ABSTRACT

EXPERIMENTAL STUDIES OF ISOBARIC QUINTETS

By

Arno George Ledebuhr

The mass excesses of the lowest T=2 states in the nuclei ^{24}Al, ^{8}Be, and ^{8}Li have been determined.

The highly proton-rich nucleus ^{24}Si has been produced via the ^{24}Mg(^{3}He,3n) reaction. A cryogenic helium jet and a recoil time-of-flight mass analyzer system were constructed for use in observing short-lived beta-delayed particle emitters. The half-life of ^{24}Si was found to be 103(42) ms, and the energy of the protons de-exciting the T=2 state in the daughter, ^{24}Al, has been measured as 3912.7(37) keV. From detailed consideration of masses in the A=24 completed isobaric quintet, it is concluded that this quintet constitutes a test of the quadratic isobaric multiplet mass equation (IMME) as precise as the mass 9 quartet and that there is, in this case, no significant departure from the equation.

Measurements of the Q values for the reactions ^{10}Be(p,t)^{8}Be(T=2) and ^{10}Be(p,^{3}He)^{8}Li(T=2) have been carried out using an Enge split-pole magnetic spectrograph. Data

were recorded on photographic plates and analyzed using the MSU plate-scanning system. The Q values determined were -27484.3(14) keV and -26821.3(57) keV for the ^{8}Be and ^{8}Li experiments respectively. These measurements have removed the deviation from the quadratic IMME that existed previous to these results.

An analysis of all A=4n isobaric quintets (five complete) for $A \leq 44$ has been carried out. Predictions for missing members have been made using the quadratic IMME. In no case has any significant deviation from the quadratic form of the isobaric multiplet mass equation been found. This leaves only the mass 9 ground state quartet where a known deviation is present and where sources of significant experimental error have probably been eliminated.

EXPERIMENTAL STUDIES OF ISOBARIC QUINTETS

By

Arno George Ledebuhr

A DISSERTATION

Submitted to
Michigan State University
in partial fulfillment of the requirements
for the degree of

DOCTOR OF PHILOSOPHY

Department of Physics

1982

To Sharon,
with all my love

ACKNOWLEDGMENTS

I would first like to thank my advisor, Dr. R.G.H. (Hamish) Robertson for suggesting this thesis project and for helping and guiding me during my graduate school career. Hamish has been a real friend and mentor.

I would also like to thank all the staff at the Cyclotron Laboratory with whom I have worked — both past and present. They have made working (and sometimes living) at the lab more enjoyable for me.

To my fellow graduate students — my nuclear beer companions — I would like to say that your support, our friendship and good times will always be remembered.

Lastly, I would like to thank my wife, Sharon, for her love and companionship, for her patience through the many lonely nights and for all her help in preparing this thesis.

TABLE OF CONTENTS

LIST OF TABLES

LIST OF FIGURES

INTRODUCTION

The isobaric multiplet mass equation (IMME) is a result of first-order perturbation theory, with the assumption that only two-body forces are responsible for charge-dependent effects in nuclei. The equation predicts that the mass excesses ΔM of analog states of an isobaric multiplet can be determined by a three-parameter quadratic equation

$$\Delta M = a + bT_z + cT_z^2.$$

Deviations from the quadratic form of the IMME could be expected if there were charge-dependent many-body nuclear forces, isospin mixing or shifts in unbound levels. These deviations are usually parametrized as cubic or quartic terms in T_z (dT_z^3,eT_z^4). If an isobaric quintet (T=2 multiplet) is used to test this equation, both additional terms can be determined, whereas only one can be determined in a quartet (T=3/2 multiplet).

In a review article by Benenson and Kashy (Be79), an analysis of 22 complete isobaric quartets found that only in one case - the ground state A=9 quartet - was there a significant deviation from the quadratic IMME (d coefficient of 5.8(16) keV). However, mass 9 is also the most accurately measured quartet and one cannot conclude that

this deviation is exceptional without obtaining results of comparable accuracy in other multiplets. Isobaric quintets offer the prospect of improved tests of the IMME.

This dissertation describes measurements which yield a test of the IMME in the A=24 quintet of the same level of precision as the mass 9 quartet. New measurements on the A=8 quintet have removed the slight deviation that existed previous to this work.

The thesis is organized as follows: Chapter One contains a discussion of the theory of the isobaric multiplet mass equation; Chapter Two describes the measurement of the ^{24}Al T=2 level and includes the details of the design of a cryogenic helium jet and recoil time-of-flight mass analyzer system constructed for this measurement; Chapter Three contains the details of the measurements of the lowest T=2 levels in ^{8}Be and ^{8}Li; Chapter Four discusses the A=24 and 8 quintets along with a summary of the remaining A=4n quintets for $A \leq 44$. There are now five completed quintets.

CHAPTER ONE

1.1 Isotopic spin and charge-independence.

Isotopic spin has its origins in the observations of low energy proton scattering which revealed that, neglecting Coulomb effects, the proton-proton (p-p) and proton-neutron (p-n) forces are very similar (Br36,Ca36). These observations led to the hypothesis of the charge-independence of the nuclear force and started the development of isospin as an important quantum number.

The hypothesis of charge-independence is that, neglecting the electromagnetic effects, the force between p-p, p-n and n-n pairs will be identical when these pairs are in the same space and spin states. Because the p-n system is not made of identical particles, there are space and spin configurations available to this system that are not allowed for the p-p and n-n system. It is only those configurations (where the identity of the nucleons does not matter) for which the forces may be compared.

Heisenberg postulated (He32) (shortly after the discovery of the neutron) that the specifically nuclear forces between a pair of protons (p-p) would be the same as that between a pair of neutrons (n-n). The hypothesis, of

the equivalence of the p-p and n-n force, is known as charge-symmetry. This is a less restrictive statement than the one of charge-independence because charge-independence implies charge-symmetry but not vice versa.

The charge-dependent nature of the nuclear force is considered to be due solely to the effects of the electromagnetic interaction. These effects are classified as direct and indirect (He69). The direct part includes the Coulomb force, vacuum polarization effects, the neutron-proton mass difference, and the magnetic forces (such as the spin-orbit force). These direct effects involve no meson exchange between the nucleons and are present even in the absence of hadronic forces.

The indirect charge-dependent effects are present only when there are nuclear forces. These effects, as described by Henley (He69,He81), include the mass difference between the neutral and charged mesons, mass differences of baryons (during two-pion exchange for example), radiative corrections to meson-nucleon coupling constants, meson mixing caused by the electromagnetic interaction, and forces that arise from meson plus photon exchanges.

In isospin formalism, the proton and neutron are opposite projections of the nucleon in isotopic spin space. This is not a projection in physical space as with normal spin but rather a fictitious space used as a convenience. Because of the two-state nature of the nucleon, the same formalism as with spin 1/2 can be applied.

The presence of the isospin quantum number allows for the generalization of the Pauli principle so that the wave function for a system of nucleons must be antisymmetric under interchange of any two nucleons.

The operator t is defined as the isospin operator for an individual nucleon with three cartesian components of t_x, t_y, and t_z. The projection of the t operator is defined as t_z. The neutron is assigned an isospin projection of $t_z=+1/2$ and the proton a projection of $t_z=-1/2$. This is the original (and still-standard) convention that is used in nuclear physics. In particle physics the opposite sign convention is used. The standard nuclear physics notation will be used here.

T is the total isospin operator for the nucleus. This is defined as

$$\vec{T} = \sum_{i=1}^{A} \vec{t}_i \qquad (1\text{-}1)$$

and has a projection given by,

$$T_z = \sum_{i=1}^{A} t_z(i) = (N-Z)/2 \qquad (1\text{-}2)$$

The charge-independent part of the nuclear Hamiltonian H_N commutes with the total isospin operator,

$$[H_N, T^2] = 0 \qquad (1\text{-}3)$$

In the isospin representation, the wave functions of the nuclear Hamiltonian are eigenstates of T and have no T_z dependence. That is

$$H_N |\alpha_0, TT_z\rangle = E^{(0)}(\alpha_0, T) |\alpha_0, TT_z\rangle \qquad (1\text{-}4)$$

where α_0 represents all the other quantum numbers (aside from T and T_z) that are necessary to specify the nuclear wave function (such as spin and parity). The energy of these states $E^{(0)}(\alpha_0, T)$ is independent of T_z so there are 2T+1 degenerate states with this energy and with quantum numbers α_0 and T.

These 2T+1 states, all having the same wave functions, will occur in 2T+1 different nuclei. They all have the same total number of nucleons and, therefore, have become known as an isobaric multiplet. The A=8 isobaric quintet (T=2) is shown in Figure 1-1.

For a nucleus with T=1/2, there are two degenerate states with T_z=+1/2 and -1/2. These are called mirror pairs. A state with a T that is larger than the T_z of the nucleus (e.g., a T=1 state in a T_z=Ø nucleus) is known as an analog state, because there exist states in neighboring nuclei that are analogous to it.

The total Hamiltonian for a system of nucleons contains change-dependent terms which do not commute with the isospin operator and, therefore, break the degeneracy of the analog states among a given isobaric multiplet. As mentioned earlier, these terms are considered to be electromagnetic in origin.

Aside from the neutron-proton mass difference, the major contributor to the breaking of the degeneracy among the analog states is the static Coulomb potential. Because the strength of the electromagnetic interaction is

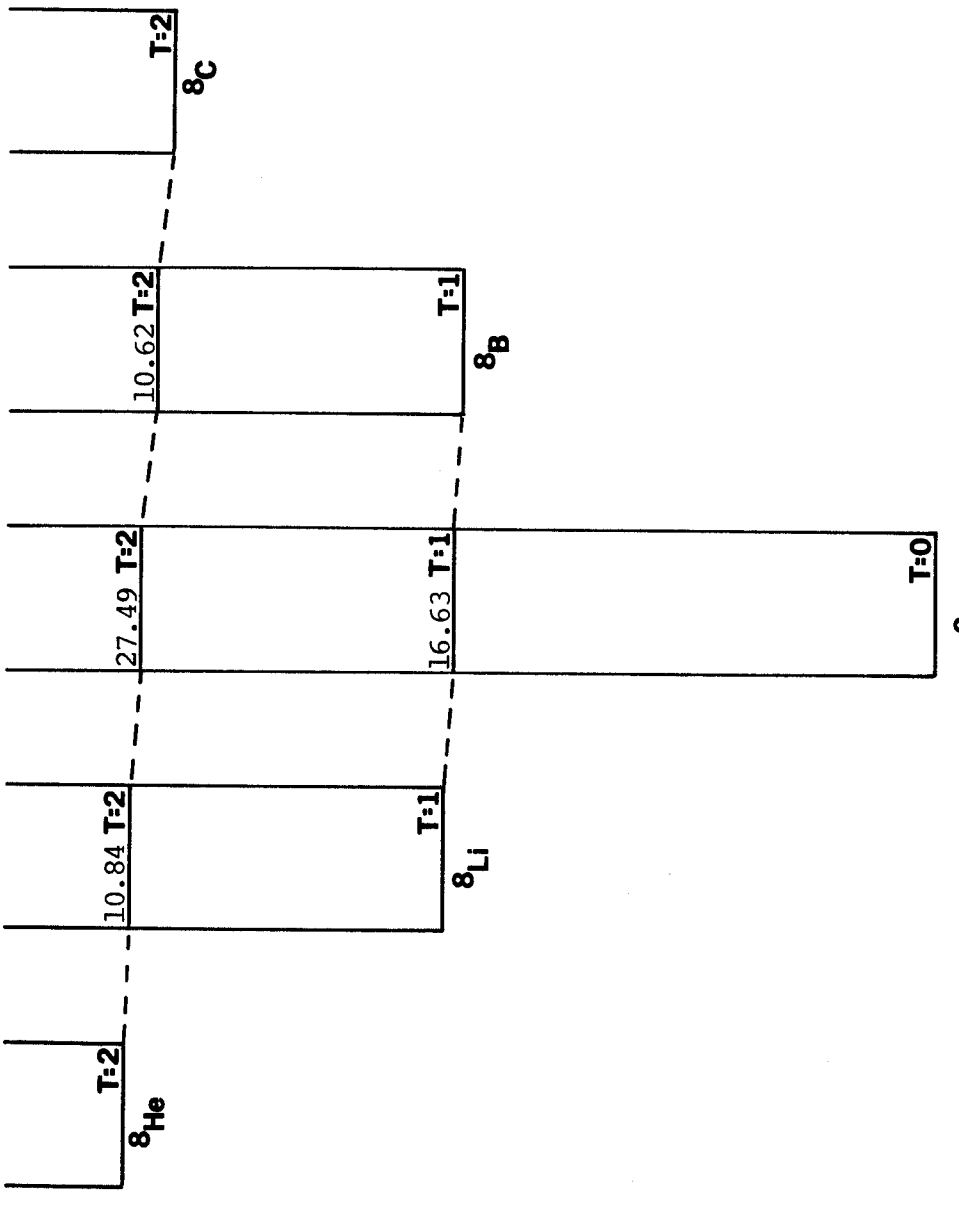

Figure 1-1. The A=8 isobaric (T=2) quintet.

only 1/137 that of the nuclear force, it can be considered as a perturbation on the nuclear force. Perturbation theory can then be used to calculate the splitting between the analog states.

Wigner (Wi57) was the first to show the effect of the Coulomb potential on the mass differences of the analog states. His derivation involved a simple application of the Wigner-Eckart theorem in first-order perturbation theory and produced the well-known isobaric multiplet mass equation (IMME):

$$\Delta M = a + bT_z + cT_z^2 \qquad (1\text{-}5)$$

The crucial decomposition of the Coulomb operator (in isospin representation) into its irreducible parts was first accomplished by MacDonald (Ma55). This explicit decomposition into an isoscalar, isovector and isotensor part allowed for the simple application of the Wigner-Eckart theorem (Wi57).

1.2 Derivation of the IMME.

The total Hamiltonian can be written as the sum of the charge-independent nuclear part H_N, and the charge-dependent electromagnetic part H_C. This latter term can be considered to be due principally to the static Coulomb interaction.

$$H = H_N + H_C \qquad (1\text{-}6)$$

In first-order perturbation theory, the correction to the unperturbed energies $E^{(0)}(\alpha_0,T)$ is

$$E^{(1)}(\alpha_0,T) = \langle \alpha_0 T T_z | H_C | \alpha_0 T T_z \rangle \qquad (1\text{-}7)$$

The Coulomb potential in isospin representation is given by

$$H_C = e^2 \sum_{i<j} \frac{\left(\frac{1}{2} - t_z(i)\right)\left(\frac{1}{2} - t_z(j)\right)}{r_{ij}} \qquad (1\text{-}8)$$

With the stated convention that $t_z=1/2$ for neutrons and $t_z=-1/2$ for protons, the $(1/2-t_z(i))(1/2-t_z(j))$ product will then be nonzero only for proton pairs. Multiplying these terms together yields

$$H_C = e^2 \sum_{i<j} \frac{1}{r_{ij}} \left[\frac{1}{4} - \frac{1}{2}\left(t_z(i)+t_z(j)\right) + t_z(i)\,t_z(j)\right] \qquad (1\text{-}9)$$

Inserting the isoscalar $\frac{\vec{t}(i)\cdot\vec{t}(j)}{3}$ into equation 1-9, (Ma55) results in

$$H_C = e^2 \sum_{i<j} \frac{1}{r_{ij}} \left\{\left[\frac{1}{4} + \frac{\vec{t}(i)\cdot\vec{t}(j)}{3}\right] - \left[\frac{t_z(i)+t_z(j)}{2}\right] + \left[t_z(i)\,t_z(j) - \frac{\vec{t}(i)\cdot\vec{t}(j)}{3}\right]\right\} \qquad (1\text{-}10)$$

The first term in brackets is the zeroth component (in cartesian form) of a zero-rank irreducible tensor operator $H_0^{(0)}$. The second and third bracketed terms are the zeroth components (in cartesian form) of rank 1 and rank 2 irreducible tensor operators $H_0^{(1)}$ and $H_0^{(2)}$ respectively. These terms are listed separately as follows,

$$H_0^{(0)} = e^2 \sum_{i<j} \frac{1}{r_{ij}} \left[\frac{1}{4} + \frac{\vec{t}(i)\cdot\vec{t}(j)}{3} \right] ; \quad \Delta T = 0$$

$$H_0^{(1)} = e^2 \sum_{i<j} \frac{1}{r_{ij}} \left[\frac{t_z(i)+t_z(j)}{2} \right] ; \quad \Delta T = 0, \pm 1 \qquad (1\text{-}11)$$

$$H_0^{(2)} = e^2 \sum_{i<j} \frac{1}{r_{ij}} \left[t_z(i)t_z(j) - \frac{\vec{t}(i)\cdot\vec{t}(j)}{3} \right] ; \quad \Delta T = 0, \pm 1, \pm 2$$

The Coulomb operator can now be expressed as

$$H_C = H_0^{(0)} + H_0^{(1)} + H_0^{(2)} \qquad (1\text{-}12)$$

The ΔT's following the explicit forms of the tensor operators, Equation 1-11, show the connections that each operator can make between states of differing isospin. These connections are not important for first-order perturbation theory where only diagonal matrix elements are considered. However, in second-order perturbation, these operators may cause additional energy shifts due to isospin mixing.

The fact that the Coulomb operator is reducible into the zeroth components of these tensors assures that only states with the same T_z values will overlap (i.e., states in the same nucleus).

Application of the Wigner-Eckart theorem yields for the first-order correction to the unperturbed energies

$$E^{(1)}(\alpha_0,T) = \left\langle \alpha_0 T T_z \left| H_c \right| \alpha_0 T T_z \right\rangle = \sum_{k=0}^{2} \left\langle \alpha_0 T T_z \left| H_0^{(k)} \right| \alpha_0 T T_z \right\rangle$$

$$= \sum_{k=0}^{2} \left\langle T k T_z 0 \left| T T_z \right\rangle \right. \left\langle \alpha_0 T \left| \left| H^{(k)} \right| \right| \alpha_0 T \right\rangle \qquad (1\text{-}13)$$

The Clebsch-Gordan coefficients are

$$\left\langle T 0 T_z 0 \left| T T_z \right\rangle \right. = 1$$

$$\left\langle T 1 T_z 0 \left| T T_z \right\rangle \right. = \frac{T_z}{\sqrt{T(T+1)}} \qquad (1\text{-}14)$$

$$\left\langle T 2 T_z 0 \left| T T_z \right\rangle \right. = \frac{3T_z^2 - T(T+1)}{\sqrt{(2T-1)T(T+1)(2T+3)}}$$

Inserting the Clebsch-Gordan coefficients into Equation 1-13 yields

$$E^{(1)}(\alpha_0,T) = \left\langle \alpha_0 T \left| \left| H^{(0)} \right| \right| \alpha_0 T \right\rangle +$$

$$+ \frac{T_z}{\sqrt{T(T+1)}} \left\langle \alpha_0 T \left| \left| H^{(1)} \right| \right| \alpha_0 T \right\rangle + \qquad (1\text{-}15)$$

$$+ \frac{3T_z - T(T+1)}{\sqrt{(2T-1)T(T+1)(2T+3)}} \left\langle \alpha_0 T \left| \left| H^{(2)} \right| \right| \alpha_0 T \right\rangle$$

Rewriting Equation 1-15 in terms of powers of T_z results in

$$E^{(1)}(\alpha_0,T) = \left[\langle\alpha_0 T||H^{(0)}||\alpha_0 T\rangle - \frac{T(T+1)\ \langle\alpha_0 T||H^{(2)}||\alpha_0 T\rangle}{\sqrt{(2T-1)T(T+1)(2T+3)}}\right] +$$

$$+ \left[\frac{\langle\alpha_0 T||H^{(1)}||\alpha_0 T\rangle}{\sqrt{T(T+1)}}\right] T_z + \qquad (1\text{-}16)$$

$$+ \left[\frac{3\ \langle\alpha_0 T||H^{(2)}||\alpha_0 T\rangle}{\sqrt{(2T-1)T(T+1)(2T+3)}}\right] T_z^2$$

The $E^{(1)}(\alpha_0,T)$ is the mass correction to the unperturbed states and is the well-known isobaric multiplet mass equation (Equation 1-5).

$$\Delta M = a + bT_z + cT_z^2 \qquad (1\text{-}17)$$

The neutron-proton mass difference may be accounted for by simply including a sum of the neutron and proton masses in the Hamiltonian.

$$H_{\Delta M} = M_n N + M_p Z \qquad (1\text{-}18)$$

where N+Z=A and M_n is the neutron mass and M_p is the proton mass. The mass difference effect is made more transparent when Equation 1-18 is written in isospin formalism

$$H_{\Delta M} = \sum_{i=1}^{A}\left[M_n\left(\frac{1}{2}+t_z(i)\right) + M_p\left(\frac{1}{2}-t_z(i)\right)\right] \qquad (1\text{-}19)$$

Upon rearrangement this becomes

$$H_{\Delta M} = \left(\frac{M_n+M_p}{2}\right)\left(\sum_{i=1}^{A}\right) + \left(M_n - M_p\right)\sum_{i=1}^{A} t_z(i) \qquad (1\text{-}2\emptyset)$$

which further reduces to

$$H_{\Delta m} = \left(\frac{M_n+M_p}{2}\right)A + \left(M_n - M_p\right)T_z \qquad (1\text{-}21)$$

These terms can then be absorbed into the a and b coefficients of the IMME.

The spin-orbit interaction has been shown by Garvey and Hecht (Ga69,He66) to also be expressible in terms of irreducible tensor operators of rank zero, one and two. So it too will preserve the form of the IMME.

In general, any two-body force will have the form (Ga69)

$$V_{ij} = V_1\left[t_z(i) + t_z(j)\right] + V_2\left[t_z(i)\,t_z(j)\right] \qquad (1\text{-}22)$$

which may be decomposed into a linear combination of irreducible scalar, vector and tensor operators. Hence, the IMME will result from the use of any two-body force in first-order perturbation theory.

1.3 Violations of the IMME.

In second-order perturbation theory, the correction to the energies for the static Coulomb potential is given as (GA69,BA73)

$$E^{(2)}(\alpha_0,T) = \sum_{T'}\sum_{i} \frac{\left|\left\langle \alpha_0 T T_z \left| H_C \right| \alpha_i T' T_z \right\rangle\right|^2}{E^{(0)}(\alpha_0,T) - E^{(0)}(\alpha_i,T')} \qquad (1\text{-}23)$$

(When $T'=T$, then $i\neq 0$.)

where $T'=T,\ T\pm1,\ T\pm2$.

With the application of the Wigner-Eckart theorem, the explicit T_z dependence of this second-order correction can be extracted. Janecke and Garvey (Ja69,Ga69) have shown that the major effect of this higher-order correction is to alter the a, b, and c coefficients. These changes can then be absorbed back into the standard form of the IMME (Equation 1-17). There are, however, terms with a T_z^3 and T_z^4 dependence generated by this expression which result in the "quartic" form of the IMME

$$\Delta M = a + bT_z + cT_z^2 + dT_z^3 + eT_z^4 \qquad (1\text{-}24)$$

These d and e terms, though small relative to a, b, and c, will have the form

$$d \cong \sum_i \frac{\langle \alpha_0 T || H^{(1)} || \alpha_i T' \rangle \langle \alpha_i T' || H^{(2)} || \alpha_0 T \rangle}{E^{(0)}(\alpha_0, T) - E^{(0)}(\alpha_i, T')} \qquad (1\text{-}25)$$

(When $T'=T$, then $i \neq 0$.)

where $T'=T, T\pm1$.

and

$$e \cong \sum_i \frac{\langle \alpha_0 T || H^{(2)} || \alpha_i T' \rangle^2}{E^{(0)}(\alpha_0, T) - E^{(0)}(\alpha_i, T')} \qquad (1\text{-}26)$$

(When $T'=T$, then $i \neq 0$.)

where $T'=T, T\pm1$ and $T\pm2$.

In order to distinguish between the effects of a charge-dependent, many-body force (which presumably would manifest itself in first-order perturbation theory) over the higher-order effects of a two-body force, detailed shell-model calculations will be required.

Isospin mixing is expected to cause deviations from the IMME. Isospin-forbidden resonance reactions have been used successfully to discover a number of higher T levels in lower T_z nuclei (T=2 states in T_z=Ø nuclei). So isospin admixtures are known to exist and could therefore be responsible for generating relative shifts between multiplet members. Figure 1-2 illustrates the effect of isospin-mixing in both quartets and quintets. For quartets, it is apparent that mixing with lower T levels would primarily produce only changes in the c coefficient. In quintets, however, mixing between T=Ø and T=2 levels in the T_z=Ø nucleus (Ro76) would, by symmetry, produce an even-order eT_z^4.

In the case of the A=8 multiplet, it is known that this state is admixed with a T=Ø state (from the observation of the T=2 state in the T_z=Ø nucleus ^{8}Be, as an isospin forbidden resonance in the ^{6}Li + d reaction). A generation of an e coefficient is seen to occur, both from the qualitative argument shown in Figure 1-2 and from the results of second-order perturbation theory Equation 1-26. Assuming only one T=Ø perturbing state with the same spin and parity as the T=2 state, the e coefficient has the form

EFFECTS OF ISOSPIN MIXING

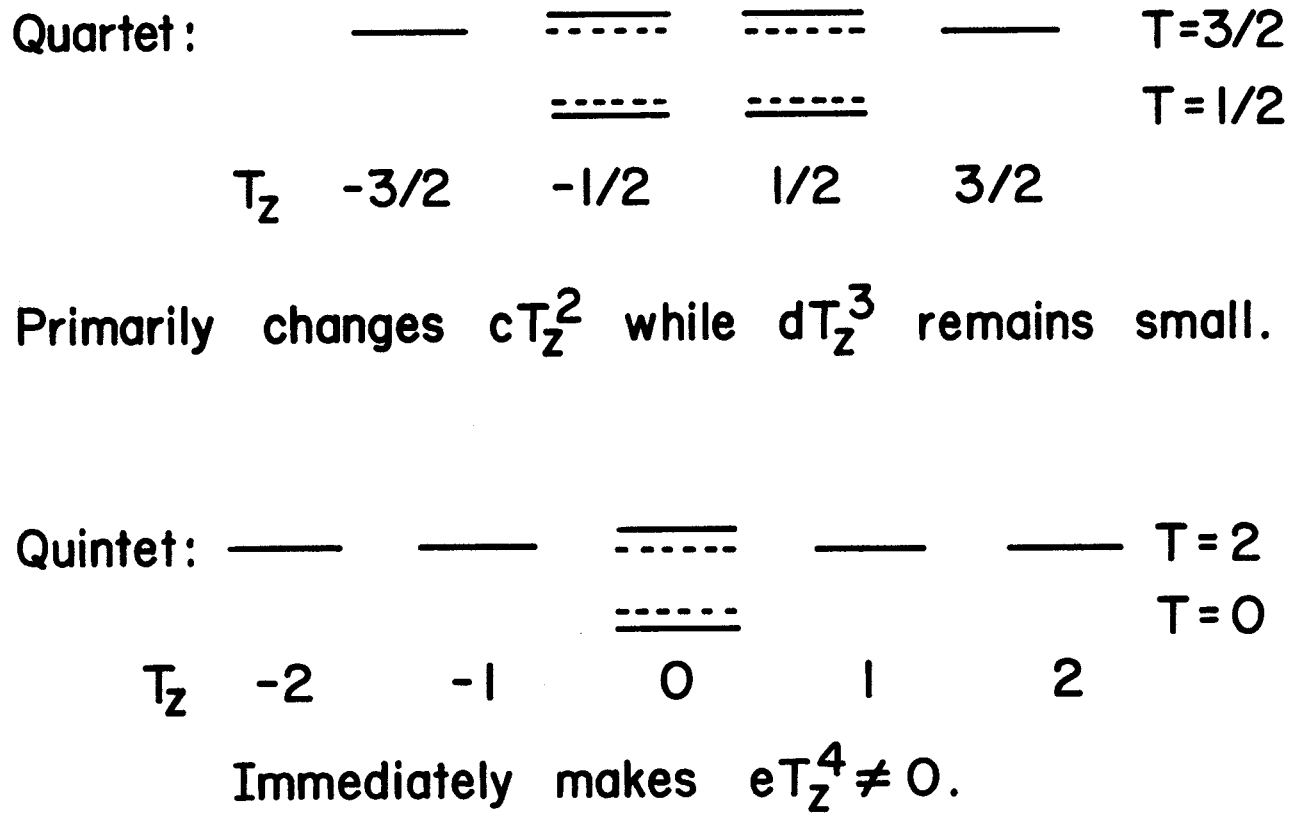

Figure 1-2. Isospin-mixing in quartets and quintets.

$$e = \frac{1}{20} \frac{\langle 2||H^{(2)}||0\rangle^2}{E^{(0)}(2) - E^{(0)}(0)} \qquad (1\text{-}27)$$

where the $\frac{1}{20}$ comes from evaluation of the Clebsch-Gordan coefficients.

For an e coefficient of 1 keV and an off-diagonal matrix element of order 100 keV, the perturbing state must lie within 500 keV of the T=2 state. As of yet this state has not been observed but evaluation of the sign of the e coefficient will determine its position with respect to the T=2 state. Actual observation of this T=0 state would then allow a determination of the size of the off-diagonal Coulomb matrix element.

It has also been suggested that changes in the wave functions between members of a multiplet could cause a deviation from the quadratic IMME. For example, the expansion of the radial wave function due to the effects of the Coulomb repulsion in the proton-rich member of a multiplet could cause a change in the calculated expection value, and hence a change in the relative separation of the levels. However, calculations have shown (Be70,Be77) that the major change occurs in the b and c coefficients and only small d and/or e coefficients are generated. The change to the b and c coefficients is absorbed back into the IMME without causing a significant deviation.

For a complete quintet the five coefficients of the quartic IMME are completely specified:

$$
\begin{aligned}
a &= M_0 \\
b &= \tfrac{1}{12}[8(M_1-M_{-1})-(M_2-M_{-2})] \\
c &= \tfrac{1}{8}[16(M_1+M_{-1})-(M_2+M_{-2})-30M_0] \qquad (1\text{-}28) \\
d &= \tfrac{1}{12}[(M_2-M_{-2})-2(M_1-M_{-1})] \\
e &= \tfrac{1}{24}[(M_2+M_{-2})-4(M_1+M_{-1})+6M_0].
\end{aligned}
$$

From these expressions it is apparent that the coefficients are more sensitive to the inner members of the multiplet and therefore accurate determination of these are necessary for a precise test of the IMME.

CHAPTER TWO

2.1 Introduction

The use of the helium jet technique for the rapid transport of activities from a region of high background radioactivity to a much lower one has been quite successful. In most applications, room temperature helium gas has been used. This necessitates the use of some sort of macroscopic impurity or cluster in the gas to obtain useful transport efficiencies and in fact, quite impressive and even reproducible results (50% over ten meters) have been obtained with some impurities (Ma76).

The high transport efficiencies are understandable in terms of Bernouilli's equation for laminar flow. A radial pressure gradient exists that forces the clusters which carry the activity to remain in the center of the capillary over long distances.

Though the impurity-laden helium jet has shown its ability to transport activity over long distances and with high efficiency, these impurities may limit or even eliminate its use in certain applications. These include interfacing the helium jet to certain types of ion sources for mass spectroscopy, precise studies of β-spectra, high-resolution studies of heavy particle emission and

fundamental weak interaction studies which rely on the line shapes of β-delayed heavy particle lines.

It was found in 1974 by Äystö et al. (Ay74) that for "pure" helium cooled to liquid nitrogen temperatures (77°K) that a significant improvement in transport efficiency was possible relative to room temperature impurity-free helium jets (Ay73).

A model presented by Robertson et al. (Ro77) explains this behavior in terms of the thermal diffusion of active atoms through the carrier gas. This model assumes the loss of active atoms is due to collisions with the capillary wall which occur during their transport through the capillary. The increased efficiency is shown to be due in equal measure to the decrease in temperature (which decreases the rate of thermal diffision to the capillary wall) and to the increased molecular flow rate (which shortens the time the active atoms remain in the capillary).

In a paper by Robertson et al. (Ro77), the description of a cryogenic (liquid-nitrogen cooled) helium jet coupled to a recoil time-of-flight mass analyzer for use in observing short-lived β-delayed particle emitters was presented. This apparatus was used at Princeton University in an attempt to observe ^{24}Si. Results tentatively suggested that protons from the decay of this nucleus had been observed and that the mass of the T=2 state in the daughter nucleus ^{24}Al was consistent with the prediction from the quadratic form of the isobaric multiplet mass

equation. With these promising results, an improved apparatus was contructed here at Michigan State University with the intent of observing ^{24}Si and other T_z=-2 nuclei.

It is a feature of this apparatus that mass identification and background reduction can be obtained with only a single surface barrier Si detector (rather than a counter telescope) to detect the protons. The improved resolution and linearity, as well as the simultaneous recording of strong calibration groups, make possible a very precise measurement of the mass of the T=2 state in ^{24}Al. In addition, the first direct measurement of the half-life of ^{24}Si has been made. Figure 2-1 illustrates the β^+-delayed proton decay of ^{24}Si.

2.2 Beamline and beam transport

For these experiments a beam of 7Ø Mev ^{3}He ions from the Michigan State University Cyclotron produced ^{24}Si via the ^{24}Mg(^{3}He,3n) reaction. Figure 2-2 shows the beamline layout to the cryogenic helium-jet target chamber (located in vault 1). Also shown is the capillary feedthrough to the recoil time-of-flight apparatus (located in vault 5).

Beam position and focus were verified with a scintillator placed Ø.3 m in front of the target chamber. The beam passed through a 1.3 cm diameter aperture in each side of the target chamber and stopped in a water Faraday cup placed Ø.4 m past the target chamber. This Faraday cup was electrically isolated from the target chamber and the

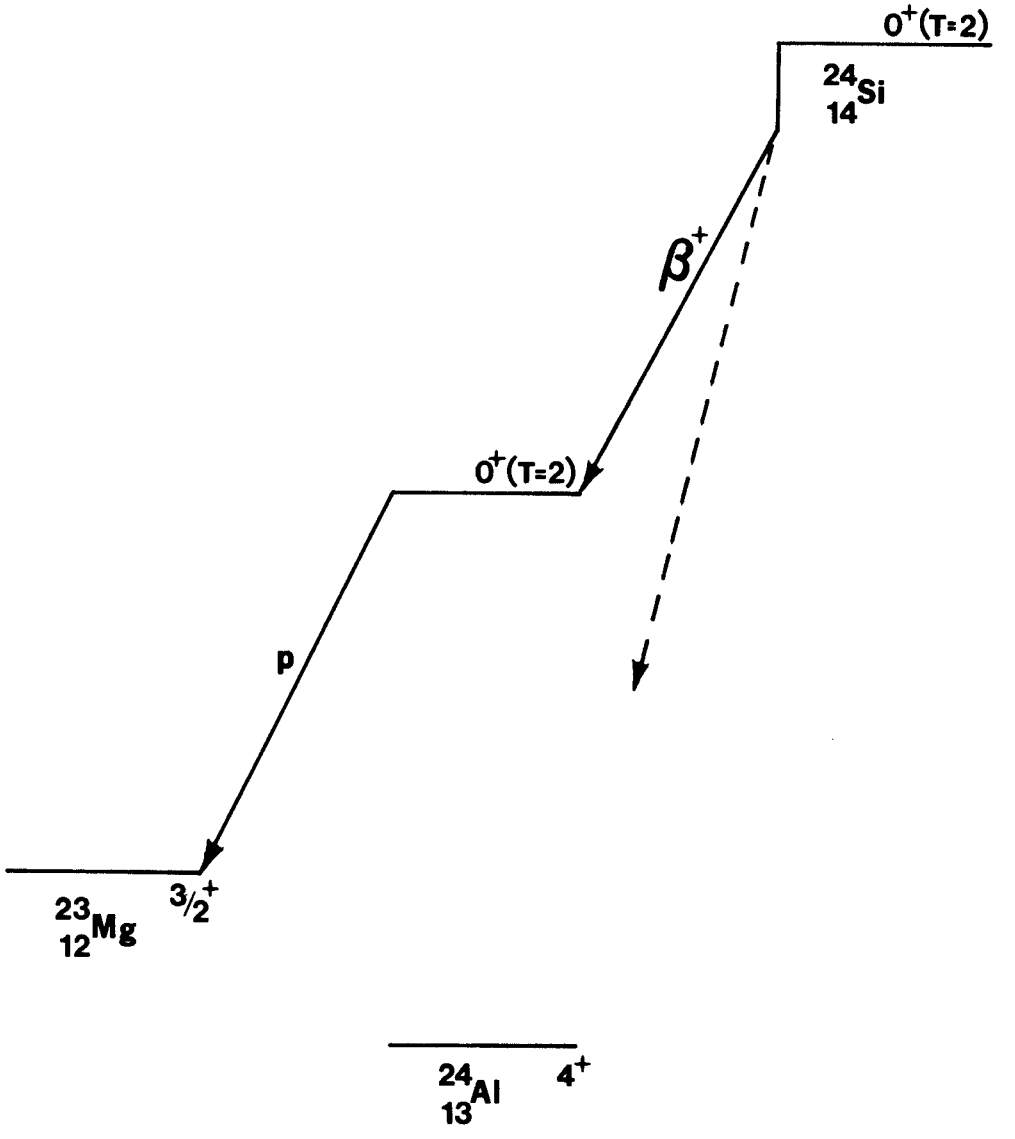

Figure 2-1. Illustration of the β^+-delayed proton decay of ^{24}Si.

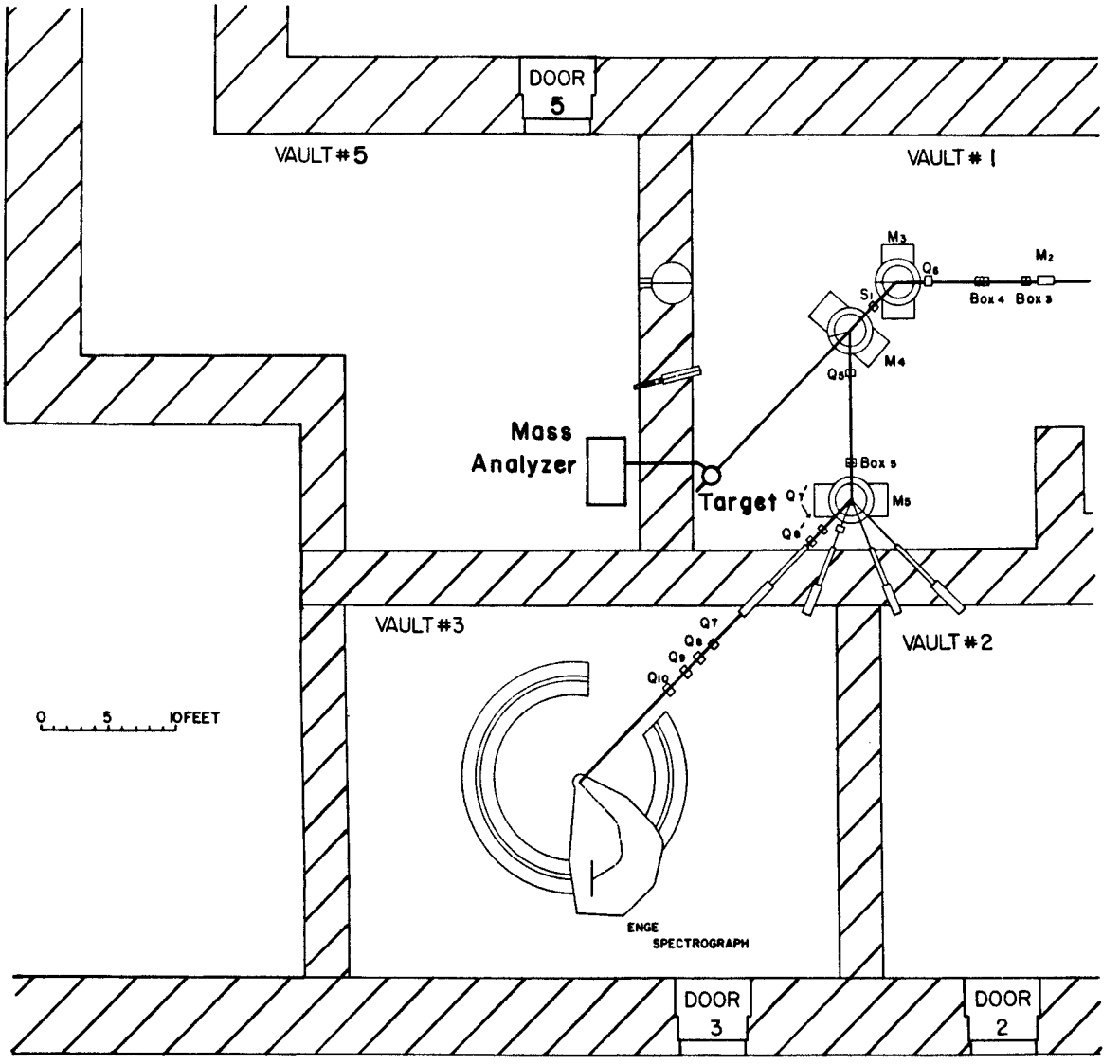

Figure 2-2. Beamline layout to target chamber.

rest of the beamline with an 8 cm section of insulating beam pipe. A current integrator gave both the total charge and the beam current. The beamline elements were adjusted to yield the maximum current from the Faraday cup. Depending on the tuning of the cyclotron, this current usually lay between 1 and 3 μA of ^{3}He++. Such currents did not lead to failures of the 5.25 mg/cm^2 Havar windows of the target chamber (Hi75). However, on one occasion, the windows ruptured after just three hours of 4-6 μA of beam current.

2.3 Helium jet target chamber

The helium jet target chamber consisted of a large (18 cm outer diameter x 35.5 cm long and 2.54 cm thick) aluminum tube, sealed at both ends with 1.3 cm thick aluminum cover plates. All flanges were sealed with indium wire.

The chamber was connected to the beamline by two stainless steel (5 cm outer diameter x 23 cm long and 1.7 mm thick) tubes, a 7.6 cm long section of which was turned down to a thickness of only ≅1 mm. This was done to minimize the heat loss through these tubes. The chamber was placed in a large (24 cm inner diameter x 46 cm inside depth) stainless steel dewar (Mv76) which was filled periodically with liquid nitrogen (LN_2). A LN_2 level controller (Nv76a) was used to keep the dewar full. A sensor placed ≅2Ø cm from the top of the dewar detected when the level of LN_2 went below this sensor. A solenoid valve then pressurized a feed dewar

which delivered LN_2 to the target chamber dewar for approximately three minutes. An insulating styrofoam cover was fit over the top of the dewar and target chamber and the stainless steel beamline connecting tubes were wrapped with a flexible styrofoam insulation. Figure 2-3 shows a cross-section of the target chamber.

Commercially "pure" He (99.995%) was sent at room temperature via 1/4 inch "poly flo" tubing to the vicinity of the target chamber where it connects to a 1.3 cm diameter copper tube of 2.5 m in length. As Figure 2-3 shows, this tubing was coiled about the target chamber and also placed in the LN_2 dewar. Thus, the He gas was cooled to $\cong 77°K$ before entering the target chamber. The gas entered through a porous stainless steel diffuser with 2 μm openings (Nu77). This prevented turbulence created by incoming gas which could significantly reduce the transport of activities (Ro77).

The target was mounted on a target holder which projected into the chamber as shown in Figure 2-4. The recoiling activities from the reaction of the beam in the target were thermalized (slowed down) in the cold He gas. In order to prevent the range of the recoils in the gas from exceeding the width of the target holder, the gas pressure was kept at approximately .7 atmospheres. Because of the increased gas density at 77°K, this pressure was sufficient to limit the range of the recoils to under 1 cm. The activities were then swept out of the chamber along with the

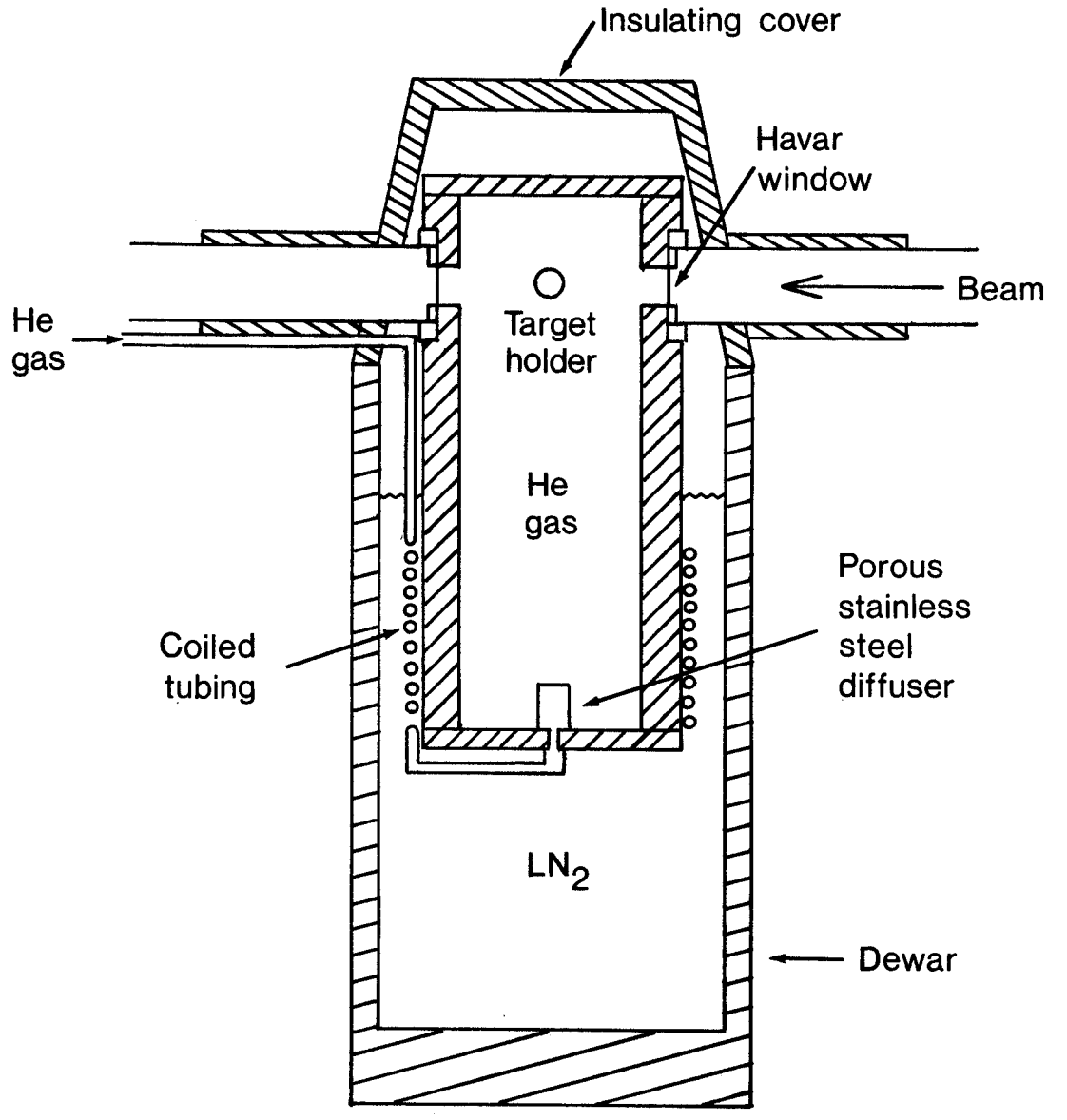

Figure 2-3. Cross-section of the target chamber.

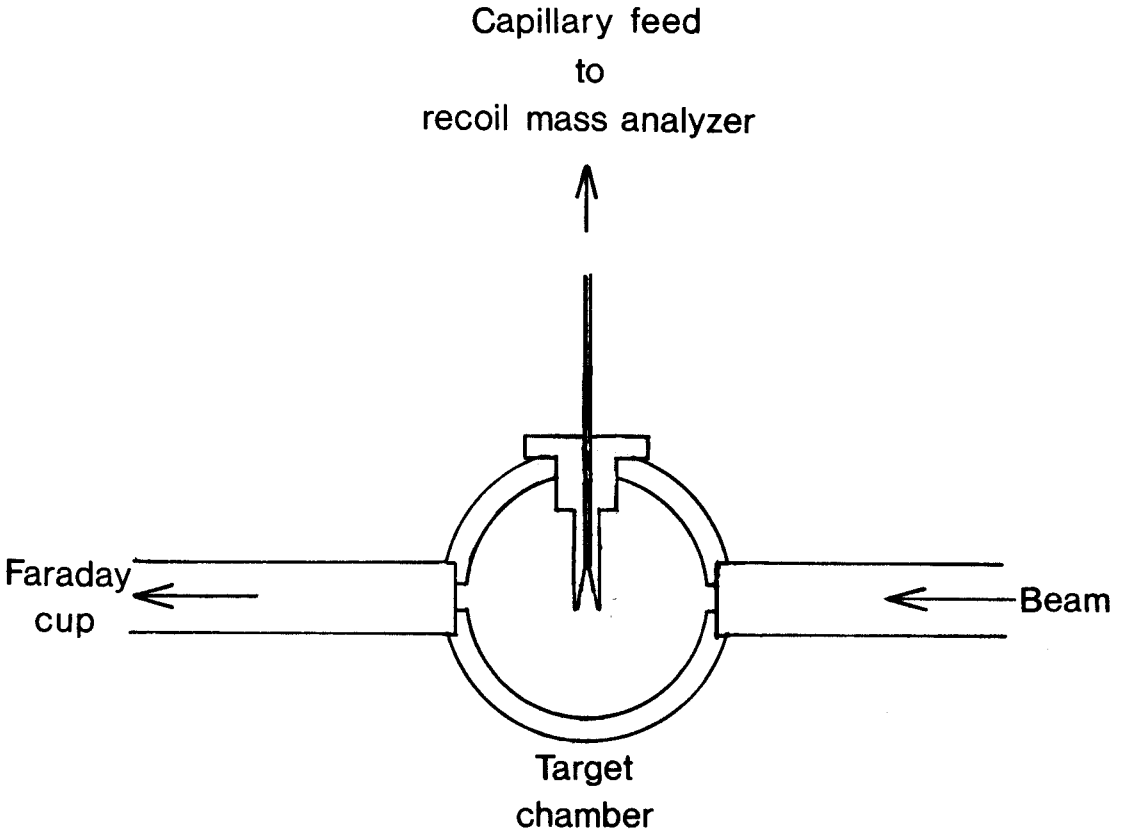

Figure 2-4. Top view of the target chamber.

He gas via a flared polyethylene capillary tube (1.8 mm inner diameter) and transported 2.4 m to the recoil time-of-flight mass analyzer.

2.4 Target holder and target

It was found by Robertson et al. (Ro77) that the target holder design was critical to the transport efficiency. Any turbulent flow behind the target reduced the transport of activities dramatically. Three target holder geometries were tested in this apparatus. Figure 2-5 shows views of the three configurations. Configurations A and C gave relatively similar results, but configuration B, which was a hoped-for improvement to configuration A, gave poor results. Configuration C was a later design which was used for the majority of the data collected. Transport efficiencies were on the order of a few percent.

The target used for these experiments was 5 mg/cm^2 of ^{24}Mg (99%) enriched that had been evaporated on a 2.3 mg/cm^2 copper backing.

2.5 Capillary-skimmer cone interface

The activity exited the capillary two to three millimeters from a skimmer cone. A 140 l/s Roots blower (Ro38) backed by an 80 l/s mechanical pump (Ki65) removed a large fraction of the He gas. Figure 2-6 shows this arrangement, along with a layout of the recoil time-of-flight mass analyzer system. The skimmer is a 90°

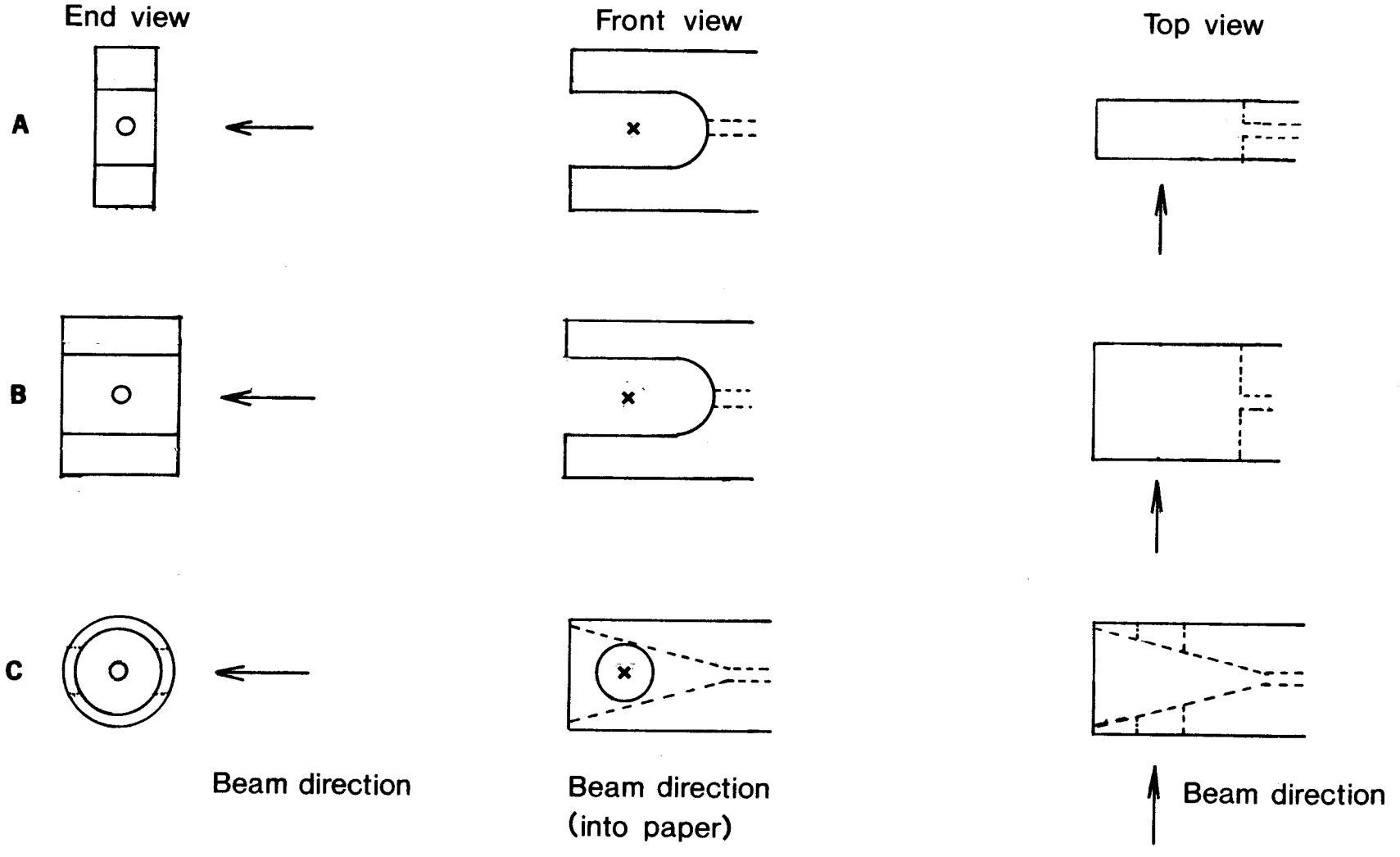

Figure 2-5. Three target holder configurations.

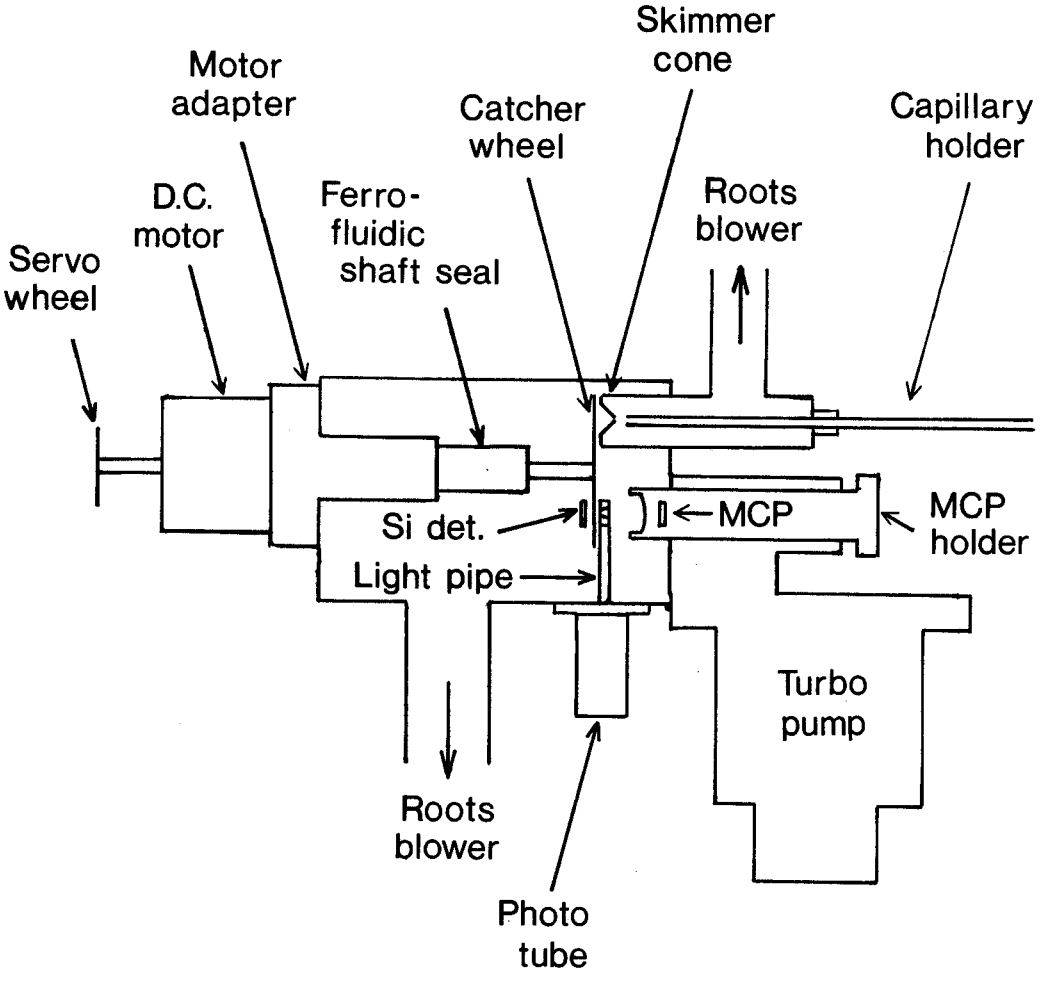

Figure 2-6. Layout of the recoil time-of-flight mass analyzer system.

cone with a 1.6 mm opening. The capillary is flared and seals against the o-ring on the end of a glass guide tube. This tube supports and also aligns the capillary with the skimmer opening.

During assembly the capillary is first flared on only one end (by holding vertically downward over a flame) and then fed through both the target holder and the shielding wall. After it is all the way past the end of the glass guide tube's seal, it is cut to length and flared. It is possible to move the recoil apparatus toward or away from the shielding wall where the capillary exits, allowing any slack to be taken up and the capillary put under tension.

2.6 Foil wheel and particle detection system.

The main chamber was pumped by a 150 l/s Roots blower (He61) backed by a 16.5 l/s mechanical pump (Va78) and a 25 l/s mechanical pump (We77) connected in parallel.

The transported atoms passed through the skimmer and into the main chamber, where they were deposited on a 10-12 $\mu g/cm^2$ thick, (6.4 mm diameter) Formvar catcher foil.

A vertically aligned foil wheel held six catcher foils. The foil wheel was stepped at a rate of 5 Hz with a high-torque hollow-rotor D.C. motor (Mi77). The wheel was connected to the motor by a Ferrofluidic shaft seal (Fe77). This seal allows for high shaft accelerations while maintaining vacuum integrity. Mounted on the opposite end

of the motor shaft, were a potentiometer (De78) and a small six-blade wheel. The potentiometer was used for recording the wheel position. The six-blade wheel (half the diameter of the catcher wheel) was part of the servo system for controlling the motor's motion. A linear filament light and a photodiode were mounted of opposite sides of the small blade wheel. The photodiode was part of a servo circuit which responded when the leading edge of the blade interrupted the light coming to the diode. This servo circuit controlled the motor which could keep the catcher foils locked into place between steps. The stepping rate was controlled external to the motor circuitry through a square wave generator.

The activity was allowed to collect for 200 ms, minus the approximate 20 ms stepping time. The wheel was then moved to its next position, where the newly-deposited activity was placed between the particle detectors (see Figure 2-7). After β-decay to particle-unstable states, both the particle emitted (proton or alpha) and the recoiling ion were observed in coincidence. Protons (or alphas) passed through the thin catcher foil and were detected using a single 150 mm^2, 300 μm deep Si detector (Or78). The residual nucleus is ejected from the surface of the foil. Figure 2-8 illustrates this arrangement.

The recoil ions have enough energy (160 keV for ^{23}Mg) to pass through a thin converter foil, placed opposite the Si detector. Secondary electrons from the converter were

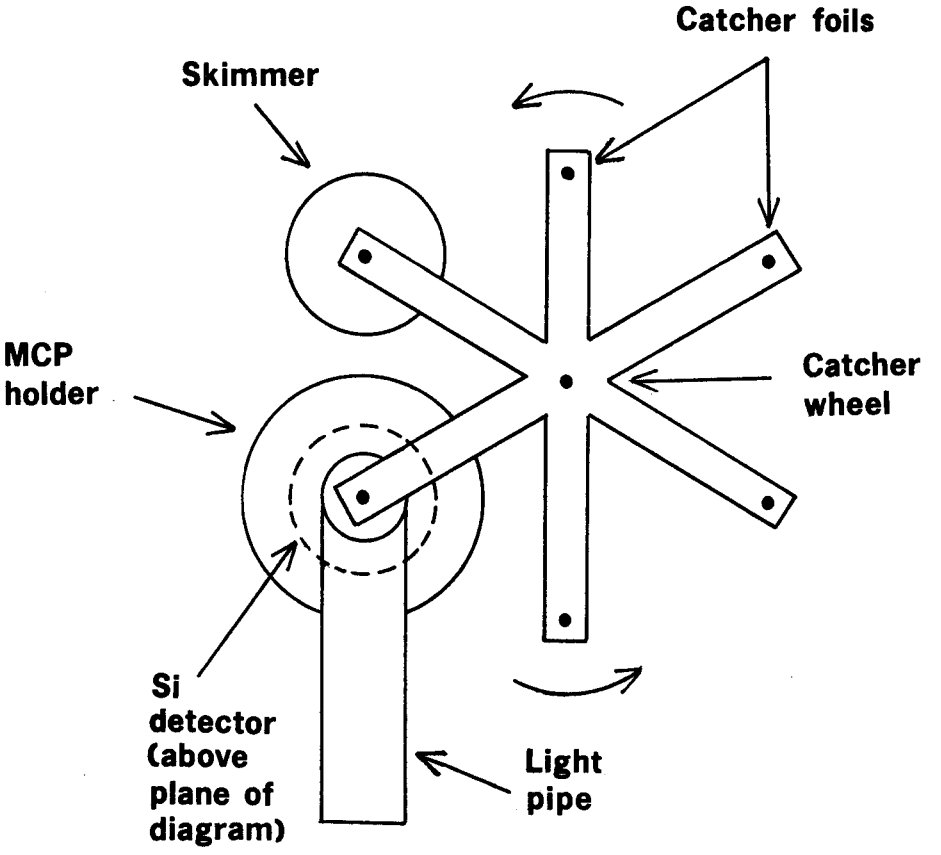

Figure 2-7. Front view of skimmer, catcher wheel and the detector system layout.

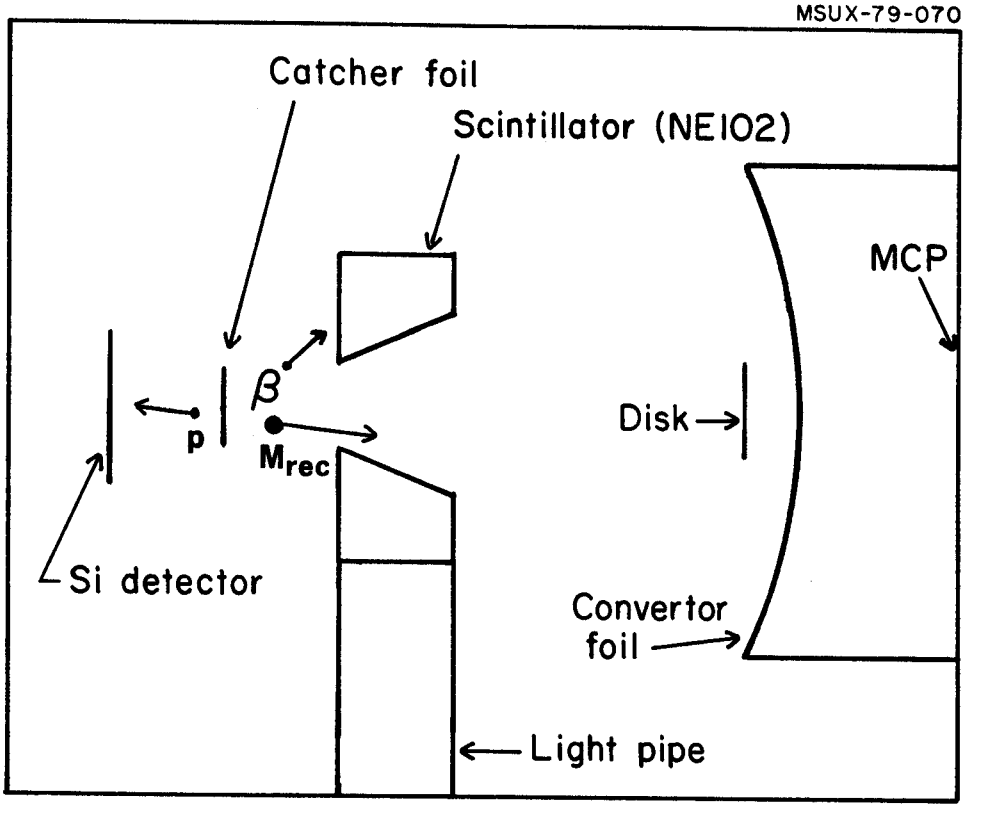

Figure 2-8. Cross section of detector region (not to scale). Activity was deposited on the right side of the catcher foil.

observed by a pair of Microchannel Plates (MCP) (Ga76). The 50.8 mm-diameter converter foil served also to isolate the MCP from the .14 torr pressure in the main detector chamber. This allowed the operation of the channel plates in a clean, high vacuum of 10^{-6} - 10^{-7} torr provided by a 1,500 l/s turbomolecular pump (Sa77).

The converter foil was shaped as a section of a sphere with an 80 mm radius of curvature. When placed 80 mm from the catcher foil, this curvature reduced the time spread of the recoil ions. Both the Si detector and converter foil subtended a solid angle of 2.6% of 4π. The converter foil consisted of a $\cong$30 $\mu g/cm^2$ layer of Formvar on a $\cong$95% transmission curved wire screen. The screen was made with 0.005 inch diameter copper wire layed onto a 80 mm radius convex wooden form. Onto the Formvar surface a $\cong$10 $\mu g/cm^2$ layer of gold and a $\cong$10 $\mu g/cm^2$ layer of CsI were evaporated. The layer of gold was used to prevent the converter foil from charging up. The CsI, with its higher secondary emission coeficient (Fa77,Bu77), was used to improve the detection efficiency of the recoils.

It may easily be shown (see Appendix A for a derivation of this result) that the mass of the recoil (daughter) nucleus M_{rec} is given by:

$$M_{rec} = \frac{\sqrt{2E_p m_p}\, t}{d} \qquad (2\text{-}1)$$

where t is the time of flight of the recoil mass, E_p the laboratory energy of the proton (or α), m_p the mass of the proton (or α) and d is the flight path (distance traveled by

M_{rec} during the time t). The recoil mass is proportional to t, not t^2 as in the usual time-of-flight system.

A start signal from the proton or alpha in the Si detector and a stop signal from the MCP gave a value for the time-of-flight of the recoil ion. This time, combined with the particle energy in the Si detector, was used in the above formula to derive the recoil mass.

The β-decay recoil determines the mass resolution in these measurements. For example, for ^{25}Si, which was produced in a competing reaction, this β-recoil limited the mass resolution to 7%, a value nevertheless adequate for mass identification. Appendix A also contains a discussion of this effect.

In initial experiments, it was found that the double coincidence data (between Si detector and MCP) showed two different recoil mass groups for the same particle energy. The second (slower) group was delayed by ≅9 ns and was attributed to recoil ions directly striking the MCP but failing to produce secondary electrons in the converter foil. In order to remove these ghost groups, which were producing a background in the region of interest, the design of an electrostatic lens was undertaken. It was hoped that a design could be found which would stop the recoils from striking the channel plates while still allowing the electrons to do so.

Lens designs were first modeled using the method of successive over-relaxation to solve Laplace's equation. See

Appendix B for a discussion of this method. A program was developed which allowed the testing of many different geometric configurations. This program also calculated particle trajectories through the lens.

A gridded lens design, illustrated in Figure 2-9, that focused the electrons to the central region of the channel plates was chosen. This design required only the central portion of the MCP to be used. The outer regions were masked off, and a small disk placed in front of the converter foil prevented the recoil ions from hitting the channel plates. A loss of only 7% in solid angle resulted from this arrangement, and a significant reduction in the background was achieved.

As in the previous apparatus (Ro77), an annular plastic scintillator was used to observe the initial β-decay of the parent nuclei. This scintillator was placed opposite the Si detector and subtended a solid angle of ≅37% of 4π. A plastic light pipe connected the scintillator to a photo-tube (Am77). Recoil ions traveled through a conical hole (20° half angle) in the scintillator to the converter foil. A cross-section of this scintillator is visible in Figure 2-8.

Many different activities are produced by the beam in the target and several delayed particle emitters were observed in our experiments. To make use of the mass identification capability, data was recorded in the event mode and, upon subsequent playback, proton and alpha energy

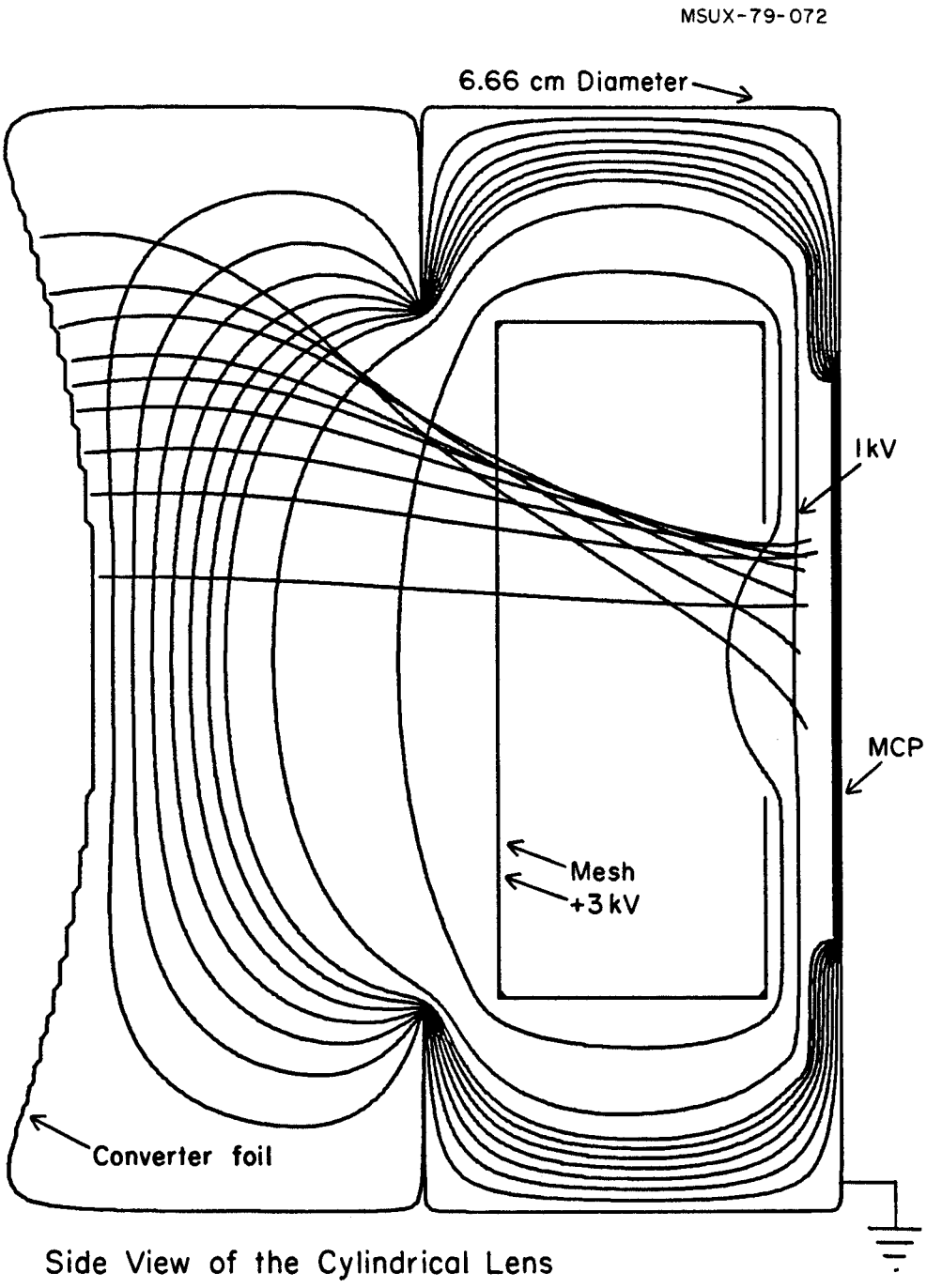

Figure 2-9. The model of the electrostatic lens, showing equipotentials and electron trajectories.

spectra for different recoil mass bands were extracted.

Eight parameters for each event were written on magnetic tape, proton energy, recoil time of flight, energy and time information from the plastic scintillator, MCP pulse height, leading-edge to crossover time for pulses from the silicon detector (used in discriminating against pileup), position of the foil wheel and, lastly, a ramp initiated by the end of a foil wheel step and strobed by pulses from the silicon detector (used in the measurement of half-lives).

Figure 2-1Ø shows a block diagram of a typical electronics set-up for these experiments.

2.7 Experimental results and analysis.

The principal delayed-particle activities observed in this experiment are ^{20}Na ($T_{1/2}$=445 ms), ^{21}Mg ($T_{1/2}$=22Ø ms), ^{25}Si ($T_{1/2}$=125 ms) and ^{24}Si ($T_{1/2}$=1Ø3 ms, this work). Figure 2-11 shows the results of a calculation using the compound nuclear evaporation code ALICE (B176). The cross sectionss for the production of each activity are plotted versus beam energy. After losing energy in the target chamber windows and gas, the beam energy was on the maximum of the production cross section. The β-delayed activity ^{20}Mg was not observed in these experiments.

Figure 2-12 shows a section of triple coincidence data (in which coincidences between the Si detector, MCP and scintillator are required), with proton energy on one axis

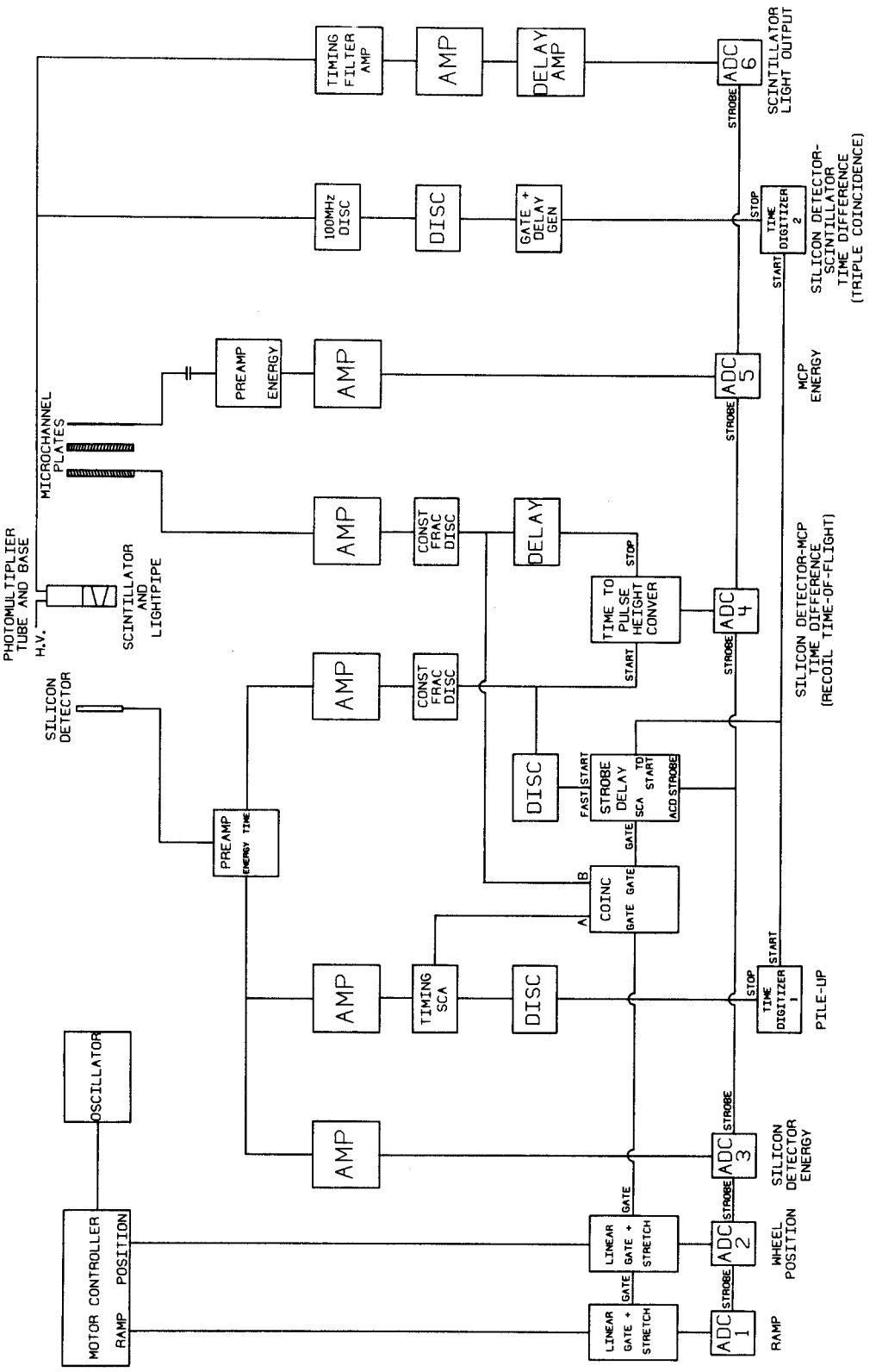

Figure 2-10. Block diagram of typical electronics set-up.

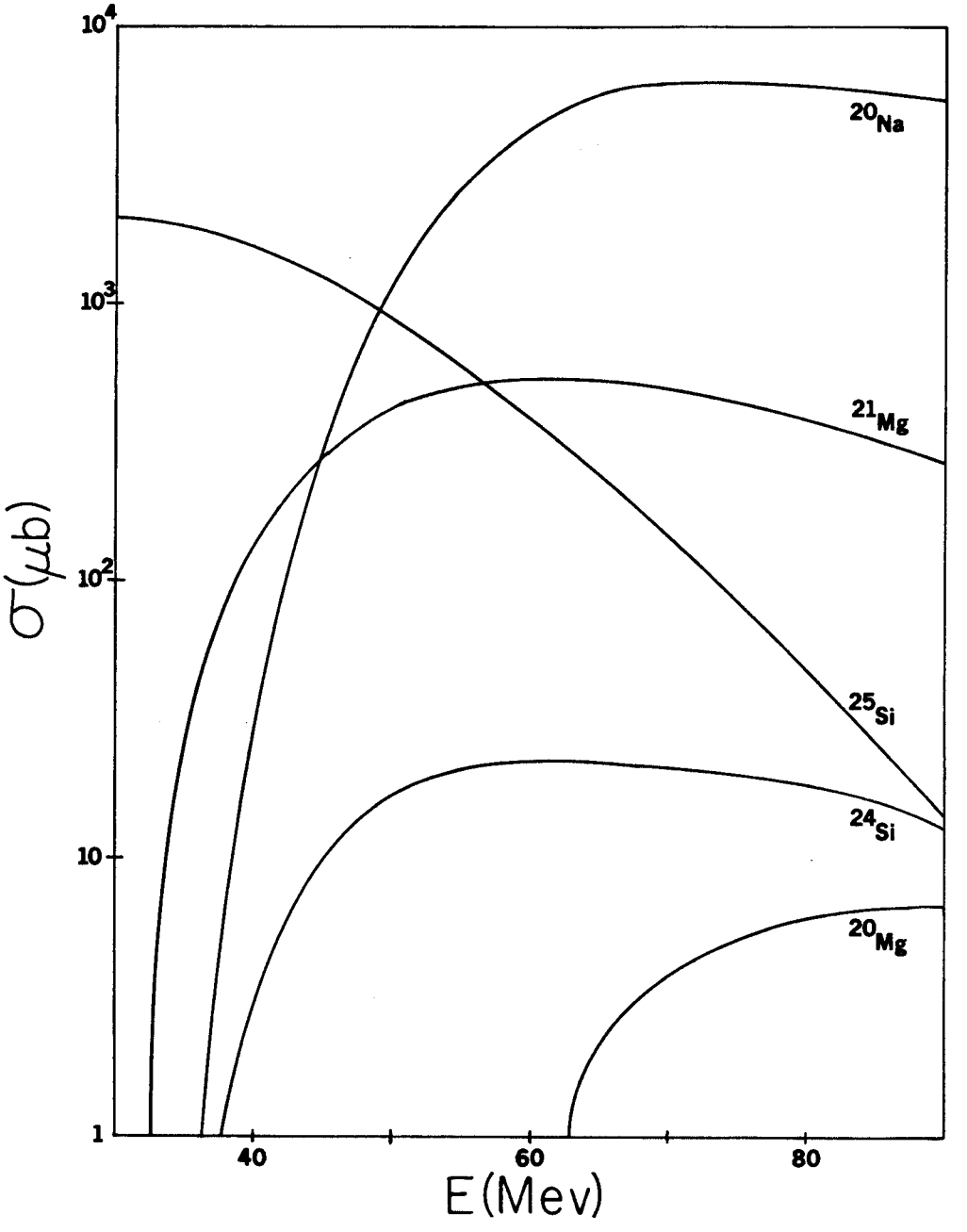

Figure 2-11. ALICE calculation of production cross sections versus beam energy for reactions of ^{3}He on ^{24}Mg.

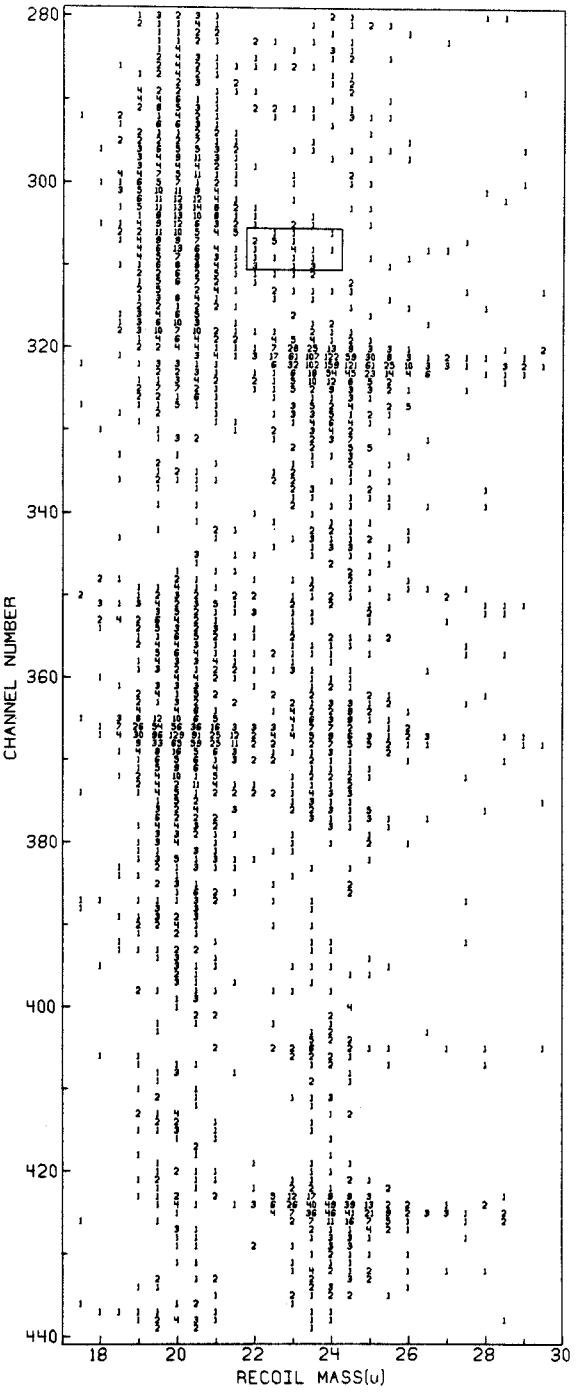

Figure 2-12. A section of triple coincidence data with proton energy (vertical axis) versus recoil mass (horizontal axis).

and recoil mass (i.e., the atomic mass of the nuclide formed following proton emission) on the other. The groups centered on 24 u at channel numbers 322 and 424 are the 4089 and 5402.2 keV protons lines from ^{25}Si decay. The groups centered on mass 20 u at channel numbers 304 and 367 are the 3900 and 4669 keV protons lines from the decay of ^{21}Mg. The box centered on 23 u at channel number 308 shows the position of the 3912.7 keV protons from the decay of ^{24}Si. The low statistics of the ^{24}Si group results from the triple coincidence requirement.

Triple coincidence data (between the Si detector, MCP and scintillator), though useful in reducing the background and improving the mass resolution for the verification of weak groups, were not directly used in obtaining the proton energy because the beta-induced recoil of the daughter has a component of its velocity toward the Si detector. Thus the particles detected in the Si detector would be on the average shifted up in energy. Therefore, only double coincidence data (between Si detector and MCP) were used to obtain the proton energy. Even for the double coincidence data there are in principle small energy shifts, which will be discussed later.

In order to convert the energy and time-of-flight data to these two-dimensional energy versus recoil mass spectra the expression,

$$M_{rec} = G\sqrt{E_p - E_o}\ (t - t_o) \qquad (2\text{-}2)$$

was used. Where E_o and t_o are energy and time offsets

respectively and G is a scaling parameter. An analysis of the energy and time-of-flight one-dimensional spectra provided initial values for these offset parameters. However, to remove skewing of the 2-D spectra it was necessary to optimize these offsets. The strong groups in ^{25}Si and ^{21}Mg (made in competing reactions) defined the mass scale. An assignment of a recoil mass of 24u to the 4Ø89 KeV and 54Ø2.2 keV groups from ^{25}Si and 2Øu to the 4669 keV and 6225 keV lines from ^{21}Mg was made. The 6225 keV peak was just at the edge of the silicon detector's range for these particles. Both with and without this group the needed parameters could be found.

A program was written that used a portion of the energy vs. recoil mass data around each peak. For a given E_o and t_o a point-by-point construction of a recoil spectrum, i.e., projection along recoil axis) and a calculation of the centroid, via a simple average, was done for each peak. By using the known recoil mass, a scale factor G was calculated. This procedure was repeated for different E_o and t_o values until the closest agreement between the scale factors for each group was obtained. The average of these four quantities was used in equation 2-2. This procedure successfully provided undistorted two-dimensional energy versus recoil mass spectra as shown in Figure 2-12.

Spectra from β-delayed protons from ^{25}Si and ^{21}Mg, and β-delayed alphas from ^{20}Na, are shown in Figure 2-13. These were obtained with the Princeton apparatus (Ro77) by setting

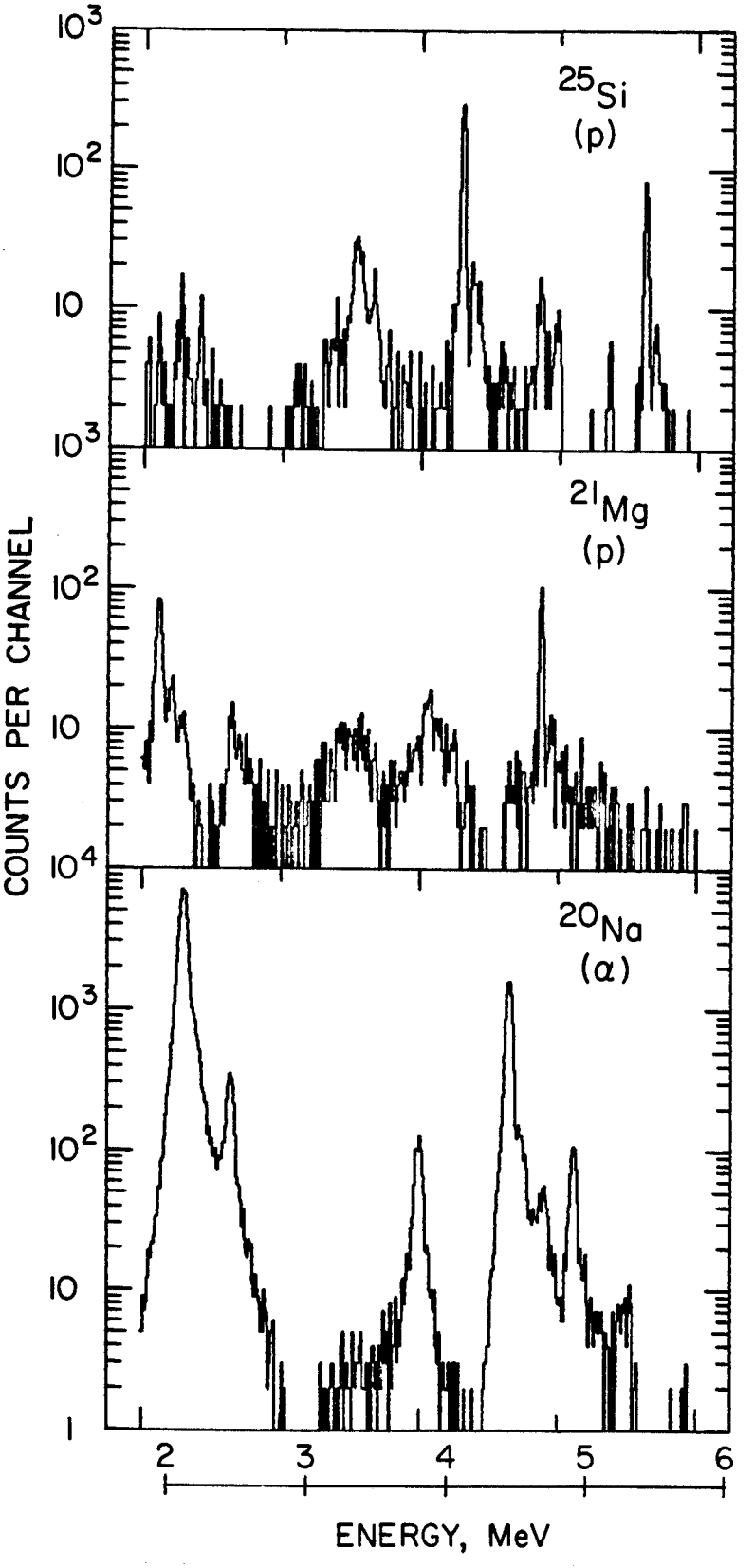

Figure 2-13. Spectra of β^+-delayed proton decays of ^{25}Si and ^{21}Mg (top and middle, respectively) and the α-decay of ^{20}Na (bottom) from (Ro77).

2 u wide windows centered on the appropriate mass regions (24 u, 20 u and 8 u) in double-coincidence (particle-recoil) data.

A projection of two-dimensional double-coincidence data along the recoil axis (as seen with the Princeton apparatus) forms the integral mass spectrum seen in Figure 2-14. Recoils (^{16}O) from the β-delayed alpha decay of ^{20}Na will appear at only half of their actual mass (8 u). Appendix A also contains a discussion of this effect.

Figure 2-15 shows a proton energy spectrum gated on a recoil mass of 23 u with a window width of 2 u. The energy resolution in this spectrum is approximately 25 keV full width at half maximum (FWHM). In addition to prominent peaks from ^{25}Si which extend partially into this band, a new peak, not seen in lower-energy bombardments (Se73), is present at an energy of 3912.7 keV. Mass spectra gated on the new peak, the 4669-keV line from ^{21}Mg and the 4089-keV line from ^{25}Si are shown in Figure 2-16. The peak at recoil mass 23 u (to the right of the peak from broad lines in the ^{21}Mg spectrum) identified it as originating from ^{24}Si β-decay. This transition has been observed by Äystö et al. (Ay79) at high mass resolution, with a proton energy of 3914(9) keV, in good agreement with the present value. The energy is in the vicinity of the IMME prediction for the ground-state proton decay of the T=2 state in ^{24}Al.

The proton energy was obtained from the double-coincidence (Si detector and MCP) spectra using the strong

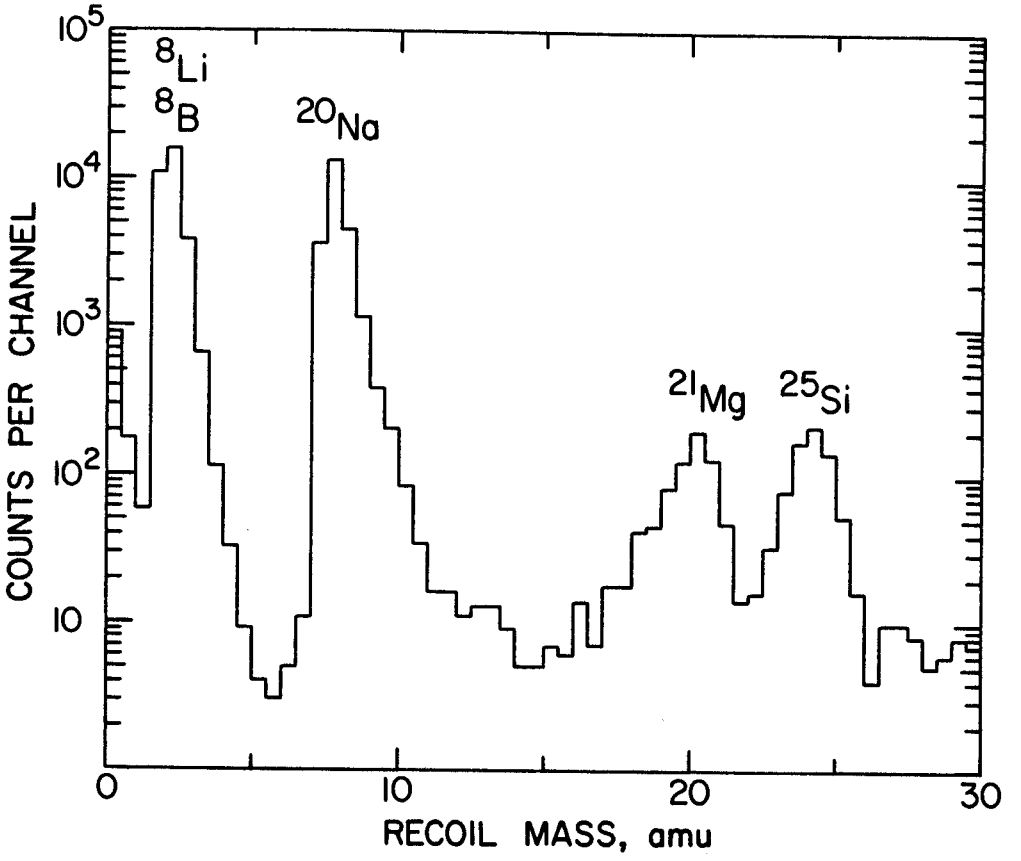

Figure 2-14. Integral mass spectrum computed from particle energies and time of flight from (Ro77).

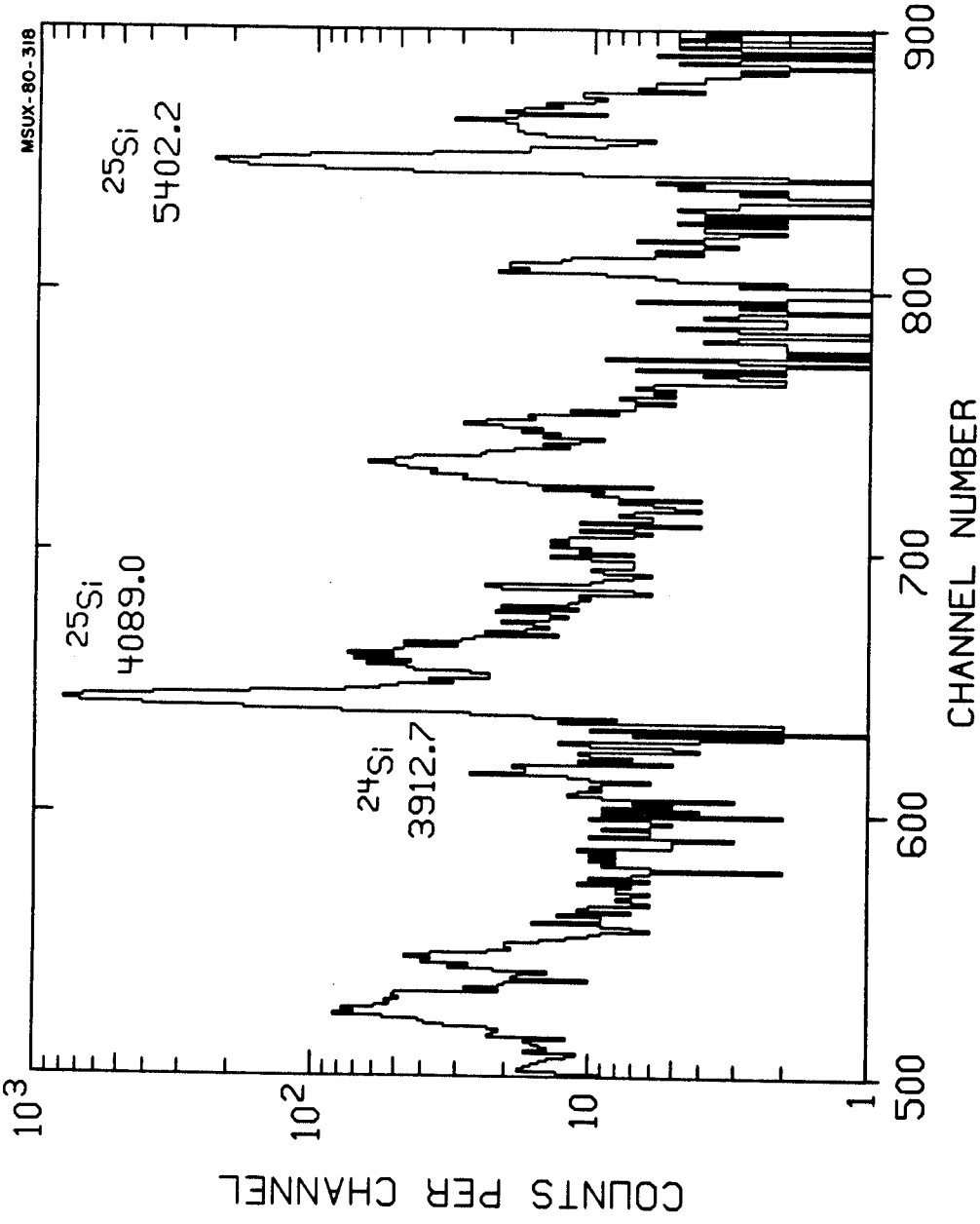

Figure 2-15. Proton energy spectrum obtained in coincidence with the MCP for recoil masses from approximately 22 to 24 u. These data represent a 650 mC bombardment.

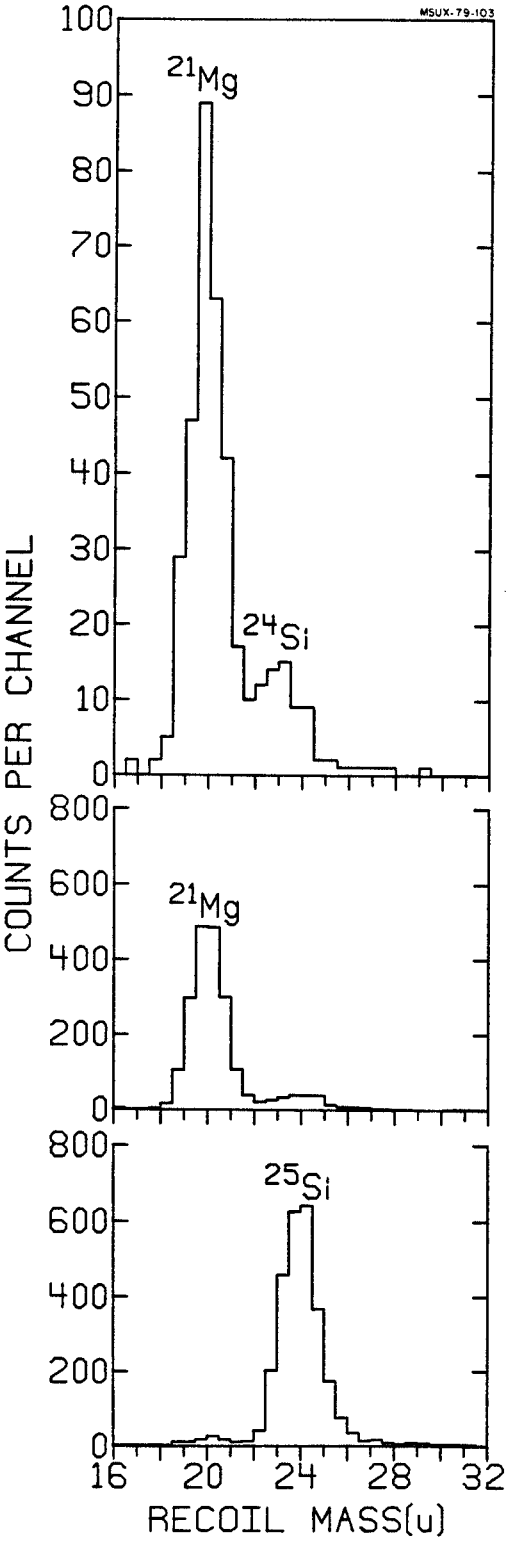

Figure 2-16. Recoil mass spectra for proton energies within ±20 keV of 3911 keV (top), 4669 keV (middle), and 4089 keV (bottom). These energies correspond to proton groups from ^{24}Si, ^{21}Mg, and ^{25}Si decay, respectively.

lines from ^{25}Si decay as calibrants. The energies of these lines are determined mainly by the measurement of the excitation energy of the lowest T=3/2 state in ^{25}Al carried out by Rogers et al. (Ro77a). This result, 7901(2) kev, coupled with the ^{24}Mg(p,γ)^{25}Al Q-value (Wa77), 2271.3(8) keV, and the excitation energy (En78) of the first excited state in ^{24}Mg, 1368.59(4) keV, leads to lab proton energies of 4089.0(22) and 5402.2(22) keV. Peak positions were obtained by fitting bivariate Gaussian distributions to the two-dimensional (recoil mass vs. proton energy) spectra, using the method of Maximum Likelihood (Me75). Figure 2-17 shows an example of a bivariate Gaussian distribution. The use of such distributions with non-zero correlation coefficients gives much improved results over simple projection of recoil bands onto the energy axis because much of the proton line broadening caused by β-recoil can be removed, since it appears as a correlation between proton energy and recoil time of flight. In this way the proton energy resolution was improved from 25 keV to 15 keV.

An illustration of two extreme cases of the correlation between proton energy and recoil time of flight is given in Figure 2-18. This shows the momentum vectors when the β-decay and subsequent proton decay are (a) parallel and (b) anti-parallel. For case (a) the excited ^{24}Al (following β-decay of ^{24}Si) is left recoiling toward the MCP detector. After proton emission the measured proton energy will be lower and the ^{23}Mg will take less time to reach the MCP.

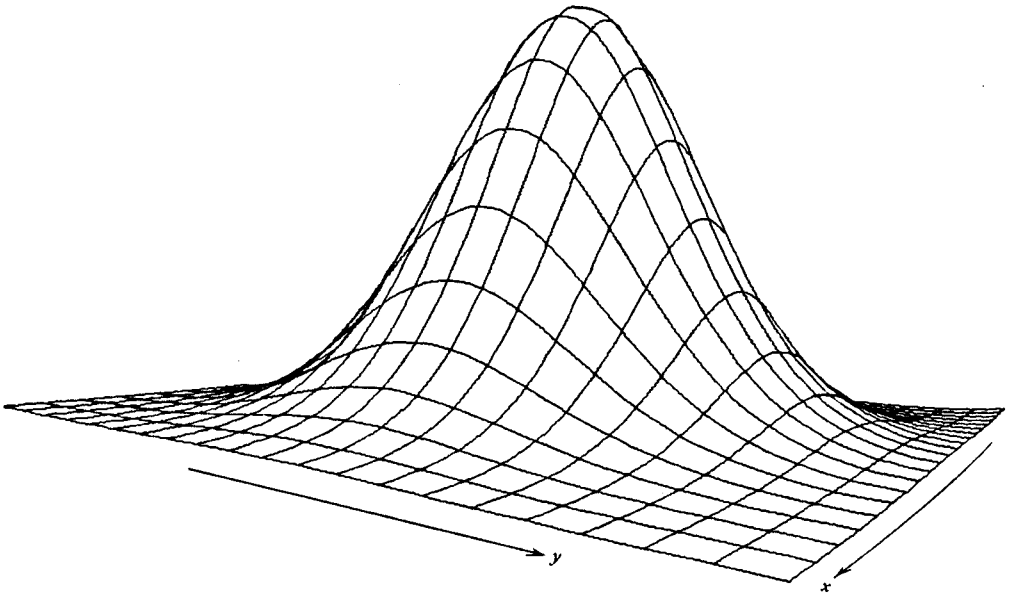

Figure 2-17. Three-dimensional plot of a bivariate Gaussian distribution.

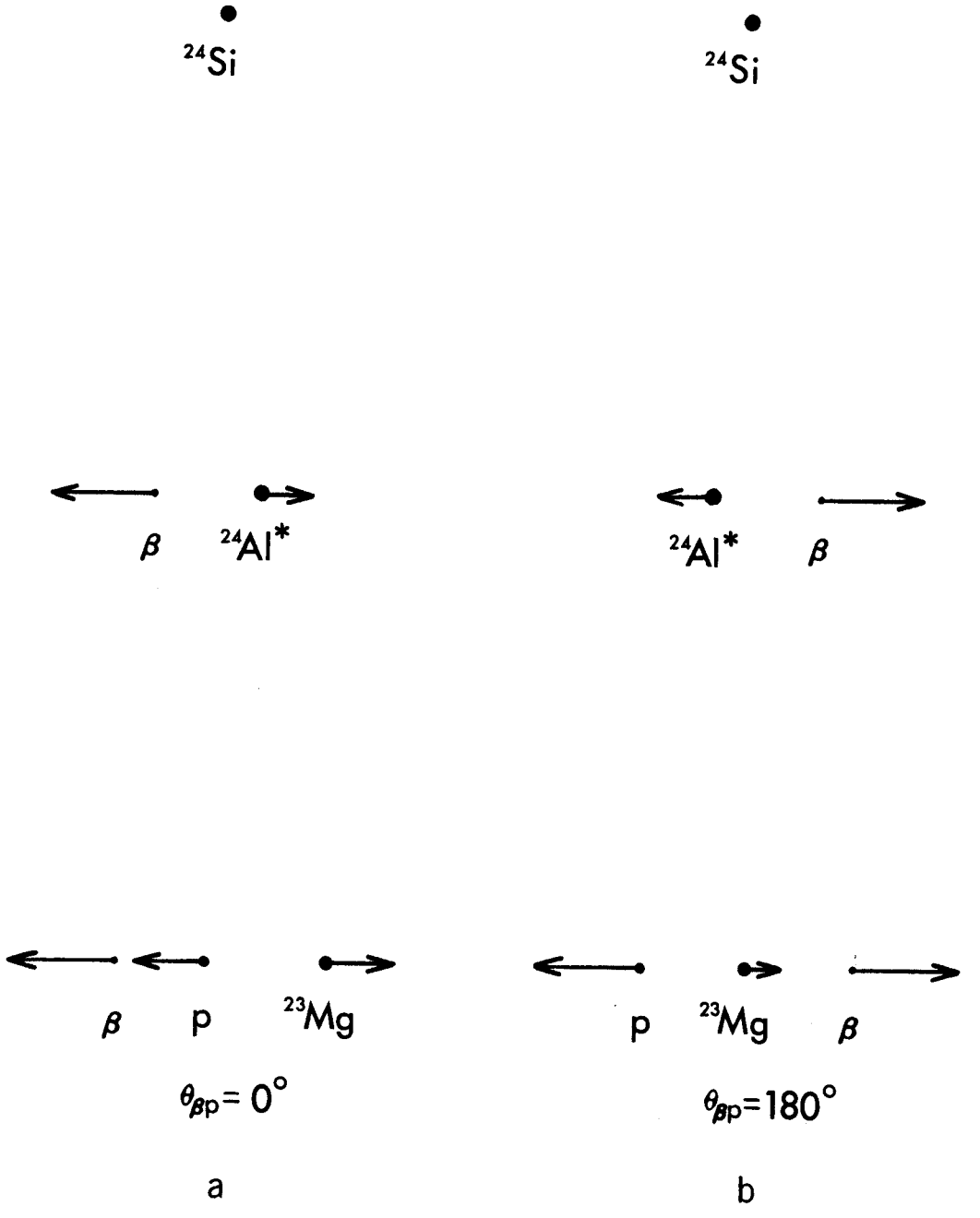

Figure 2-18. Correlation between proton energy and recoil time of flight. Momentum vectors when the beta and proton are: a) parallel, b) anti-parallel.

For case (b) the excited ^{24}Al is left recoiling toward the Si detector, so the measured proton energy is shifted up and the ^{23}Mg will take longer to reach the MCP. According to equation 2-1 the calculated recoil mass for case (a) will be smaller than that calculated for case (b). This correlation is observed as a tilting of the mass groups shown in Figure 2-12.

The shapes of the bivariate Gaussian distributions were fixed using the strong ^{25}Si lines as standards. In general, the recoil distributions are a function of β^+ end point energy, but the end points for ^{24}Si and ^{25}Si are so similar (within 200 keV) that the same recoil distribution parameters were used for the two isotopes. There is a background underlying the ^{24}Si peak which was fitted making various assumptions about its dependence on recoil mass and proton energy. The result for the centroid of the ^{24}Si peak was insensitive to these assumptions, and the final form of the background chosen was linearly varying in the recoil dimension and constant in the energy dimension. Integration of the maximum likelihood function provided an estimate for the uncertainty in the centroid position. Appendix C contains a discussion of the method of Maximum Likelihood and its application in this analysis.

A possible systematic effect arises from the β^+-proton angular distribution. Even though neither the positron (in double-coincidence data) nor the neutrino are detected, there are still two effects which can lead to centroid

shifts of the proton lines:

1) Kinematic terms in the β^+-p correlation function with a dependence on the cosine of the angle between the positron momentum and the proton momentum ($\cos\theta_{\beta p}$);
2) Rejection (loss) of proton events for which the associated positron passed through the Si detector (i.e., events with $\theta_{\beta p} \cong \emptyset$).

Both of these effects were analyzed approximately using the formalism of Holstein (Ho74) and were found to cause a centroid shift of the order of +Ø.4 keV in the ^{24}Si peak. The second effect was found to be the dominating cause of the centroid shift. This small shift is, furthermore, almost exactly cancelled by a commensurate shift in the ^{25}Si calibration lines which arise from a quite pure Fermi transition of similar energy (Se73). Thus, no correction is needed. Appendix A contains a description of this calculation.

A linear energy calibration was used to extract the energy of the ^{24}Si proton group. The latter group lies sufficiently close to the 4Ø89 keV line that only small effects would be expected from neglecting higher-order terms; however, this assumption was tested by extracting the energy of the 4669(4)-keV group (Se73) from ^{21}Mg decay for several different experimental arrangements, involving different analog-to-digital converter gains, amplifier gains and amplifier manufacturers.

The ^{21}Mg group lies almost midway between the two ^{25}Si calibration lines, so it was a more severe test of the linearity assumption (see Figure 2-13). Centroids were extracted from a projection along the energy axis as in Figure 2-15 using the peak-fitting routine SAMPO (Ro69). The standard deviation of the data indicated that the actual uncertainties were slightly larger than the statistical ones (which were determined from the fits). An average linearity error was thus added in quadrature with the statistical error. It is assumed that departures from linearity will be in random directions from run to run. The size of this error was chosen to bring the reduced chi-squared for a set of four ^{21}Mg energy measurements to approximately unity. The value obtained was 1.5 keV.

The uncertainties present in the measurement of the laboratory proton energy from decays of the T=2 level in ^{24}Al are the aforementioned linearity error (1.5 keV), the statistical error in fitting the proton peak (2.5 keV), and the uncertainty in the calibration lines (2.2 keV). A sum of these in quadrature (i.e., $\sum_i \sigma_i^2$) yields an uncertainty of 3.7 keV. The value for the proton energy from the decay of the T=2 level in ^{24}Al is:

3912.7(37) keV.

A weighted average of this value with the result of Äystö et al. (3914(9) keV), is

3912.8(36) keV

where the common 2.2 keV calibration error is removed before

calculating this weighted average. It is then added back (in quadrature) to obtain the above value.

Chapter Four contains a discussion of the effect of these results on the IMME fit to the A=24 quintet.

2.8 ^{24}Si Half-life Measurement

The half-life of ^{24}Si was extracted from the data using the well-known half-lives of ^{20}Na ($T_{1/2}$=446(3) ms), ^{21}Mg ($T_{1/2}$ =220(3) ms) and ^{25}Si ($T_{1/2}$=125(3) ms) as calibrations. Figure 2-19 shows a portion of the ramp data for the 4089 keV peak. The width of the ramp spectrum determined the total interval for detecting activity. This interval was divided into four equal sections, corresponding to equal counting times. The end points of each of these sections served as gates for the energy and recoil data. Four two-dimensional spectra of particle energy vs. recoil mass were generated for each activity. These data were again fit with the bivariate Gaussian distribution, but now the only free parameter was the peak height. These heights would of course be proportional to peak area and, therefore, the decay rate in the given interval.

In order to calculate the half-life it was necessary to determine the actual time that the four intervals corresponded to. The foil wheel was stepped at a rate of 5 Hz, so the total interval was about 200 ms. However, because the stepping time was only approximately measured ($\cong$20 ms), the exact length of time that the catcher foils

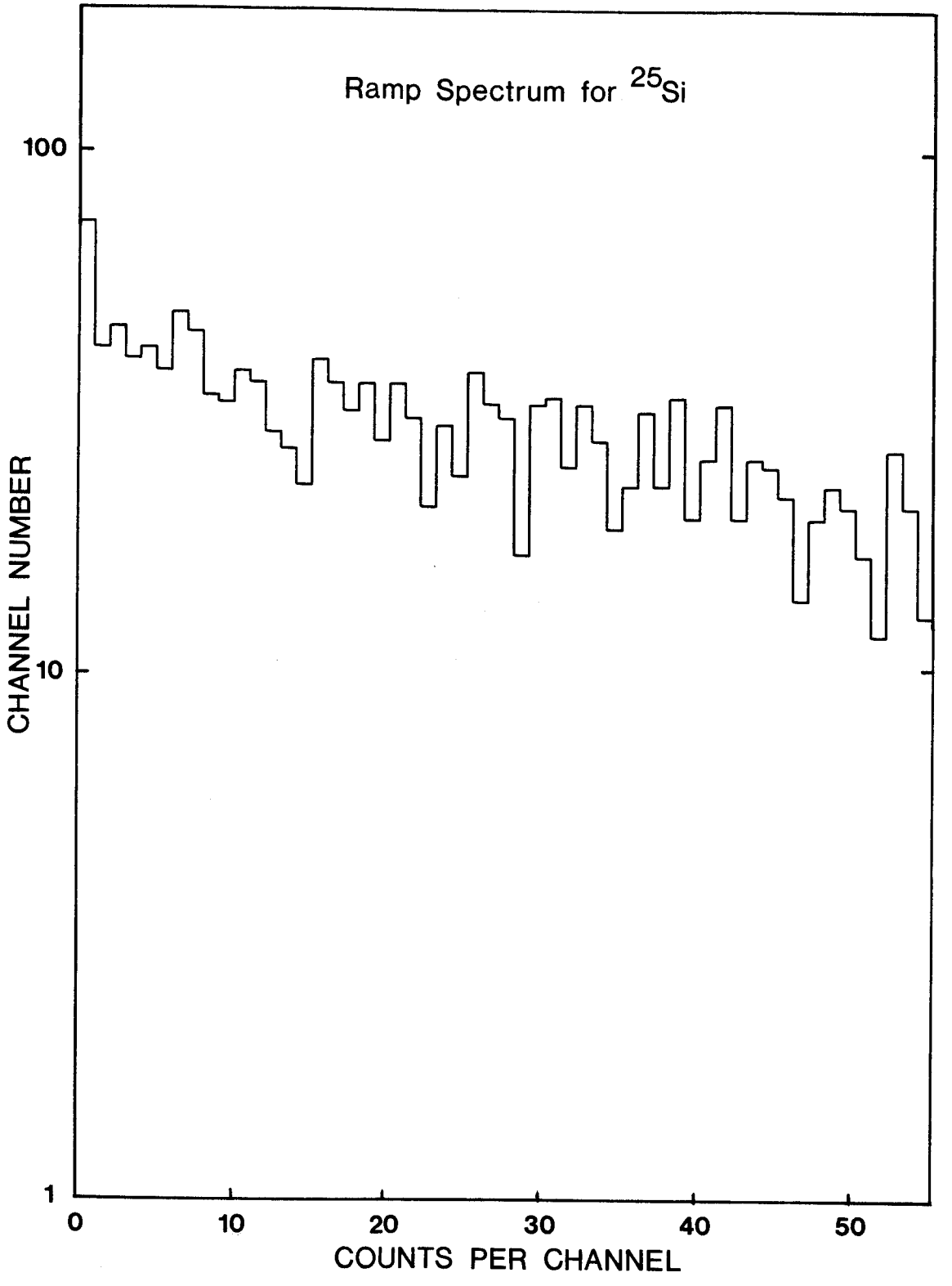

Figure 2-19. Portion of the ramp spectrum from the ^{25}Si 4089 keV peak.

were between the detectors was unknown. This difficulty was resolved by using the known activities to define a time scale.

The half-lives were first calculated for the calibration activities assuming a known total time interval. These values were compared to known half-lives using the expression 2-3.

$$\chi^2 = \sum_{i=1}^{3} \left(\frac{T_i^{theo} - T_i^{exp}}{\sigma_i^{theo}} \right)^2 \qquad (2\text{-}3)$$

Where T^{theo} is the calculated value, T^{exp} is the experimental value and σ_i^{theo} is the calulated uncertainty. The three calibration half-lives were known experimentally to equal precision and therefore these uncertainties were not included in the χ^2. First a total time interval was assumed, and the half-lives were calculated and compared to their known values. The total interval was then varied until the best agreement (smallest χ^2) between the calculated and known half-lives was achieved. The best total time interval was found to be 189(1) ms. This represents a stepping time of only ≅11 ms.

In Figure 2-2Ø a plot of the extracted peak height as a function of time is shown for the decay of ^{24}Si. This measurement yields a half-life for the β-decay of ^{24}Si of,

$$T_{\frac{1}{2}} = 1Ø3(42) \text{ ms.}$$

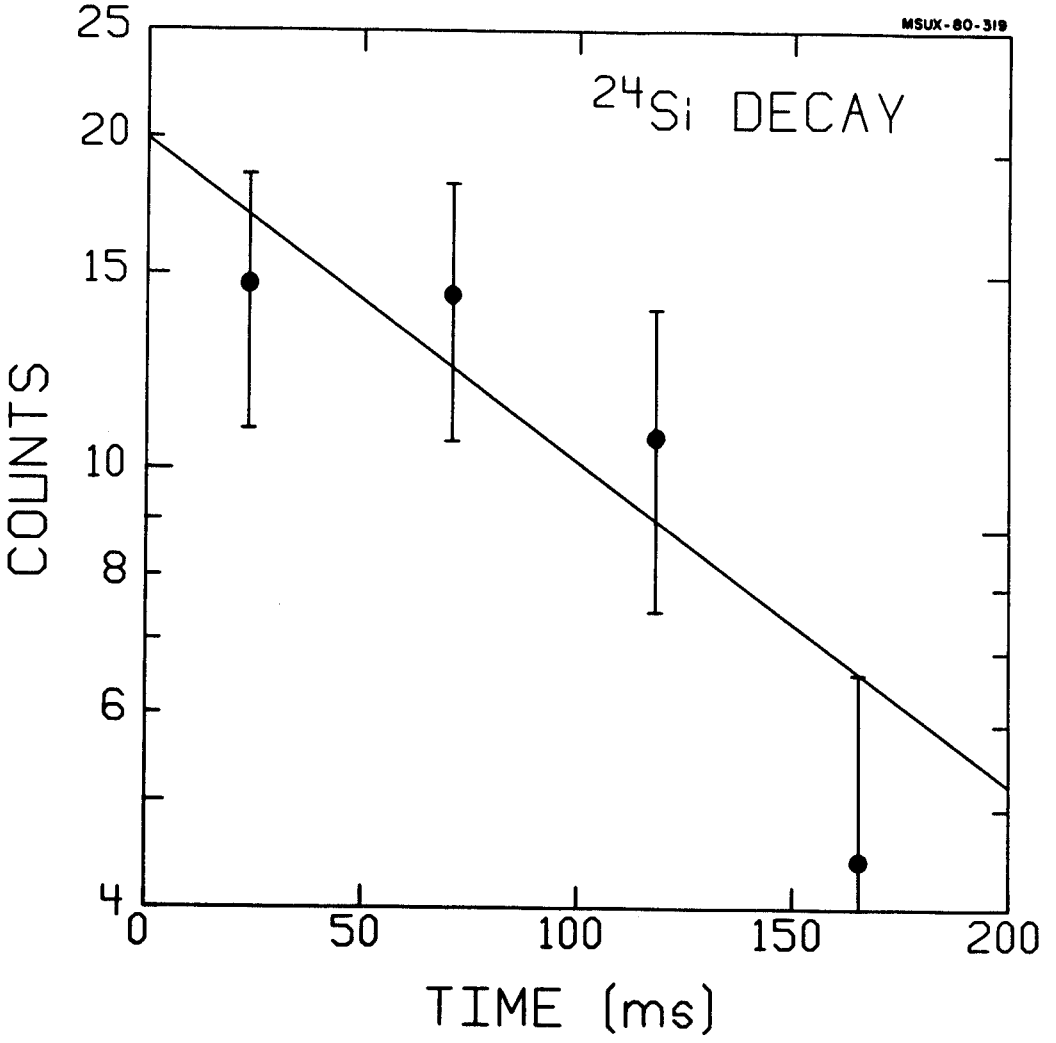

Figure 2-20. Decay of ^{24}Si. The half-life derived is 103(42) ms.

This result is in good agreement with the predicted value of 115 ms, based on a shell model calculation by Robertson and Wildenthal (Ro73). It is also in good agreement with the estimate of 100^{+90}_{-40} ms made by Äystö et al (Ay79).

CHAPTER THREE

3.1 Introduction

The A=8 isobaric quintet is of special interest in that it is the only completed quintet which shows a slight deviation from the quadratic form of the IMME. Figure 3-1 shows the residuals (M_{exp}-M_{IMME}) of the quadratic IMME fit for the A=8 isobaric quintet. These values were derived following the remeasurement of the ^{6}He mass excess (Ro78). It can be seen that a small but significant departure from the IMME exists. Isospin mixing in the T_z=Ø member of the multiplet (^{8}Be) has been suggested as a possible cause for part of this deviation (Ro76). For quintets, as previously discussed, mixing with T=Ø or T=1 states immediately causes a T_z^4 dependence in the IMME (see Figure 1-2). To understand these effects further, a remeasurement of the T=2 levels in ^{8}Be and ^{8}Li was undertaken at the Michigan State University Cyclotron Laboratory.

The first observation of the lowest T=2 level in ^{8}Be was made by Black et al. (Bl69). This was observed as a narrow resonance using the ^{6}Li(d,p)^{7}Li and ^{6}Li(d,α)^{4}He reactions. A more precise measurement was subsequently carried out by Robertson et al. (Ro75). This work verified

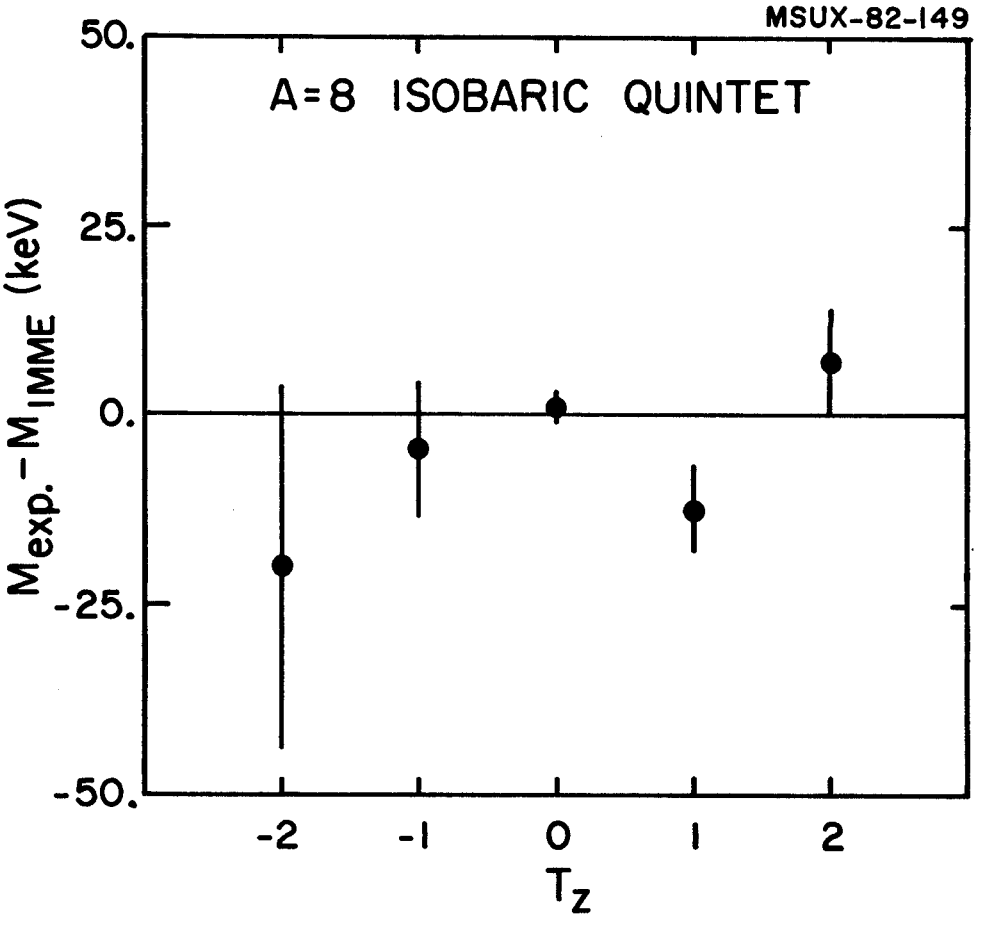

Figure 3-1. Residuals for the quadratic IMME fit to the A=8 quintet (Ro78).

the assignment of the resonance as a $\emptyset^+$ T=2 state (the angular distribution displayed a prominent L=Ø shape). The $^{10}Be(p,t)^{8}Be$ reaction was used for that work and serves as the basis for our new measurement. A measurement of the radiative width of this level by Noé et al. (No76) using the $^{6}Li(d,\gamma)^{8}Be$ reaction provided a value for the excitation energy of comparable precision.

The only measurement of the lowest T=2 level in ^{8}Li was made by Robertson et al. (Ro75) using the $^{10}Be(p,^{3}He)^{8}Li$ reaction.

In the previous measurements by Robertson et al. (Ro75), the reactions were analyzed using an Enge split-pole magnetic spectrograph, and the reaction products were observed using a position-sensitive Si detector placed in the focal plane of the spectrograph. The spectrograph field was set to place the reactions of interest onto the active region of the detector and then was successively changed to place the calibration reactions on the detector. This required an accurate magnetic calibration of the spectrograph (Tr71).

An alternative approach, developed by Nolen, Hamilton, Kashy and Proctor (No74), is to use nuclear emulsions in the focal plane of the spectrograph. The advantage in this method is that the necessary calibration lines can be recorded simultaneously with the reaction of interest. This helps reduce some of the systematic errors that are associated with sequential measurements, such as changes in

the beam energy, spectrograph saturation and hysteresis effects as well as changes in the target thickness resulting from deterioration or a build up of contamination. In addition, this approach enables a linearized least squares fit to be performed to determine all the unknowns in the experiment (assuming sufficient calibration lines are available). These unknowns are the beam energy, the reaction angle, and the spectrograph focal plane calibration.

Photographic emulsions are more linear and more stable than counters and they provide better position resolution than that which is obtainable with electronic detectors (at best Ø.25 mm). There are, however, several drawbacks to using emulsions. These drawbacks include poor particle identification properties, poor saturation characteristics (overexposure) and the inability to display the data in real time as is possible with electronic detectors.

Though there usually is some observable difference in the track density between different types of ionizing particles, this difference cannot be relied on in most cases to observe a low cross section reaction in a high background environment. A partial way around this particle identification difficulty was worked out by Robertson et al. (Ro78a) through the development of an electrostatic deflector which fitted in the gap of the Enge split-pole spectrograph. Figure 3-2 shows the location of the deflector in the spectrograph.

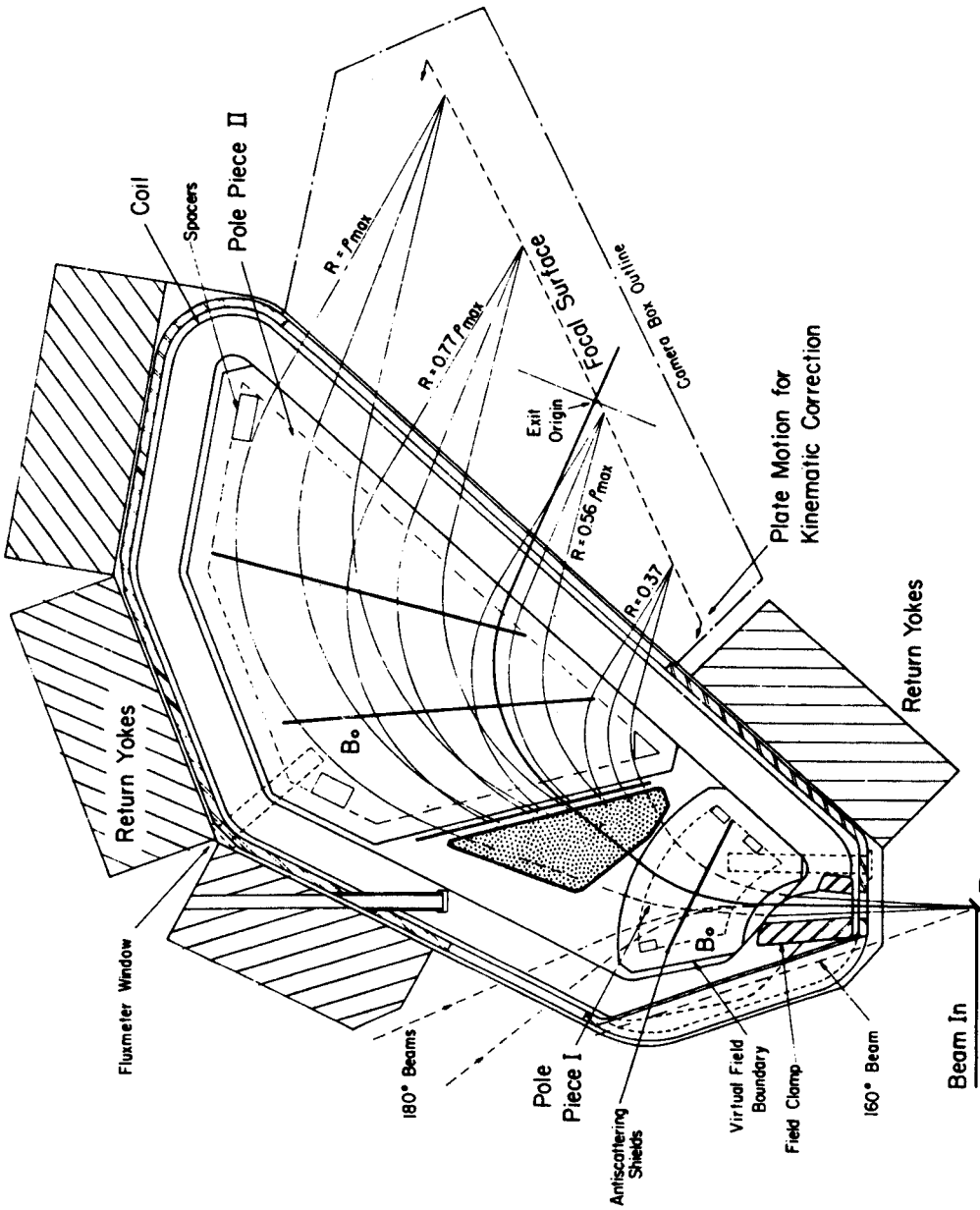

Figure 3-2. Cross-sectional view of Enge split-pole magnetic spectrograph, showing electrostatic deflector (stippled area) used to separate particle types.

The deflector plates were oriented parallel to the pole faces and provided a vertical deflection of the particles. The shape of this deflector was designed so that, to good approximation, the deflection of the particles is constant along most of the focal plane. For particles of the same magnetic rigidity, the vertical deflection is proportional to m/q where m is the mass and q is the ionization state of the particle. In general, the deflection at the high-rho end of the spectrograph is approximately 10.0(Vq/E) mm, where V is the applied voltage in kV, and E is the kinetic energy of the particle in Mev (Ro78a). This deflection resulted in tracks in the emulsion that were vertically separated into bands along the plate according to the m/q of the reaction products. For this method to be of use, small vertical beam spots are required. So care must be taken to focus the beam onto the target. The deflector would of course not be of use if particles of the same m/q from some other reaction fall on the peak of interest.

Figure 2-2 shows the beamline arrangement to the spectrograph (located in vault 3). The dipole magnets M3 and M4 served to analyze the beam energy and the dipole M5 directed the beam to the spectrograph. The quadrupoles (labeled Q7, Q8, etc.) focused the beam on the target.

The beamline to the spectrograph was designed (B171) so that the beam could be brought to a dispersed focus at the target of the spectrograph. By matching the dispersion of the beam to the dispersion produced by the spectrograph, the

line widths in the focal plane could be significantly reduced (Co59). A depiction of a dispersion matched condition is shown in Figure 3-3. Rays leaving the target from the E+ΔE side have a larger radius of curvature (as a result of their higher energy) but because they are physically displaced as shown they move towards the central ray of energy E. The E-ΔE rays with their smaller radius of curvature will also move towards the central ray because they leave the target from the opposite side of the central E ray.

3.2 Experimental Procedure.

A 45 Mev beam of protons from the MSU cyclotron bombarded a 113 $\mu g/cm^2$ target of 94% enriched ^{10}BeO on a 1 mg/cm^2 Pt backing. This was the same target as was used in the previous work by Robertson et al. (Ro75). The target material was produced in the Oak Ridge high-flux isotope reactor via the $^{13}C(n,\alpha)^{10}Be$ reaction (Go74).

The proton beam was used to populate the T=2 states in ^{8}Be and ^{8}Li via the (p,t) and (p,^{3}He) reactions respectively. Tritons, deuterons, and helium 3 reaction products were recorded on 20-inch photographic plates (Il74) mounted in the focal plane of the Enge split-pole spectrograph. Deuterons were recorded simultaneously with the tritons and were used as calibrations in the $^{10}Be(p,t)$ experiment. In the $^{10}Be(p,^{3}He)$ experiment only the ^{3}He spectrum was used. Two sets of exposures were made at

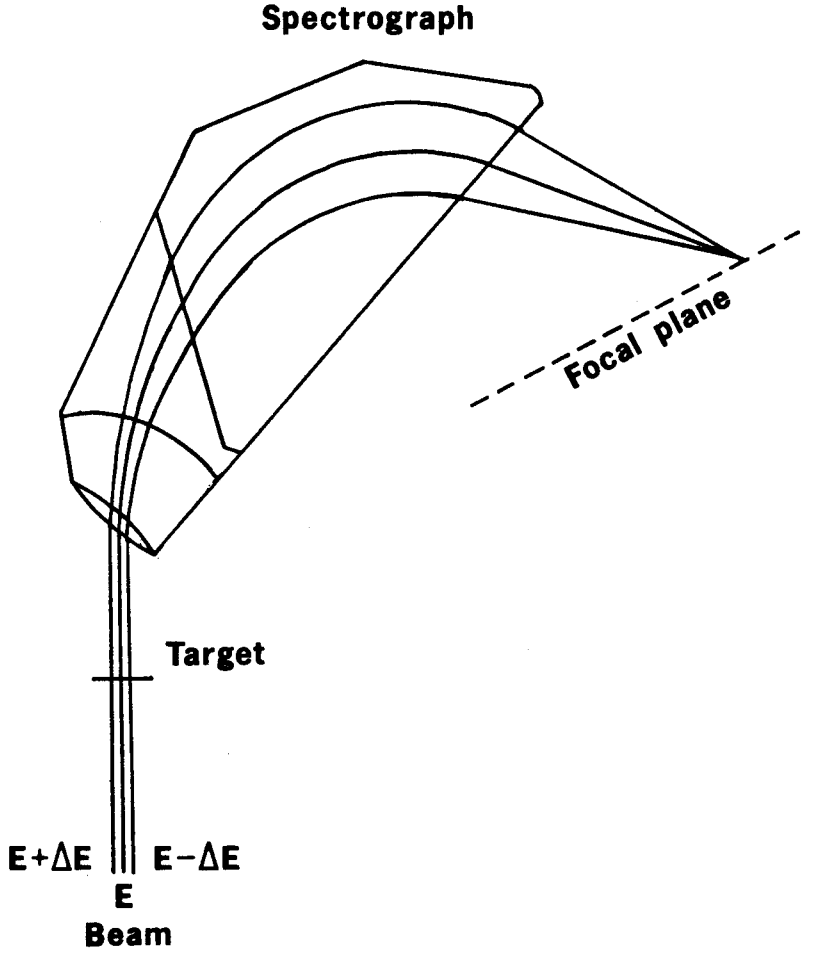

Figure 3-3. Dispersion matching in the spectrograph.

laboratory angles of 8, 9, and 10 degrees. The electrostatic deflector was run at a negative 20 kV potential on the upper plate (deflecting the positively charged ions upward).

The spectrograph focal plane is angled at 45 degrees relative to the particle trajectories (see Figure 3-2). Particles entering the photographic emulsions do so at 45 degrees with respect to the surface. After development, the particle paths appear as small tracks under the microscope. The brightness and density of the tracks depend on the ionization properties of the particles. Because the ionization of a charged particle increases as it slows down, absorbers were placed in front of the emulsion to lower the particle energy. A 0.002-inch (50-micron) Al foil was used with both the helium 3 and triton plates while an additional 0.02-inch (0.5-mm) acetate absorber was used with the tritons. This enhanced the visibility of the particle tracks.

The plates were developed in a dilute solution of D-19 developer at 4°C. They were scanned using the automatic plate scanner developed at MSU by Robertson and Nolen (Ro73a). This scanner uses an analog approach to the problem of track identification rather than the more common digital one (Er79). Tracks are imaged onto a three-segment diode array through a rectangular aperture (0.6 μm × 25 μm) oriented paralled to the tracks. Bright-field illumination is provided by a high-intensity xenon arc lamp filtered by

three infrared filters and a Kodak blue-green gelatin filter.

Automatic focusing is maintained with a motor drive connected to the fine focusing knob of the microscope. This is controlled via a pressure-sensing arrangement that keeps the objective lens at a constant distance from the emulsion.

The scanning was done in Ø.ØØ1-inch (25.4-μm) steps with vertical bands that were 4 mm wide. Only a 1Ø-inch segment of the plates could be scanned at one time, so it was necessary to scan the 2Ø-inch plates in two segments.

The plate holder moves in a rectangular grid pattern with tracks passing across the diode array vertically. As the tracks pass across the aperture the light reaching the diode array is reduced. This signal is inverted and sent to the scanner electronics. When these signals are viewed on an oscilloscope a track event registers as a peak in the trace. For valid track identification several criteria must be satisfied simultaneuosly. These include the signal height, its duration, rise time and centering on the diode array. If all these requirements are satisfied a valid track count is recorded at the current position in the scan. These counts form a histogram of the band of tracks along the plate. The reliability of the system has been elicited in a number of comparisons with hand scanned spectra (Ro81).

Data for both the ^{8}Be and ^{8}Li experiments were recorded sequentially during the same runs. Two plates were placed in the focal plane one above the other. The spectrograph

angle and the field were set for a given reaction and one plate was exposed. Then the field was changed for the other reaction and the plate holder moved so the other plate could be exposed. Running these experiments together enabled the use of the beam energies determined in the triton exposures to be used in the helium 3 experiment. This was necessary because the observation of only the (p,^{3}He) reaction in the ^{8}Li experiment did not provide the needed decoupling of the beam energy and the spectrograph angle. Therefore, an average beam energy was used for the analysis of the ^{3}He data. The Q value showed little sensitivity to the beam energy so this procedure was not a problem.

3.3 Analysis

Spectra from the plates are shown in Figures 3-4 and 3-5. Higher energy particles are at lower channel number. The resolution obtained is 25-35 keV FWHM. Figure 3-4 contains both the deuteron band and the triton band (that were collected simultaneously during the exposure). The deuteron band contains some additional peaks from reactions in the platinum backing. These are the unlabeled peaks at low channel number. The labeled peaks indicate the calibrations used in determining the energy of the T=2 state. The ordering is according to increasing channel number.

The peaks in the deuteron spectra numbered 1, 5, 6, and 14 show a reduction in counts near their centers. This is

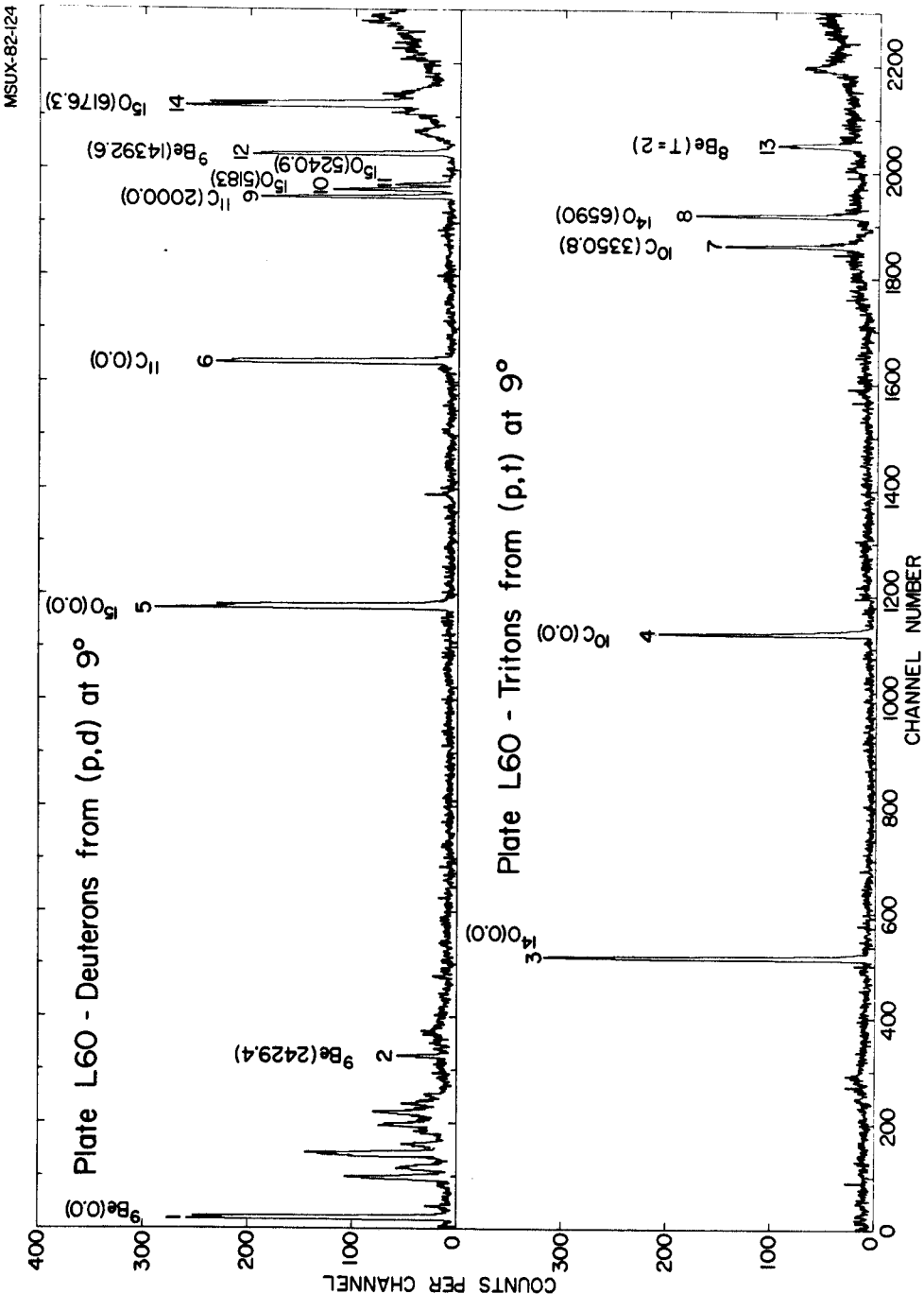

Figure 3-4. Scan of plate L60. Spectrum of deuterons from (p,d), top, and tritons from (p,t), bottom, at 9 degrees.

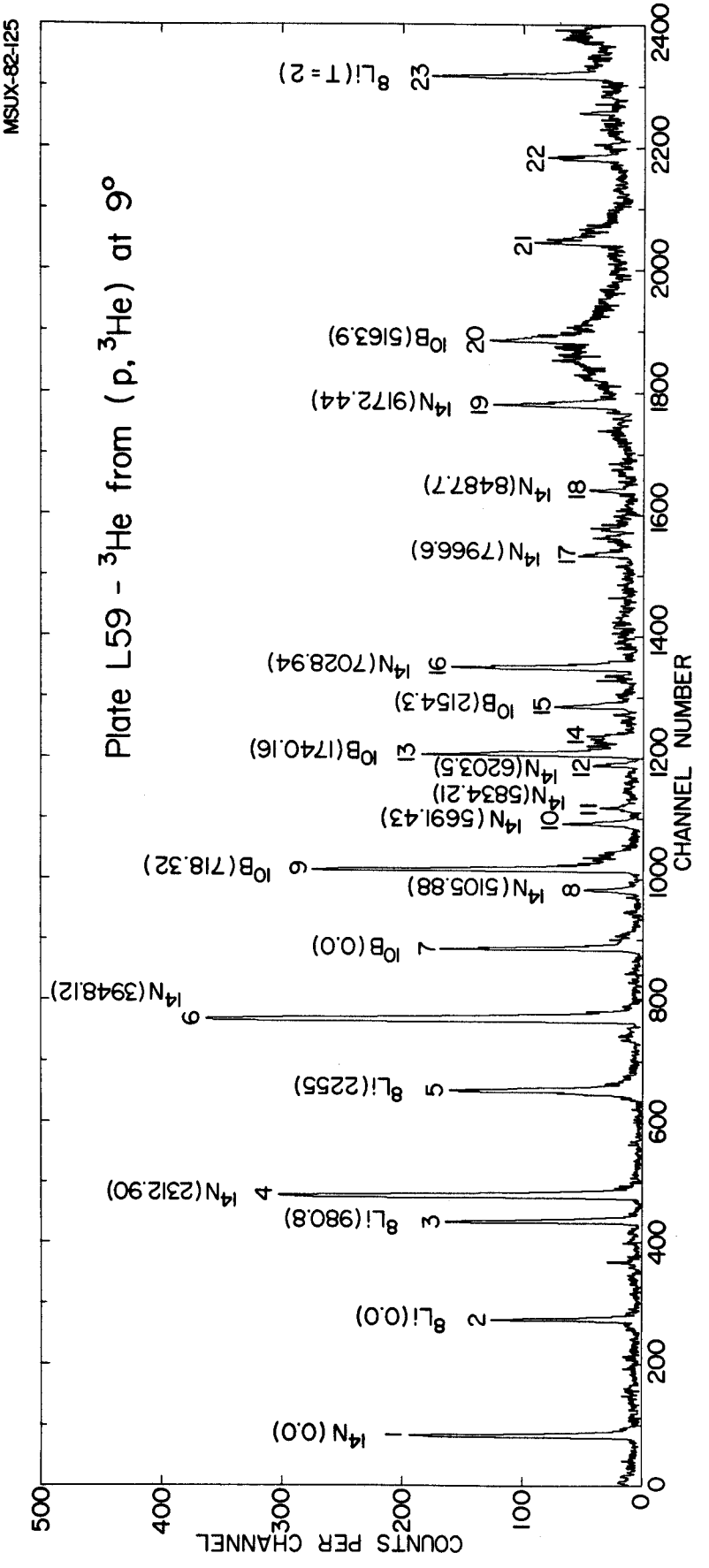

Figure 3-5. Scan of plate L59. Spectrum of helium 3 particles from (p, ^{3}He) at 9 degrees.

caused by the high track density in the center of these groups. The track number becomes so large that a large fraction of the tracks overlap and the scanner electronics can no longer distinguish the individual tracks. The overexposure of these lines was necessary in order to obtain enough statistics in the T=2 state.

A specialized peak fitting routine was written to determine the centroids of the "burned-in" peaks. This program performs a peak fit with a symmetric three-parameter gaussian with a background that could include constant, linear or quadratic terms. The code allowed the removal of the central portion of the peak from the fit. The method of maximum likelihood was used to find the best fit and to determine the centroid uncertainty.

The use of the maximum likelihood method was necessitated by the discovery that a chi-squared minimization method did not produce realistic centroid uncertainties for fits to the burned-in peaks. This was determined by testing with normal peaks that had their center regions removed. As more channels were left out of the fit, the resulting centroid uncertainties decreased. Because less information should not produce greater certainty in the results, a different approach to the calculation of the centroid uncertainties was tried. Integrating the likelihood distribution with respect to the centroid provided a reliable estimate of the centroid uncertainty. See Appendix C for a discussion of the method of maximum

likelihood.

In addition to three-parameter symmetric gaussians, an attempt was made to fit the peaks with functions containing more parameters. This was done in the hope that the slightly asymmetric nature of the peaks would be better fit with a distribution that could include this asymmetry. Four- and five-parameter functions were tried but the extra parameters produced unrealistic peak shapes. So only fits with three parameters were used in the final analysis. Because of the inability to obtain realistic peak shapes with the four- and five-parameter functions, it was not possible to determine if a systematic error was present when the fitting was done with the three-parameter functions. However, because of the large number of calibration lines on each plate, as well as the number of plates used in the analysis, the deviations should average out. Furthermore, if a constant centroid shift were introduced, the relative peak separations would not change and the shift would have no effect. No additional uncertainty will be introduced to account for this possible effect.

DOALL, a code developed at MSU by Hamilton and Vance (Ha74), was used to determine the Q values. This program performs an energy calibration on a given spectrum. It utilizes a linear chi-squared minimization procedure on designated calibration lines with accurately-known reaction excitation energies to calculate changes in the beam energy (ΔE) and spectrograph angle ($\Delta\theta$) while simultaneously

calculating the parameters for the relation between the effective radius of curvature ρ and the particle position D, along the focal plane of the spectrograph. Measurement of the spectrograph magnetic field, combined with the effective radius of curvature, enables the determination of the particle energy. This code then calculates accurate excitation energies and Q values from the fit parameters.

Nominal values for the magnetic rigidity, $(B\rho^i)_0$ for a given line i are provided from calibration of the beam analyzing system. The analyzing system determined the beam energy to ≅1ØØ keV. The spectrograph angle was known nominally to Ø.2 degrees. DOALL calculates corrections to the nominal values of the beam energy E_0 and the scattering angle Θ_0 and applies these to an actual value of $B\rho^i$ using the first order expansion,

$$B\rho^i = (B\rho^i)_0 + \frac{\partial(B\rho^i)}{\partial E}\Delta E + \frac{\partial(B\rho^i)}{\partial \Theta}\Delta\Theta \qquad (3\text{-}1)$$

The relation between ρ and D is usually expressed in terms of an expansion around an arbitrary point and takes into account the nonlinear relationship between these quantities.

$$\rho^i = \rho_0 + \alpha(D^i - D_0) + \beta(D^i - D_0)^2 \qquad (3\text{-}2)$$

This can then be related to the magnetic rigidity as

$$B\rho^i = B\rho_0 + B\alpha(D^i - D_0) + B\beta(D^i - D_0)^2 \qquad (3\text{-}3)$$

The ρ_0, α, and β are the unknowns of the spectrograph calibration. Combination of equations 3-1 and 3-3 results

in an expression for each calibration line which contains five unknowns.

$$(B\rho^i)_o = -\frac{\partial(B\rho^i)}{\partial E}\Delta E - \frac{\partial(B\rho^i)}{\partial\theta}\Delta\theta + B\rho_o + \\ + \alpha B(D^i - D_o) + \beta B(D^i - D_o)^2 \qquad (3\text{-}4)$$

With five or more appropriately-chosen calibration lines it is then possible to determine these unknowns. Once the chi-squared minimization procedure determines the best values for these unknowns the energy and Q value of the reaction of interest can be obtained (No73).

Table 3-1 contains the excitation energies used in the analysis (Aj79,Aj80,Aj81). Recent high precision measurements (Bi81,Ba82) of states in ^{14}N were combined in quadrature with the compilation of Ajzenberg-Selove (Aj81). These are shown in Table 3-2. The Q values used in the analysis were those calculated from the 1981 mass tables of Wapstra and Bos (Wa81).

The weighting for each calibration line included both the centroid uncertainty from the peak fitting routine taken in quadrature with the excitation energy uncertainty. The excitation energy was first converted to channel number via the first order conversion between energy and channel number along the focal plane. In the compressed spectra the energy/channel number conversions for ^3He, d, and t were 5.0, 6.9, and 4.5 keV/channel respectively.

The target thickness and uniformity were determined using the alpha particle backscatter technique (Fo77a,Ro82).

Table 3-1 Calibration excitation energies for the ^{8}Li and ^{8}Be experiments.

Nuclide	Excitation Energy(keV)	Peak Numbers in Spectra
^{8}Li Experiment		
^{14}N	Ø.Ø	1
	2312.9Ø(3)	4
	3948.12(18)	6
	51Ø5.88(15)	8
	5691.43(12)	1Ø
	5834.21(16)	11
	62Ø3.5(6)	12
	7Ø28.94(13)	16
	7966.6(6)	17
	8487.7(12)	18
	9172.44(3Ø)	19
^{8}Li	Ø.Ø	2
	98Ø.8(1)	3
	2255.(3)	5
	1Ø822.2(55)	23
^{10}B	Ø.Ø	7
	718.32(9)	9
	174Ø.16(17)	13
	2154.3(5)	15
	5163.9(6)	2Ø
^{8}Be Experiment		
^{15}O	Ø.Ø	5
	5183.(1)	1Ø
	524Ø.9(3)	11
	6176.3(17)	14
^{9}Be	Ø.Ø	1
	2429.4(13)	2
	14392.6(18)	12
^{11}C	Ø.Ø	6
	2ØØØ.Ø(5)	9
^{14}O	Ø.Ø	3
	659Ø(1Ø)	8
^{8}Be	27494.Ø(2Ø)	13
^{10}C	Ø.Ø	4
	335Ø.8(9)	7

Table 3-2 ^{14}N excitation energies.

Excitation Energy (keV) (Aj81)	Excitation Energy (keV) (Bi81)	Excitation Energy (keV) (Ba82)	Weighted Average (keV)
2312.87(7)	2312.90(3)	-	2312.90(3)
3947.8(4)	3948.2(2)	-	2948.12(18)
5105.87(18)	5105.9(3)	-	5105.88(15)
5689.6(11)	5691.55(13)	5690.5(4)	5691.43(12)
5834.23(21)	5834.3(3)	5834.0(4)	5834.21(16)
6203.5(6)	-	-	6203.5(6)
7027.9(14)	7029.4(3)	7028.85(14)	7028.94(13)
7966.6(6)	-	-	7966.6(6)
8487.7(12)	-	-	8487.7(12)
9170.7(16)	9172.5(3)	-	9172.44(30)

A 3 MeV alpha beam, from the single-ended Van-de-Graaff at Los Alamos National Laboratory, was used in the measurement. Alpha particles were backscattered off the platinum target backing. The energy shift and width of the high energy side of the Pt backscatter peak (with particles passing through the BeO layer) showed that the target was quite uniform (though the platinum backing appeared not to be). The measured target thickness of 113 $\mu g/cm^2$ was in excellent agreement with a previous measurement of 114 $\mu g/cm^2$ by Robertson et al. (Ro75).

To account for energy loss in the target, corrections were made to the excitation energies corresponding to the calculated energy loss for each reaction in the target. The program SPECTKINE IV, developed at MSU by Trentelman, Robertson, Gleitsmann and Robinson (Tr76b) contained the calibration of the beam transport system and calculated the particle energies for the reactions. The energy loss for each reaction was then calculated using the stopping power tables from Saclay (Wi66). An average beam energy was used in this calculation, and the particle energies were determined for a scattering angle of 9 degrees. Energy loss corrections for the deuterons and tritons were between Ø to 4 keV while those for ^{3}He were between Ø to 13.2 keV.

The 1981 mass tables have not as yet been incorporated into the library of the MSU computer system. Therefore, to take into account the new Q values, it was necessary to enter corrections to the excitations energies used in the

calibration. For a given reaction, the ground state as well as all the excited states were corrected with the negative of the Q value change (1981-1977).

Table 3-3 lists the ground state mass excesses that are needed in the calibration reactions (Wa77,Wa81). There currently exist some discrepancies between the adopted values and some recent high resolution mass measurements. In particular the masses of ^{14}O and ^{10}C are in doubt. Unpublished measurements by Barker and Nolen (Ba82a), differ by several keV from the 1977 and 1981 mass tables (see Table 3-3). An additional and independent measurement of the ^{10}C-^{14}O mass difference (see footnote in Table 3-3), also by Barker and Nolen, is consistent with the mass difference extracted from their individual mass measurements. Table 3-4 lists the Q values based on the 1981 and 1977 mass tables for all the ground state reactions in the experiments. The Q value changes using the Barker and Nolen mass excesses are also listed. An analysis of the ^{8}Be data using these alternate values produced a change in the ^{8}Be T=2 Q value of less than Ø.13 keV. These masses were not used in the ^{8}Li measurement, and so had no effect on the Q value in that case.

3.4 Results

The deviation of the Q values (about their unweighted average) derived from individual plate exposers, from the ^{8}Be and ^{8}Li experiments are shown in Figures 3-6 and 3-7.

Table 3-3 1977 and 1981 mass excesses.

	Mass Excess 1977	Mass Excess 1981	Difference (1981-1977)	Difference (Nolen-1977)
^{1}H	7289.Ø34(23)	7289.Ø28(23)	-Ø.ØØ6	-
^{2}H	13135.84(4)	13135.823(42)	-Ø.Ø17	-
^{3}H	14949.94(5)	14949.91Ø(52)	-Ø.Ø3Ø	-
^{3}He	14931.32(5)	14931.311(52)	-Ø.ØØ9	-
^{8}Li	2Ø946.9(9)	2Ø945.312(787)	-1.588	-
^{8}Be	4941.76(1Ø)	4941.696(1Ø5)	-Ø.Ø64	-
^{9}Be	11348.Ø(4)	11347.6ØØ(397)	-Ø.4ØØ	-
$^{1\,0}Be$	126Ø7.6(6)	126Ø6.869(412)	-Ø.731	-
$^{1\,0}B$	12Ø51.7(5)	12Ø5Ø.Ø42(393)	-1.658	-
$^{1\,0}C$	157Ø2.9(7)	157ØØ.472(394)	-2.428	-2.71(47)[a]
$^{1\,1}C$	1Ø65Ø.Ø(11)	1Ø649.287(435)	-Ø.713	Ø.Ø1(29)
$^{1\,2}C$	Ø.Ø	Ø.Ø	-	-
$^{1\,4}N$	2863.444(23)	2863.43Ø(24)	-Ø.Ø14	-
$^{1\,4}O$	8ØØ8.3(5)	8ØØ6.563(81)	-1.737	Ø.35(51)[a]
$^{1\,5}O$	2855.4(7)	2855.45Ø(63Ø)	Ø.Ø5Ø	-
$^{1\,6}O$	-4737.Ø2(4)	-4737.Ø48(47)	-Ø.Ø28	-

[a] Calculated $^{1\,0}C$-$^{1\,4}O$ mass difference relative to the 1977 mass table is 3.Ø6(42) keV. Measured mass difference is 3.44(27) keV (Ba82a).

Table 3-4 1977 and 1981 Q values.

Reaction	Q Value 1977 Mass Table	Q Value 1981 Mass Table	Difference 1981-1977	Difference Nolen-1977
$^{16}O(p,t)^{14}O$	-20406.226(504)	-20404.493(110)	1.733	-0.354
$^{12}C(p,t)^{10}C$	-23363.806(702)	-23361.354(398)	2.452	2.734
$^{10}Be(p,t)^{8}Be$	4.934(611)	4.291(429)	-0.643	-
$^{16}O(p,d)^{15}O$	-13439.226(703)	-13439.293(634)	-0.067	-
$^{12}C(p,d)^{11}C$	16496.806(1101)	-16496.082(1436)	0.724	0.001
$^{10}Be(p,d)^{9}Be$	-4587.206(723)	-4587.526(574)	-0.320	-
$^{16}O(p,^{3}He)^{14}N$	-15242.750(072)	-15242.761(78)	-0.011	-
$^{12}C(p,^{3}He)^{10}B$	-19693.986(503)	-19692.325(397)	1.661	-
$^{10}Be(p,^{3}He)^{8}Li$	-15981.586(1083)	-15980.726(890)	0.860	-

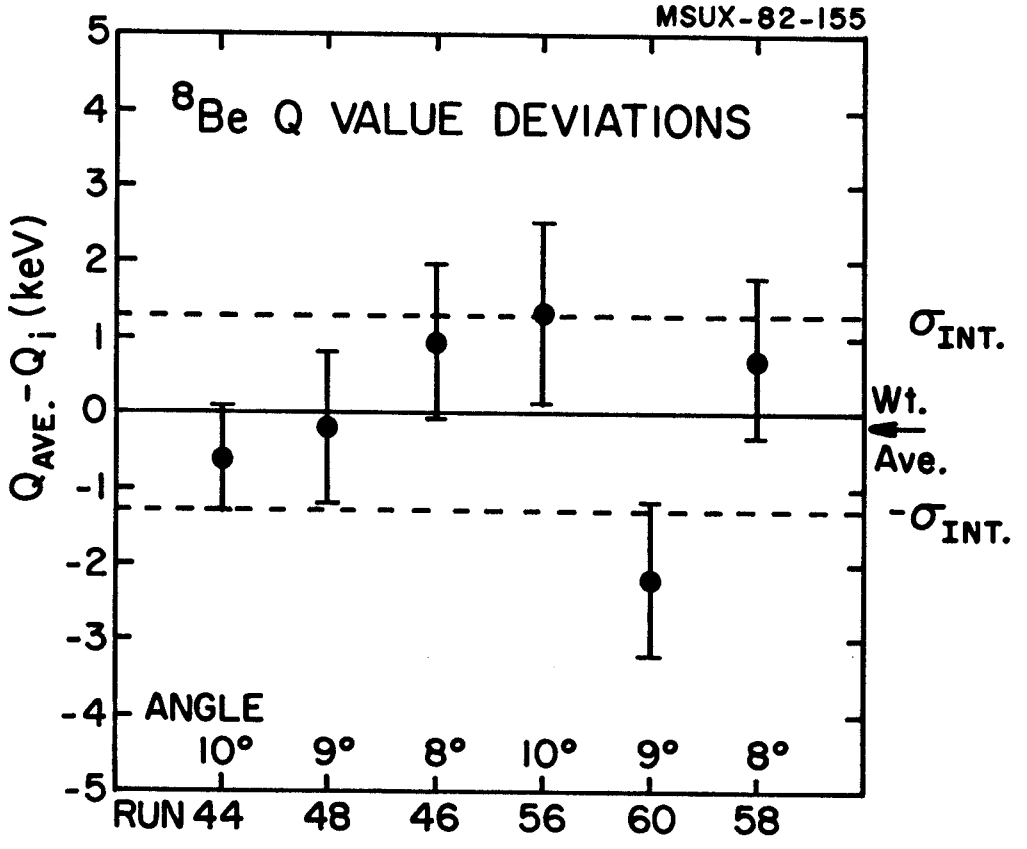

Figure 3-6. Deviations of the ^{8}Be Q values from their unweighted average.

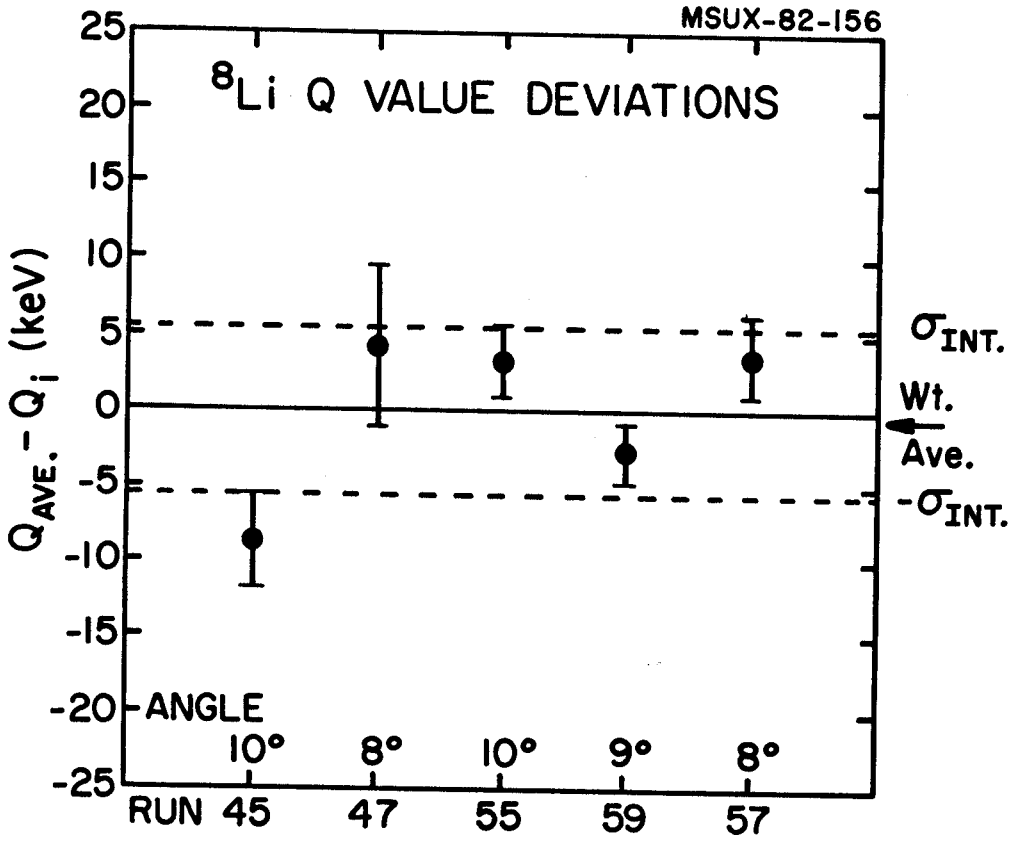

Figure 3-7. Deviations of the ^{8}Li Q values from their unweighted average.

In the ^{8}Li data, one 9-degree run was not included because of an incorrect setting of the spectrograph field which placed the T=2 state off the end of the plate. The uncertainty for each value is from a sum (in quadrature) of the centroid uncertainty (from the peak fitting routine) and the uncertainty in the excitation energy (calculated in DOALL from the variance-covariance matrix). The difference between a weighted and unweighted average of these data is also shown in the figures. The standard deviation of the data points (internal error) is shown as dotted lines in these figures. The weighted average falls well within the internal spread of the data. The unweighted average of the Q values is adopted for the final result. For the ^{10}Be(p,t)^{8}Be reaction the Q value is

-27484.3(14) keV.

For the ^{10}Be(p,^{3}He)^{8}Li reaction the Q value is

-26821.3(57) keV.

Table 3-5 contains a list of the major uncertainties in the measurements. All the uncertainties were taken in quadrature to yield the errors quoted above.

For the ^{8}Be experiment there are four ground state Q values that could change:

$$Q_1 = {}^{12}C(p,d)^{11}C$$

$$Q_2 = {}^{10}Be(p,d)^{9}Be$$

$$Q_3 = {}^{16}O(p,t)^{14}O$$

$$Q_4 = {}^{12}C(p,t)^{10}C.$$

Future corrections to our Q value will be approximately

Table 3-5 Contributing uncertainties to the Q value measurements.

	^{8}Be(T=2) ΔQ(keV)	^{8}Li(T=2) ΔQ(keV)
A 10% uncertainty in ^{10}BeO	0.30	0.42
A possible 10 μg/cm^2 carbon layer	0.23	0.45
25 keV shift in beam energy for ^{8}Li experiment	-	0.32
10% uncertainty of the relative shift between d and t from deflector	0.04	-
Uncertainty in appending two halves of the scans together; 1/16 channel shift to all peaks $\geq$ 1200 channels	0.12	0.47
Barker and Nolen Q values (Table 3-4)	0.13	-
Uncorrelated Q value uncertainty from $\left[\sum_i \left(\frac{\partial Q}{\partial Q_i}(T=2)\right)^2 \sigma_{Q_i}^2\right]^{\frac{1}{2}}$ (Partials from Equations 3-5 and 3-6. Q value uncertainties from Table 3-4.)	0.43	0.72
Internal errors (See Figures 3-6 and 3-7)	1.28	5.56
Total sum in quadrature	1.41	5.67

$$\Delta Q=(\emptyset.59)\Delta Q_1+(\emptyset.1\emptyset34)\Delta Q_2+(\emptyset.\emptyset25)\Delta Q_3+(1.\emptyset217)\Delta Q_4 \qquad (3\text{-}5)$$

where ΔQ's are defined as $Q_{New}-Q_{Old}$.

For the ^{8}Li experiment the qround state Q values subject to change are

$$Q_1={}^{12}C(p,{}^{3}He)^{10}B$$

$$Q_2={}^{10}Be(p,{}^{3}He)^{8}Li.$$

Possible corrections to our value will be approximately

$$\Delta Q=(\emptyset.372)\Delta Q_1+(\emptyset.67)\Delta Q_2. \qquad (3\text{-}6)$$

Equations 3-5 and 3-6 are based on the approximation that small Q value changes may be taken as independent. These expressions give the change in our result as a function of calibration Q value changes. The coefficients are partial derivatives calculated by making 1 keV changes to the calibration Q values and taking the difference of the averages for all the runs before and after the change. This sum of partial derivatives works quite well and gives reasonable results even when several values are changed at once.

The Q values from the measurement of Robertson et al. (Ro75) are -27487.6(26) and -268Ø4.1(54) keV for the reactions $^{10}Be(p,t)^{8}Be(T=2)$ and $^{10}Be(p,{}^{3}He)^{8}Li(T=2)$ respectively. Comparison of our values with these previous results shows a fairly good agreement between the ^{8}Be

measurements. For the ^{8}Li Q value, however, our new value is 17.2 keV below the older measurement. The calibration Q values used in the Robertson analysis have only changed by a few keV and are not the cause of this discrepency. Because of the introduction of the additional calibration lines as well as the non-sequential aspect of the new measurements, it may be argued that only the new values should be adopted.

The mass excess for the T=2 state in ^{8}Be (based on our new Q value of -27484.3(14) keV for the reaction ^{10}Be(p,t)^{8}Be) is

32430.4(15) keV.

The resonance energy for the reaction ^{6}Li(d,γ)^{8}Be(T=2) by Noé et al. is E_d=6962.8(30) keV. This measurement is based on an accelerator energy calibration of E_p=14230.75(20) keV from the resonance reaction ^{12}C(p,γ)^{13}N(T=3/2) (Aj81). This calibration has not changed, so just using the E_d resonance energy and the 1981 mass table to recalculate the Q value, the T=2 ^{8}Be mass excess becomes 32435.7(23) keV.

A weighted average of the mass excesses obtained from the resonance experiment of Noé et al. and from our (p,t) work is 32432.0(13) keV. Because these two values are two standard deviations apart, the approach of the particle data group (Ba70) has been adopted. Namely, the uncertainties of the measurements have been scaled to bring the reduced chi-squared to unity. The resulting change is only in the size of the error and does not affect the value of the average. The adopted mass excess for the T=2 state in ^{8}Be

is then

32432.Ø(24) keV.

The ^{8}Li T=2 mass excess (based on the Q value from our new measurement -26821.3(57) keV and the 1981 mass tables) is

31785.9(57) keV.

Chapter Four contains a discussion of the effect of these new results on the IMME fit to the A=8 quintet.

CHAPTER FOUR

4.1 A=24 Quintet

In the A=24 quintet, the mass of the T_z=2 nucleus ^{24}Ne was measured by Silbert and Jarmie (Si61) using the ^{22}Ne(t,p)^{24}Ne reaction. The most accurate measurement of the lowest T=2 state in ^{24}Na was made by Start et al. (St73) via the ^{22}Ne(^{3}He,pγ) reaction. The lowest T=2 level in ^{24}Mg was first observed in the ^{26}Mg(p,t) reaction by Garvey, Cerny and Pehl (Ga69). It has subsequently been studied as an isospin-forbidden resonance in the ^{23}Na(p,γ) reaction by Riess et al. (Ri67), by Szucs, Underwood, Alexander, and Anyas-Weiss (Sz73), and by Heggie and Bolotin (He77).

The T=2 level in ^{24}Al was first observed by Äystö et al. (Ay79) using the ^{24}Mg(^{3}He,3n)^{24}Si reaction. The ^{24}Si activity was transported via helium jet to an on-line mass separator system. Mass-24 activity was deposited in front of a ΔE-E telescope and the energy of protons from the T=2 level in ^{24}Al (populated by the beta-decay of ^{24}Si) were measured. This level has subsequently been measured using the same reaction (see Chapter Two and Le8Ø). The observation of ^{24}Si in the ^{28}Si(^{4}He,^{8}He) reaction by Tribble et al. (Tr8Ø) brings this quintet to completion.

In the A=24 multiplet some of the mass excesses are

derived from measurements of nuclear reaction Q-values, some from excitation energies and some from proton resonance or decay energies. Considered independently, each of these T=2 state mass excesses includes in its uncertainty the uncertainty in a ground state mass excess. However, mass differences in a local group of nuclides are frequently known more precisely (by direct measurement) than are the absolute mass excesses themselves. It is these mass differences which are relevant in testing the IMME because the higher-order terms are all expressible as mass differences. In other words, the uncertainties in the ground state masses are strongly correlated, and a proper evaluation of the uncertainties in the coefficients of the IMME requires consideration of these correlations.

We therefore return to the original measurements which link the nuclei of interest. Those measurements constitute a practically uncorrelated body of data, although there are small correlations which arise from the use of common calibration lines, e.g., the 6129.17 keV line of ^{16}O. The uncertainties in these calibrations are small enough that their influence can be neglected. We may confine our attention to masses which affect the T=2 states in ^{24}Al, ^{24}Mg and ^{24}Na because the uncertainties in the masses of ^{24}Si and ^{24}Ne, 22 keV and 1Ø keV, respectively, are so large Furthermore, the masses of the T=2 states in ^{24}Al and ^{24}Na are, for all practical purposes, correlated only with the masses of ^{23}Mg and ^{24}Na (respectively), while in ^{24}Mg the

gamma decay energy to the ground state and the proton resonance energy in ^{23}Na(p,γ) are known to comparable precision. In earlier mass evaluations these two independent measures of the mass of the ^{24}Mg T=2 state were consistent, but the 1977 Wapstra-Bos tabulation (Wa77) leads to values obtained in the two types of experiment (Ri67,Sz73,He77) which differ by 5.Ø(24) keV. The origin of this discrepancy is difficult to identify exactly because of the global nature of mass adjustments; however, it appears to lie outside of the local group of masses needed for the present purposes, a group interrelated by several precise and consistent experimental measurements.

This problem in the middle of the s-d shell has been noted by Wapstra and Bos (Wa77). Wapstra (private communication) has carried out an adjustment in which the direct mass spectroscopic data is omitted and the results show reduced closure errors. Furthermore, Wapstra and Bos have published tables of mass differences which have been calculated taking correct account of the correlations between the masses concerned. However, these tabulations do not list the correlations between mass differences, nor do they include the linkage through the T=2 state of ^{24}Mg, i.e., the proton resonance energy and the γ-decay energy, which significantly constrains the ^{23}Na-^{24}Mg mass difference. For these reasons we have adopted a local mass adjustment.

The ground state masses required in the analysis are

^{23}Mg, ^{23}Na, ^{24}Mg and ^{24}Na. In addition, the mass of the T=2 state in ^{24}Mg should be included on the same footing as the ground state masses because it links ^{24}Mg and ^{23}Na.

The data base given in Table 4-1 forms the input for a local least-squares mass adjustment. Each mass is linked to at least two others, and 5 masses are related by 7 mass differences. This is illustrated graphically in Figure 4-1. The solid lines show the 7 connections between the 5 masses and the dotted lines represent the measured proton energies and excitation energies used in determining the T=2 level in ^{24}Al.

The normalized χ^2_ν for the fit is 1.1 (2 degrees of freedom). To obtain actual numerical values for masses we arbitrarily assign ^{24}Mg a mass excess of -13930.6 keV -- all the derived masses are then based on (and fully correlated with) this mass. The resulting ground state mass excesses (along with a comparison to the 1977 mass tables) are listed in Table 4-2. Table 4-3 contains a summary of the T=2 state mass excesses (and their excitation energies) as derived from the local mass adjustment. These masses are used to derive the coefficients of the IMME which are also shown in Table 4-3. The covariances are negligible with the exception of ^{23}Na - ^{24}Na. It should be borne in mind that the masses in Tables 4-2 and 4-3 do not include the ^{24}Mg mass uncertainty (0.7 keV), and that it is this distinction which eliminates the otherwise strong correlation between them. The coefficient (a) is therefore subject to the

Table 4-1 Reaction Q values used in the local mass adjustment.

Reaction	Q values (keV)	References
$^{23}Na(p,\gamma)^{24}Mg$	11691.2(11)	(Wa77)
$^{23}Na(n,\gamma)^{24}Na$	6959.41(12)	(Wa77)
$^{23}Na(p,n)^{23}Mg$	-4839.1(26)	(Wa77)
$^{24}Mg(p,d)^{23}Mg$	-14307.5(15)	(Wa77)
$^{24}Na(\beta-)^{24}Mg$	5514.8(20)	(Wa77)
$^{24}Mg(T=2) \rightarrow {}^{23}Na + p$	3741.2(23)	(Ri67,Sz73)[a]
$^{24}Mg(T=2) \rightarrow {}^{24}Mg + \gamma$	15436.3(6)	(St73,Sz73)[a]

[a] Weighted average of these measurements.

Table 4-2 Mass excesses obtained using the local mass adjustment, and a comparison to the 1977 mass table (Wa77).

Nuclide	Local Adjustment Mass Excess(keV)	1977 Mass Table Mass Excess(keV)
^{23}Na	-9527.7(9)	-9529.6(8)
^{23}Mg	-5470.2(13)	-5470.6(15)
^{24}Na	-8415.6(9)	-8417.5(8)
^{24}Mg	-13930.6[a]	-13930.6(7)
$^{24}Mg(T=2)$	1505.5(6)	-

[a] Assigned reference mass excess.

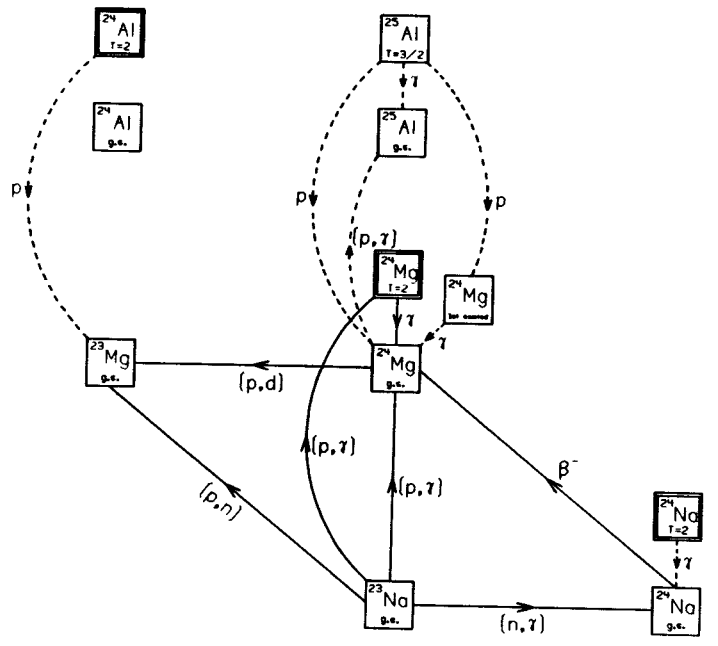

Figure 4-1. Graphical representation of the local mass adjustment. Solid lines are Q value inputs, dotted lines are measured proton energies and calibration excitation energies.

Table 4-3 Summary of the properties of the A=24 isobaric quintet and coefficients of the IMME fits.

Nuclide	T_z	Mass Excess[a] (keV)	Excitation (keV)	References
^{24}Si	-2	10782(22)	0	(Tr80)
^{24}Al	-1	5903.4(40)	5955.4(57)	(Ay79,This work)[b]
^{24}Mg	0	1505.5(6)	15436.1(6)	(Wa77)
^{24}Na	1	-2445.4(13)	5970.2(9)	(St73)
^{24}Ne	2	-5949(10)	0	(Wa77)

a	b	c	d	e	χ^2_ν
1505.5(6)	-4171.6(19)	224.7(18)	-	-	0.9
1505.4(6)	-4174.3(25)	225.0(18)	-1.2(16)	-	1.3
1505.5(6)	-4175.3(20)	223.9(28)	-	0.4(9)	1.7
1505.5(6)	-4171.6(35)	222.1(31)	-2.8(21)	1.4(12)	-

a
Mass excesses of the three inner members of the quintet (Al,Mg,Na) make use of the local mass adjustment. See tables 4-1 and 4-2 for input values. Outer members (Si,Ne) do not.

b
Weighted average of these measurements.

additional uncertainty contributed by the uncertainty in the mass of ^{24}Mg.

Examination of Table 4-3 shows that the quadratic IMME gives a reasonably good fit to the data, with χ^2_ν=Ø.9 per degree of freedom. A plot of the residuals of the quadratic fit is shown in Figure 4-2. Addition of either a cubic or quartic term by itself does not improve the quality of the fit. The uncertainty in the d coefficient, 1.6 keV in the cubic fit, may be compared directly with other d coefficients in both quintets and quartets.

4.2 A=8 Quintet

In the A=8 quintet, the T=2 nucleus ^{8}He was first observed by Cerny et al. (Ce66), using the ^{26}Mg(^{4}He,^{8}He)^{22}Mg reaction. More recently the ^{18}O(^{4}He,^{8}He)^{14}O (Ja74) and ^{64}Ni(^{4}He,^{8}He)^{60}Ni (Ko75a,Tr77) reactions have been used to determine the ^{8}He mass excess. Previous to the work described in Chapter Three, the only measurement of the T=2 state in ^{8}Li was made by Robertson et al. using the ^{10}Be(p,^{3}He)^{8}Li reaction. The T=2 level in ^{8}Be was discovered as a narrow resonance by Black et al. (Bl69), using the ^{6}Li(d,p)^{7}Li and ^{6}Li(d,α)^{4}He reactions. This was later verified by Robertson et al. using the ^{10}Be(p,t)^{8}Be reaction (Ro75). The T=2 state in ^{8}B has only been measured once using the ^{11}B(^{3}He,^{6}He)^{8}B reaction (Ro75). The T=2 nucleus ^{8}C was first observed by Robertson et al. (Ro74), via the ^{12}C(^{4}He,^{8}He)^{8}C reaction. A measurement by Tribble et al.

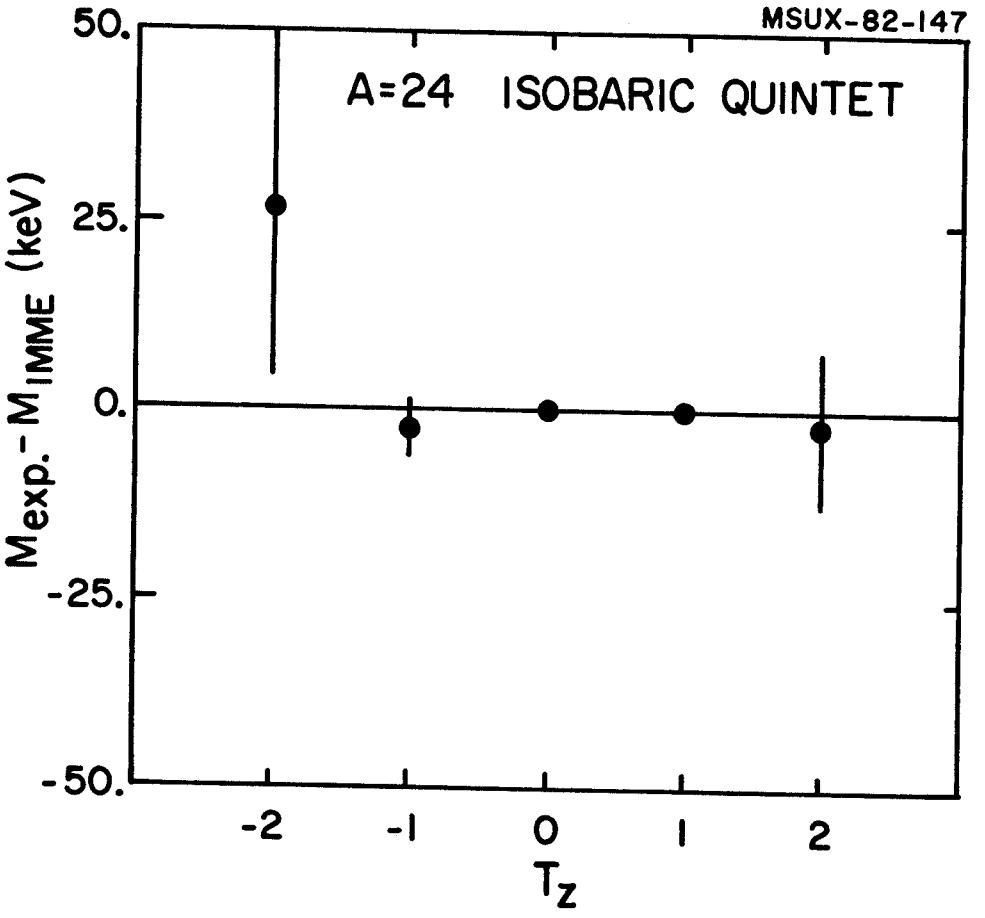

Figure 4-2. Residuals for a quadratic IMME fit to the A=24 quintet.

(Tr76) also used this reaction. A later measurement by Robertson et al. (Ro76), used the $^{14}N(^{3}He,^{9}Li)^{8}C$ reaction to determine the ^{8}C mass excess. This later measurement helps to reduce the correlation between the ^{8}He mass and the ^{8}C mass that results when using the $^{12}C(^{4}He,^{8}He)^{8}C$ reaction.

Table 4-4 contains the mass excesses for the A=8 isobaric quintet. The 1981 mass tables (Wa81) have been used to derive these masses. Because of the large number of connections between the ground state masses in this region, it was felt that a local adjustment was not necessary. The measurements of the T=2 states were, however, analyzed with this table.

Table 4-4 also contains the coefficients from a fit using the IMME. With the change in the ^{8}Li mass from its previous value, the deviation from the quadratic form of the IMME has been eliminated. This holds even when the new and old ^{8}Li masses are averaged together. Figure 4-3 shows the residuals of the quadratic fit to the A=8 quintet.

It is striking that even in this case, where several members of the quintet (^{8}C, ^{8}B and ^{8}Be) are unbound to isospin allowed particle decay, that agreement with the quadratic form of the IMME is still maintained.

4.3 Quintet Summary

Besides the A=8 and 24 isobaric quintets, the A=20, 32, and 36 quintets have been completed. Of the remaining A=4n systems for $A \leq 44$ there are four multiplets A=12, 16, 28,

Table 4-4 Summary of the properties of the A=8 isobaric quintet and coefficients of the IMME fits.

Nuclide	T_z	Mass Excess (keV)	Excitation (keV)	References
^{8}C	-2	35095(23)	0	(Wa81)[a]
^{8}B	-1	33542.3(79)	10622.1(80)	(Ro75)[b]
^{8}Be	0	32432.0(24)	27490.3(24)	(No76, This work)[c]
^{8}Li	1	31785.9(57)	10840.6(58)	(This work)[d]
^{8}He	2	31598.0(91)	0	(Wa81)

a	b	c	d	e	χ^2_ν
32432.3(23)	-876.7(38)	229.8(25)	-	-	0.2
32432.4(23)	-878.1(64)	229.4(28)	0.6(23)	-	0.3
32432.0(24)	-876.7(38)	232.3(70)	-	-0.7(18)	0.3
32432.0(24)	-879.5(68)	233.3(72)	1.3(26)	-1.2(20)	-

a
Based on a weighted average of (Tr76,Ro76).

b
Used measured Q value ratio from (Ro75) and 1981 mass tables (Wa81) to obtain these values.

c
Adjusted value from (No76) using (Wa81) then took a weighted average with this work. Quoted error has been scaled according to the prescription of (Ba70).

d
The measurement of (Ro75) has not been included.

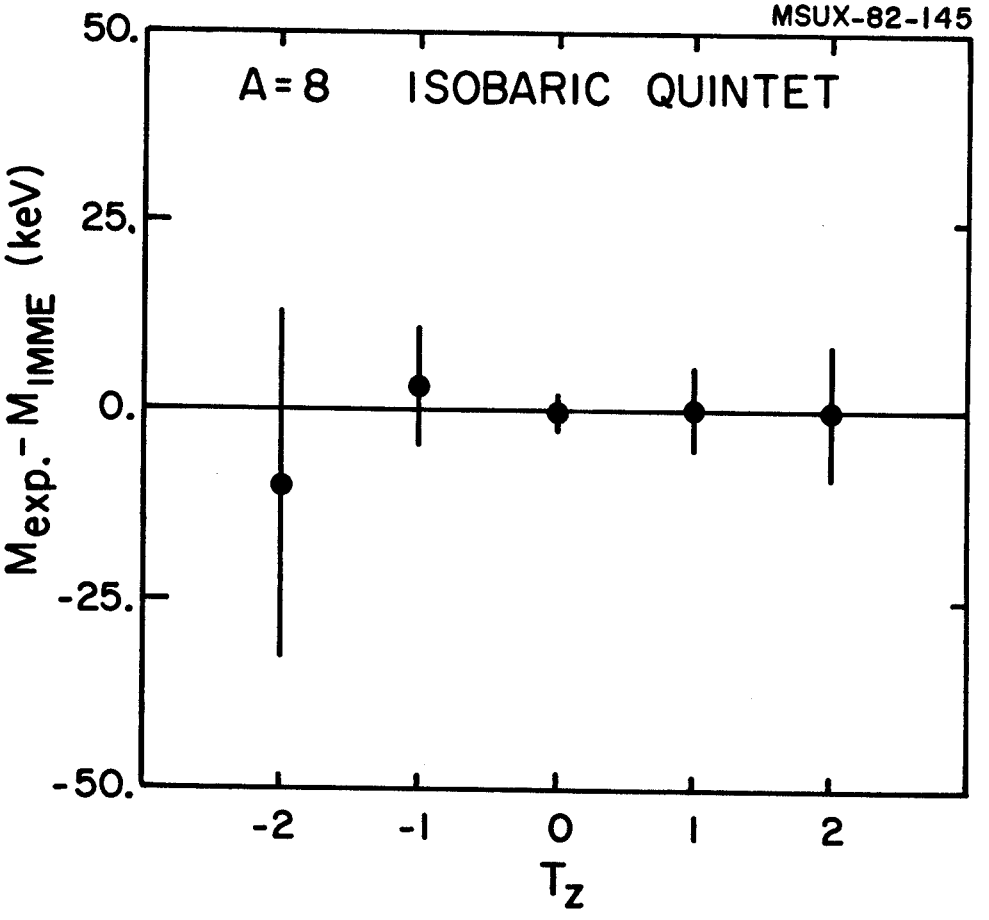

Figure 4-3. Residuals for a quadratic IMME fit to the A=8 quintet.

and 4Ø which contain four known members (A=44 has only three members known). Each of these is missing the T_z=-1 member of the quintet. Experimentally, this has been the most difficult mass to measure, because no good general method has been found to identify the T=2 state in these T_z=-1 nuclei (Be79).

There are at least 9 excited quartets that have been completed (Be79). However, there is as of yet no case of a complete excited quintet. Only for the A=16 multiplet are four members known. For the A=12 and 2Ø multiplets three members are known.

Tables 4-5 through 4-15 contain a summary of these quintets. The uncompleted cases are included and use the quadratic form of the IMME to predict the unknown mass excesses and excitation energies. The residuals of the quadratic fit to the IMME have been plotted for the three completed quintets (2Ø, 32, and 36) and are shown in Figures 4-4 through 4-6.

In all cases the 1981 mass tables (Wa81) were used in the analysis of the data.

Figures 4-7 through 4-1Ø contain plots of the d and e coefficients obtained from IMME fits. For fits with only a d or e coefficient the uncompleted quintets were included. It is worth noting, that for a multiplet where the T_z=-1 mass is missing, the derived d coefficient will equal the e coefficient. For the completed quintets both d and e could be tested simultaneously. These coefficients are shown in

Table 4-5 Summary of the properties of the A=12 isobaric quintet and coefficients of the IMME fits.

Nuclide	T_z	Mass Excess (keV)	Excitation (keV)	References
^{12}O	-2	32066(45)	0	(Ke78, Bu80)[a]
^{12}N	-1	[29589(16)]	[12251(16)]	IMME[b]
^{12}C	0	27595.0(24)	27595.0(24)	(Ro78)
^{12}B	1	26080(19)	12711(19)	(Ne71,As76)[c]
^{12}Be	2	25077(15)	0	(Al78)

a	b	c	d	e	χ^2_ν
27594.9(24)	-1749.6(111)	244.7(59)	-	-	0.2
27595.0(24)	-1763.0(260)	244.1(60)	4.0(69)	-	-
27595.0(24)	-1747.3(119)	228.3(292)	-	4.0(69)	-

a
A weighted average of these two measurements. The value from ref. (Bu80) required a small -3 keV correction (Mo82a).

b
Prediction using the quadratic form of the IMME.

c
A weighted average of these two measurements. This differs from the adopted value of Ex=12750(50) keV in (Aj80) based on (As76) and (Aj75). The latter measurement is $^{9}Be(^{7}Li,\alpha)^{12}B$ which is isospin forbidden to the T=2 level and is therefore unlikely to populate it.

Table 4-6 Summary of the properties of the A=12 first excited (2^+) isobaric quintet and coefficients of the IMME fits.

Nuclide	T_z	Mass Excess (keV)	Excitation (keV)	References
^{12}O	-2	[33810(860)]	[1740(860)]	IMME[a]
^{12}N	-1	[31500(340)]	[14160(340)]	IMME[a]
^{12}C	0	29630(50)	29630(50)	(As76)
^{12}B	1	28189(100)	14820(100)	(As76)
^{12}Be	2	27179(19)	2102(12)	(Al78,Al78a)[b]

a	b	c	d	e	χ^2_ν
29630(50)	-1657(214)	216(104)	-	-	-

[a] Predictions using the quadratic form of the IMME.

[b] A weighted average of these two measurements.

Table 4-7 Summary of the properties of the A=16 isobaric quintet and coefficients of the IMME fits.

Nuclide	T_z	Mass Excess (keV)	Excitation (keV)	References
^{16}Ne	-2	24022(51)	Ø	(Ke78,Bu8Ø)[a]
^{16}F	-1	[20793(17)]	[10113(19)]	IMME[b]
^{16}O	Ø	17983(5)	22720(5)	(Aj82)
^{16}N	1	15609.8(74)	9928(7)	(He68)
^{16}C	2	13694.2(36)	Ø	(Wa81)[c]

a	b	c	d	e	χ^2_ν
17981.3(47)	-2589.4(101)	222.8(49)	-	-	Ø.9
17983.Ø(5Ø)	-2595.3(119)	218.8(65)	3.3(35)	-	-
17983.Ø(5Ø)	-2582.Ø(128)	205.4(19Ø)	-	3.3(35)	-

a
A weighted average of these two measurements. The value from (Bu8Ø) required a -3 keV correction to the Q value (Mo82a).

b
Prediction using the quadratic form of the IMME.

c
This is based on a weighted average of Q values from ref. (Fo77) and (Se78).

Table 4-8 Summary of the properties of the A=16 first excited (2^+) isobaric quintet and coefficients of the IMME fits.

Nuclide	T_z	Mass Excess[a] (keV)	Excitation (keV)	References
^{16}Ne	-2	25712(87)	1690(70)	(Ke78)
^{16}F	-1	[22593(28)]	[11913(29)]	IMME[b]
^{16}O	0	19785(11)	24522(11)	(Al70)
^{16}N	1	17382.8(74)	11701(7)	(He68)[c]
^{16}C	2	15460(11)	1766(10)	(Fo77)

a	b	c	d	e	χ^2_ν
19771.1(94)	-2600.9(156)	220.9(75)	-	-	6.0
19785.0(110)	-2615.6(167)	200.3(113)	13.2(54)	-	-
19785.0(110)	-2563.0(219)	147.7(308)	-	13.2(54)	-

a The ground state masses used are tabulated in Table 4-7.

b Prediction using the quadratic form of the IMME.

c This could be a 1^- or 2^+ level.

Table 4-9 Summary of the properties of the A=20 isobaric quintet and coefficients of the IMME fits.

Nuclide	T_z	Mass Excess (keV)	Excitation (keV)	References
^{20}Mg	-2	1757(27)	0	(Wa81)[a]
^{20}Na	-1	13420(50)	6580(50)[b]	(Mo79)
^{20}Ne	0	9689.4(23)	16735.7(31)	(Bl67,Ku67,Ad69)[c]
^{20}F	1	6502.4(31)	6519.4(30)	(Mi76)
^{20}O	2	3799.5(84)	0	(Wa81)[d]

a	b	c	d	e	χ^2_ν
9690.4(22)	-3437.6(49)	247.5(32)	-	-	1.1
9689.5(23)	-3434.4(56)	249.4(36)	-2.3(19)	-	0.8
9689.4(23)	-3444.0(68)	259.7(95)	-	-2.6(19)	0.4
9689.4(23)	-3464.1(335)	279.4(335)	5.3(87)	-7.6(85)	-

a Based on a measurement by ref. (Tr76a).

b This value based on the mass difference between the T=2 and ground state (Wa81) mass excesses. This differs from the value of Ex=6570(50) keV from ref. (Mo79).

c Weighted average of these three measurements.

d Based on weighted average of Q value from (Ja60,Hi62).

Table 4-1Ø Summary of the properties of the A=2Ø first excited (2^+) isobaric quintet and coefficients of the IMME fits.

Nuclide	T_z	Mass Excess (keV)	Excitation (keV)	References
^{2Ø}Mg	-2	[2Ø46Ø(8ØØ)]	[29ØØ(8ØØ)]	IMME[a]
^{2Ø}Na	-1	[1553Ø(3ØØ)]	[869Ø(3ØØ)]	IMME[a]
^{2Ø}Ne	Ø	11383.8(29)	1843Ø.1(35)	(Ad68,Ku72)[b]
^{2Ø}F	1	8Ø33(1ØØ)	8Ø5Ø(1ØØ)	(Aj78)[c]
^{2Ø}O	2	5473.2(84)	1673.68(15)	(Wa73)

a	b	c	d	e	χ^2_ν
11383.8(29)	-3746(2ØØ)	396(1ØØ)	-	-	-

a Prediction from the quadratic form of the IMME.

b Weighted average of these two measurements.

c From a measurement in ref. (Ce64).

Table 4-11 Summary of the properties of the A=28 isobaric quintet and coefficients of the IMME fits.

Nuclide	T_z	Mass Excess (keV)	Excitation (keV)	References
^{28}S	-2	-4134(160)	Ø	(Mo82)
^{28}P	-1	[-1252.8(98)]	[5908(11)]	IMME[a]
^{28}Si	Ø	-6269.3(31)	15223(3)	(Sn69,Je72)[b]
^{28}Al	1	-10858.1(8)	5992.4(4)	(St73)
^{28}Mg	2	-15018.7(21)	Ø	(Wa81)

a	b	c	d	e	χ^2_ν
-6269.4(31)	-4802.7(50)	214.0(20)	-	-	Ø.1
-6269.3(31)	-4798.Ø(137)	206.7(200)	2.5(67)	-	-
-6269.3(31)	-4788.2(400)	196.9(468)	-	2.5(67)	-

a Prediction using quadratic form of the IMME.

b Updated the value from (Sn69) brought it into agreement with (Je72). This excitation energy differs from that of (En78) Ex=15225(3) keV.

Table 4-12 Summary of the properties of the A=32 isobaric quintet and coefficients of the IMME fits.

Nuclide	T_z	Mass Excess (keV)	Excitation (keV)	References
^{32}Ar	-2	-2176(50)	0	(Bu80,Mo82)[a]
^{32}Cl	-1	-8296.4(54)	5033.1(93)	(Ha77)
^{32}S	0	-13971.1(5)	12045.0(4)	(An80)
^{32}P	1	-19232.6(11)	5073.2(9)	(Pi60,Ly67,Va67,Fo72)[b]
^{32}Si	2	-24079.1(12)	0	(Wa81)

a	b	c	d	e	χ^2_ν
13971.1(5)	-5468.8(19)	207.4(11)	-	-	0.2
13971.1(5)	-5468.8(21)	207.3(26)	0.0(10)	-	0.4
13971.1(5)	-5468.5(27)	206.8(33)	-	0.1(5)	0.4
13971.1(5)	-5465.5(56)	205.2(43)	-2.6(43)	1.4(23)	-

a Based on Q value for ^{32}S(π^+,π^-)^{32}Ar = -23840(50) keV.

b Weighted average of these four measurements.

Table 4-13 Summary of the properties of the A=36 isobaric quintet and coefficients of the IMME fits.

Nuclide	T_z	Mass Excess (keV)	Excitation (keV)	References
^{36}Ca	-2	-6440(40)	Ø	(Wa81)[a]
^{36}K	-1	-13168(22)	4258(23)	(Ay81a)
^{36}Ar	Ø	-19379.6(22)	10851.8(22)	(Hu76,Ma76a)[b]
^{36}Cl	1	-25223.2(10)	4298.9(10)	(Ma75,Ri75,Ve76)[c]
^{36}S	2	-30664.51(26)	Ø	(Wa81)

a	b	c	d	e	χ^2_ν
19379.8(20)	-6044.5(34)	201.1(13)	-	-	1.9
19380.2(22)	-6045.3(38)	203.1(46)	-0.8(17)	-	3.5
19379.6(22)	-6043.2(74)	199.3(91)	-	0.3(14)	3.7
19379.6(22)	-6018.1(151)	176.4(150)	-9.5(50)	7.6(41)	-

a Based on Q value from (Tr77).

b A weighted average of these measurements; uncertainty scaled according to (Ba70). This excitation energy differs from that of (En78) where Ex=10853.4(15) keV.

c Result is a weighted average of these three measurements. In ref. (En78) the value adopted was from ref. (Ve76) where Ex=4299.5(11) keV.

Table 4-14 Summary of the properties of the A=40 isobaric quintet and coefficients of the IMME fits.

Nuclide	T_z	Mass Excess (keV)	Excitation (keV)	References
^{40}Ti	-2	-8792(160)[a]	0	(Mo82)
^{40}Sc	-1	[-16164(39)][b]	[4364(39)][b]	IMME[c]
^{40}Ca	0	-22874(15)	11974(15)	(Ce68,Ha70,Ad72,Bo77)[d]
^{40}K	1	-29151.9(12)	4384.0(3)	(St77)
^{40}Ar	2	-35040.8(14)	0	(Wa81)

a	b	c	d	e	χ^2_ν
22859.7(131)	-6494.2(197)	201.8(66)	-	-	3.8
22874.0(150)	-6502.3(201)	239.4(203)	-15.0(77)	-	-
22874.0(150)	-6562.2(400)	299.3(503)	-	-15.0(77)	-
22874.0(150)[e]	-6472.4(226)[e]	194.5(76)[e]	-	-	-

a
This mass is predicted to be -9151(91) keV from the quadratic IMME (using Ca,K and Ar).

b
This mass is predicted to be -16207(45) keV with Ex=4321(45) from the quadratic IMME (using Ca,K, and Ar).

c
Prediction from the quadratic IMME, with Ti in the fit.

d
Weighted average of these four measurements.

e
Coefficients from the IMME fit, did not include Ti.

Table 4-15 Summary of the properties of the A=44 isobaric quintet and coefficients of the IMME fits.

Nuclide	T_z	Mass Excess (keV)	Excitation (keV)	References
^{44}Cr	-2	[-13461(36)]	Ø	IMME[a]
^{44}V	-1	[-21Ø23(14)]	[283Ø(1ØØØ)]	IMME[a]
^{44}Ti	Ø	-28211.8(25)	9338(2)	(Si72)[b]
^{44}Sc	1	-35Ø27.3(4Ø)	2787.4(27)	(En78)[c]
^{44}Ca	2	-41469.4(16)	Ø	(Wa81)

a	b	c	d	e	χ^2_ν
28211.8(25)	-7ØØ2.2(89)	186.7(43)	-	-	-

a Prediction using the quadratic form of the IMME.

b A possible doublet with a companion level at Ex=9298(2) keV (Di78).

c A weighted average of seven measurements tabluated in ref. (En78), the adopted value in this ref. was Ex=2787(3) keV.

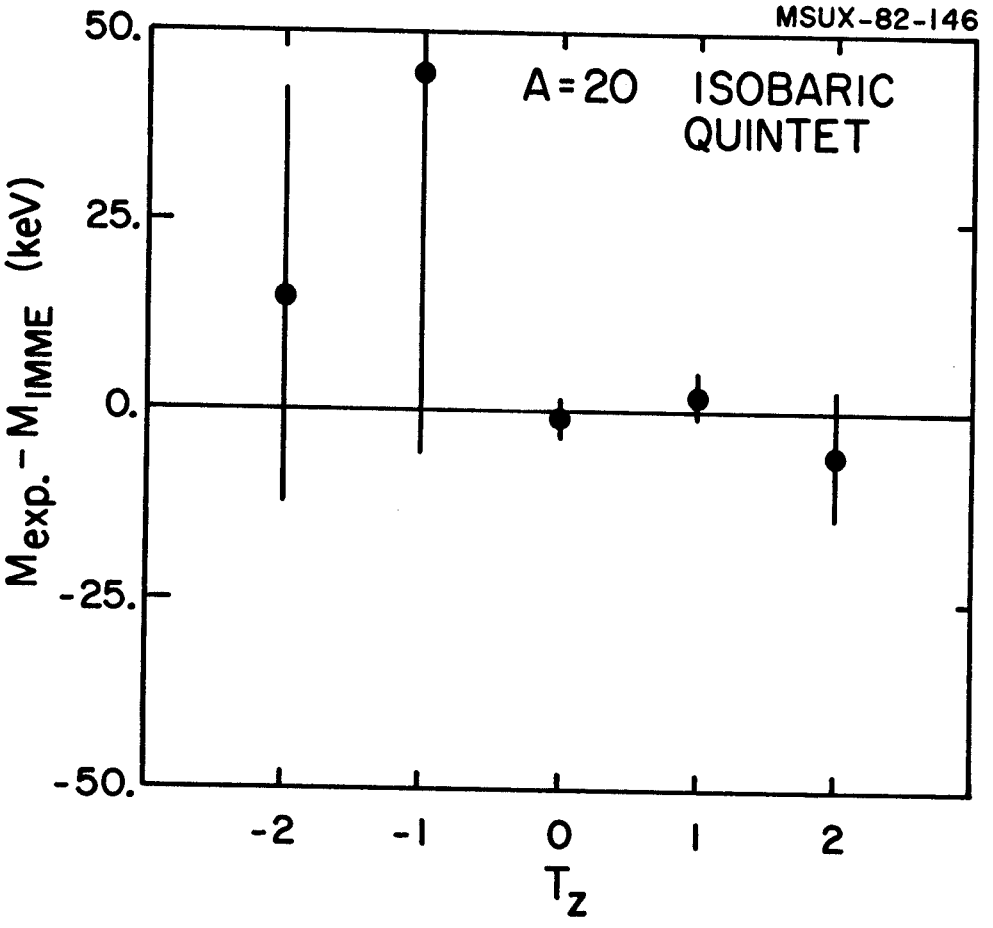

Figure 4-4. Residuals for a quadratic IMME fit to the A=20 quintet.

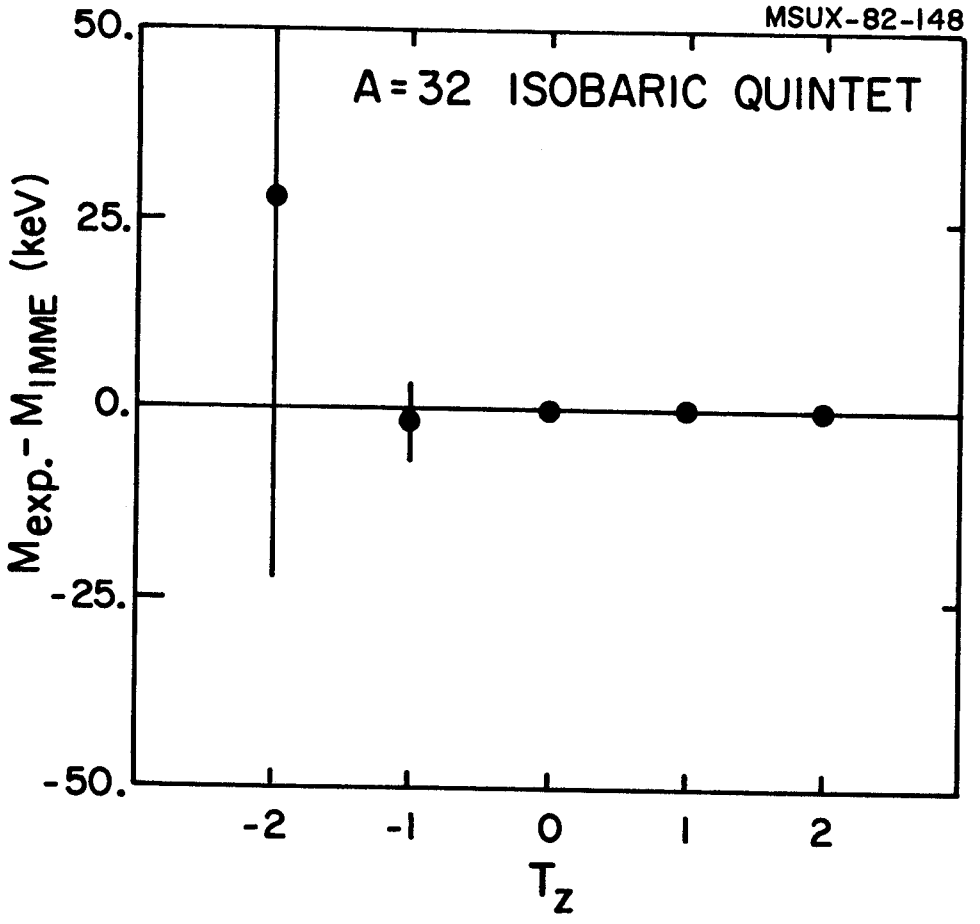

Figure 4-5. Residuals for a quadratic IMME fit to the A=32 quintet.

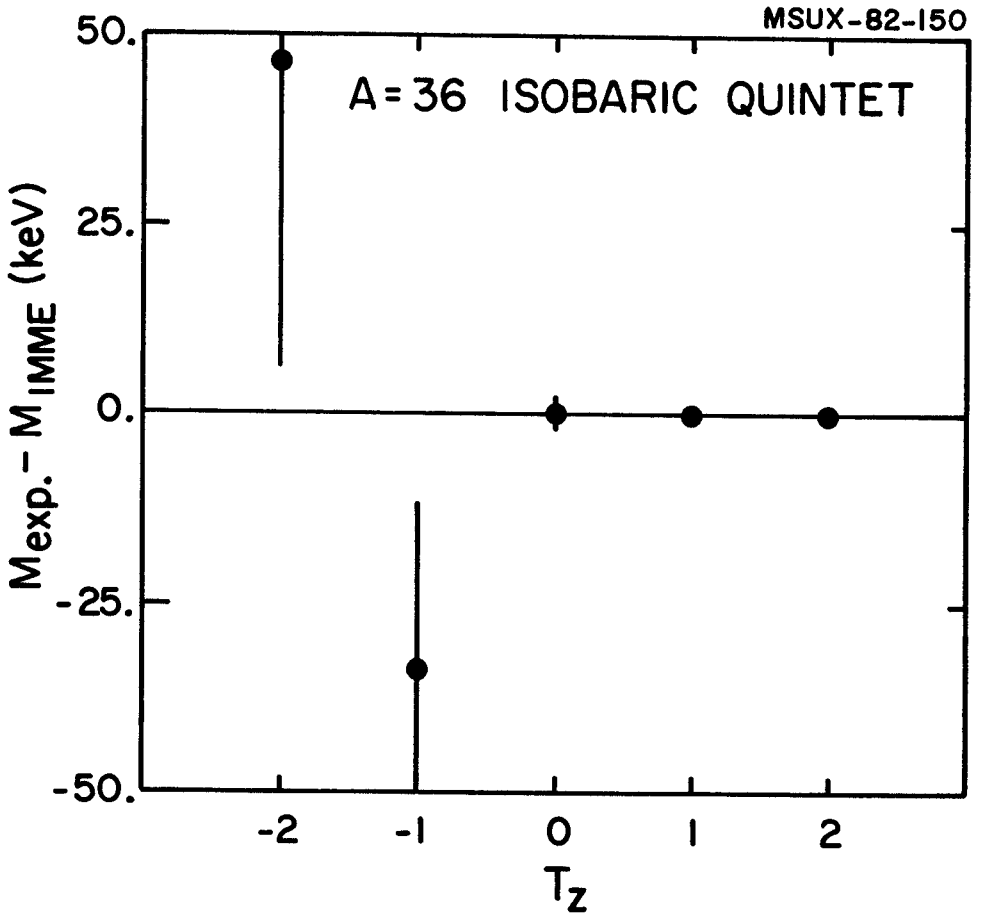

Figure 4-6. Residuals for a quadratic IMME fit to the A=36 quintet.

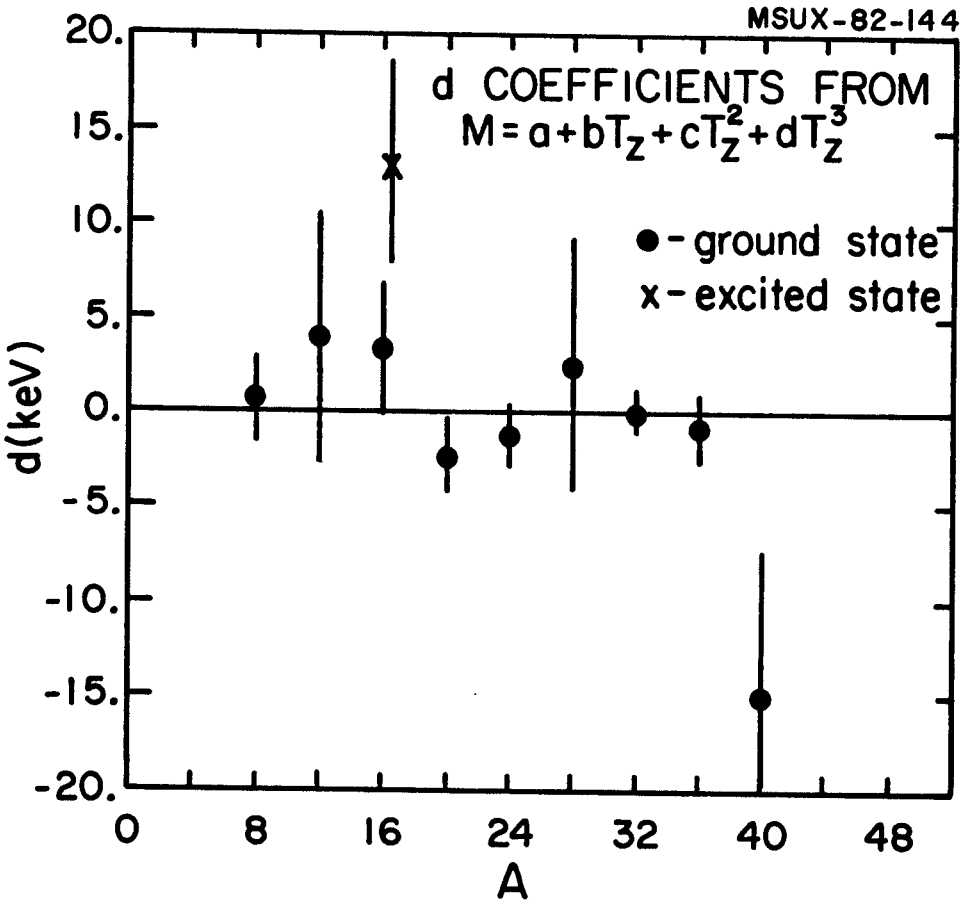

Figure 4-7. The d coefficient of the IMME with e=0 plotted versus mass number of the quintet.

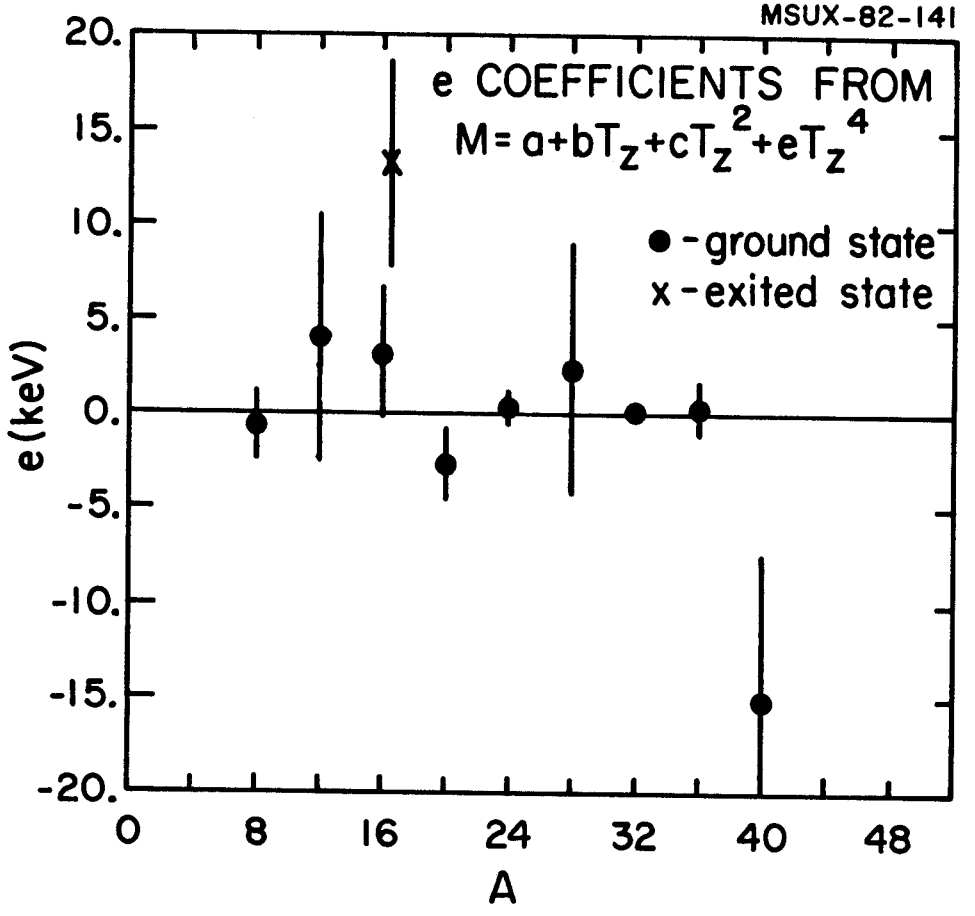

Figure 4-8. The e coefficient of the IMME with d=0 plotted versus mass number of the quintet.

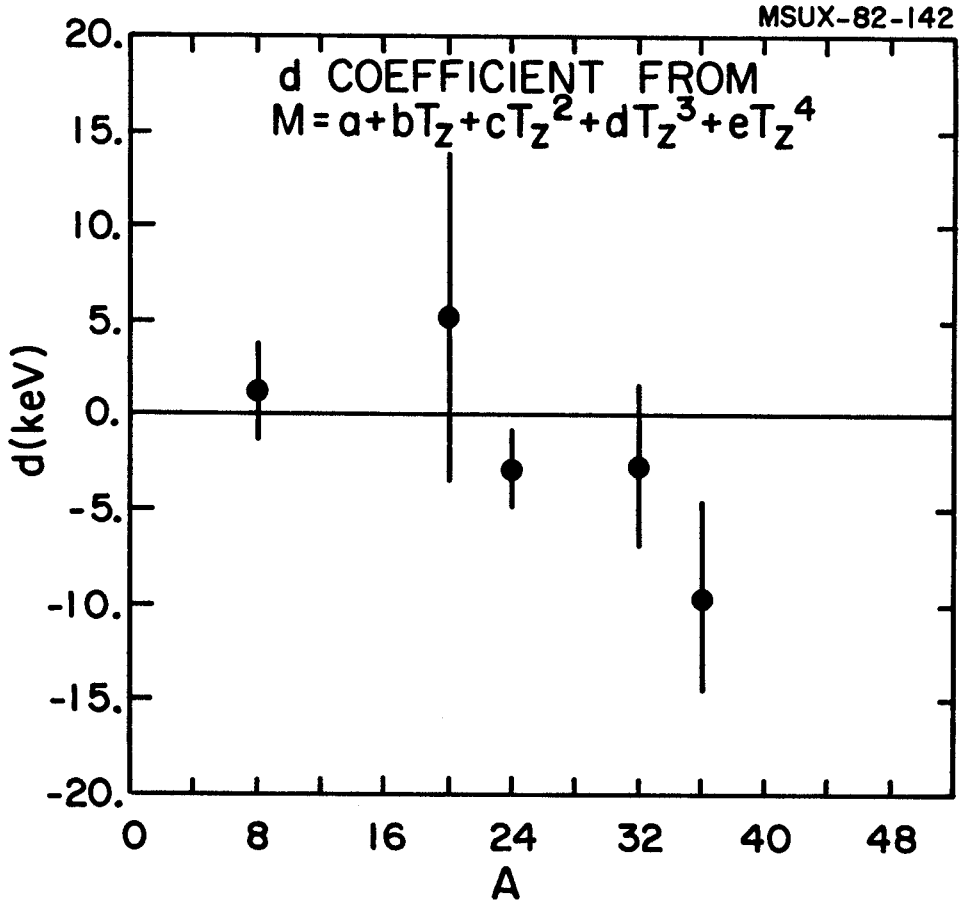

Figure 4-9. The d coefficient of the quartic IMME ($e \neq 0$) plotted versus mass number of the quintet.

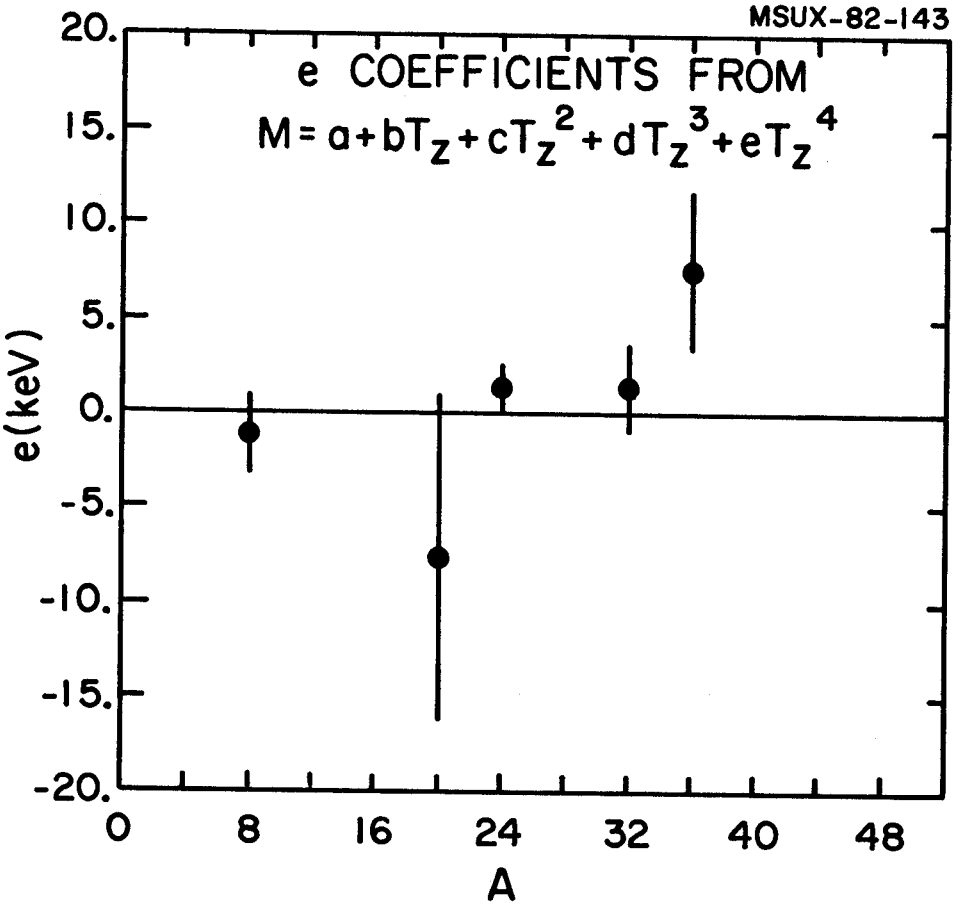

Figure 4-10. The e coefficient of the quartic IMME ($d \neq 0$) plotted versus mass number of the quintet.

the latter two figures (4-9 and 4-10).

It is apparent that for fits using either a d or e coefficient there is quite good agreement with the quadratic form of the IMME. Only in the excited A=16 and the ground state A=40 multiplet are there significant deviations from the quadratic IMME. Neither of these multiplets is completed and in particular the measurement of the ^{40}Ti mass excess is still preliminary (Mo82).

For the completed quintets there is a larger spread in the coefficients when both d and e are used simultaneously, but only in the A=36 case are the two coefficients inconsistent with zero. However, because the reduced chi-squared for the quadratic fit was significantly smaller than that for a fit using either a d or e coefficient, there is no real need for these coefficients. Also, the residuals for the quadratic fit in this case reveal that both the T_z = -1 and -2 masses are poorly determined relative to the other members of the multiplet, which may account for the apparent deviation.

4.4 The b and c coefficients

Examination of the experimentally-determined mass excesses shows that in most cases the quadratic form of the IMME is satisfied. Figure 4-11 shows the b and c coefficients of the quadratic IMME plotted versus mass number (A) of the quintet. The trend of a decreasing positive c coefficient and an increasing negative b

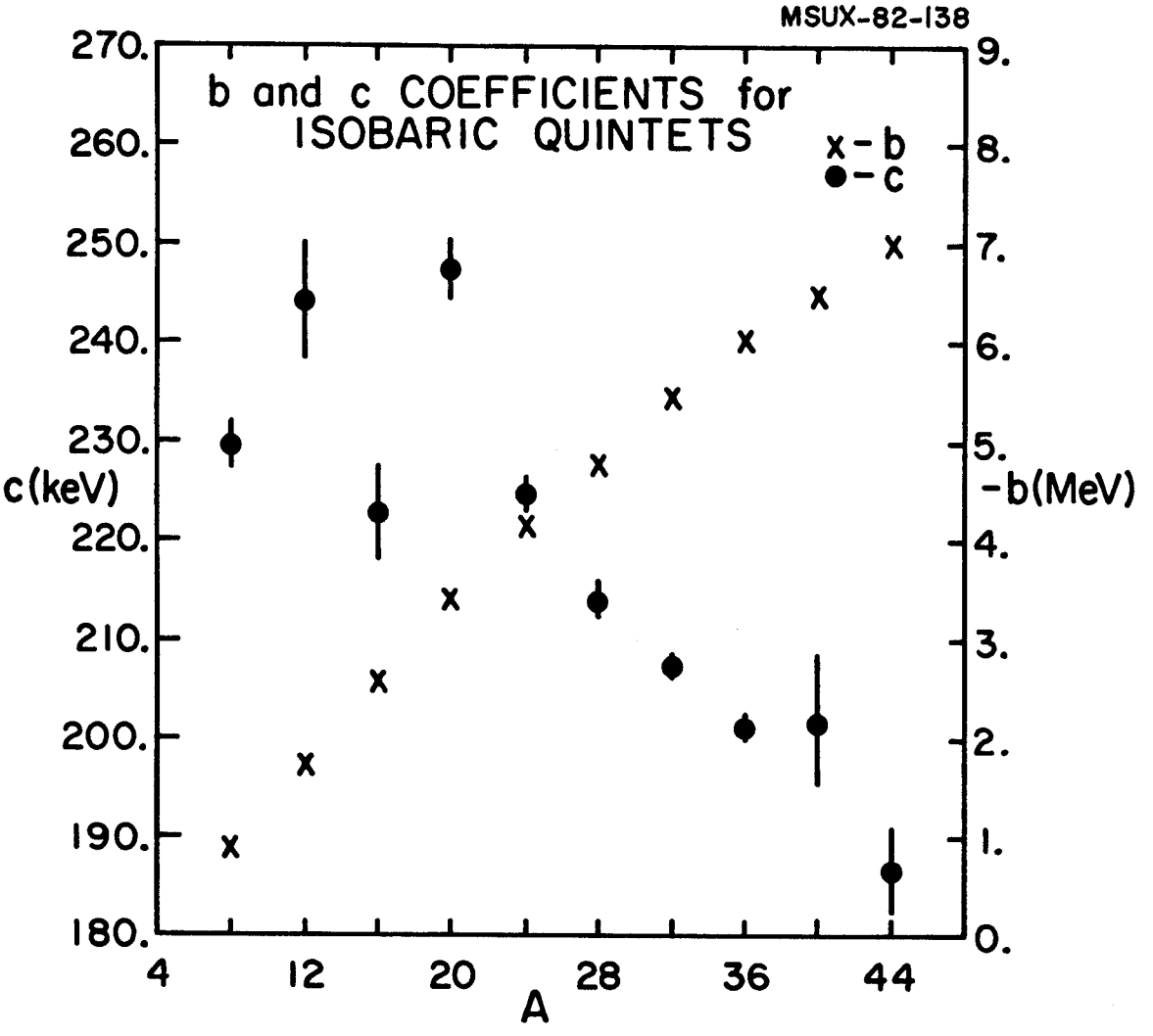

Figure 4-11. The b and c coefficients of the quadratic IMME for isobaric quintets plotted versus mass number of the quintet.

coefficient is the same as that observed in isobaric quartets (Be79).

A simple model which explains the approximate size of the b and c coefficients may be used to compare these coefficients.

Considering the nucleus to be a uniformly-charged sphere of radius R_c, the total Coulomb energy is

$$E^{(1)}(\alpha_0,T) = \left\langle \alpha_0 T T_z \left| H_C \right| \alpha_0 T T_z \right\rangle = \frac{3}{5}\frac{Z(Z-1)e^2}{R_c} \qquad (4\text{-}1)$$

Expressing the proton number Z as $A/2-T_z$ (from $T_z=(N-Z)/2$ and $A=N+Z$), this expression becomes

$$E^{(1)}(\alpha_0,T) = \frac{0.6e^2}{R_c}\left[\frac{A^2}{4} - (A-1)T_z + T_z^2\right] \qquad (4\text{-}2)$$

Comparing this quadratic equation in T_z to the quadratic IMME the coefficients b and c may be expressed as

$$b = \frac{-0.6e^2}{R_c}(A-1) + (M_n - M_p) \qquad (4\text{-}3)$$

and

$$c = \frac{0.6e^2}{R_c} \qquad (4\text{-}4)$$

where the neutron-proton mass difference has been added to the b coefficient (used $M_n-M_{^1H}$ in the calculations). Defining the quantity b* as

$$b^* = b - (M_n - M_p) \qquad (4\text{-}5)$$

an expression for the relation between b* and c is

$$R \equiv \frac{b^*}{c(1-A)} = 1 \qquad (4\text{-}6)$$

where the quantity R is by definition 1 for a uniform sphere. Figure 4-12 shows the quantity R plotted versus mass number (A) of the quintet. Deviations are apparent, but the agreement is quite good for such a simple model.

The Coulomb radius parameter can also be extracted from this model by setting R_c in Equations 4-3 and 4-4 equal to $r_o A^{1/3}$. Solving for r_o in each equation the Coulomb radius parameters are

$$r_{ob} = \frac{0.6e^2(1 - A)}{b^* A^{1/3}} \qquad (4\text{-}7)$$

and

$$r_{oc} = \frac{0.6e^2}{c A^{1/3}} \qquad (4\text{-}8)$$

For a uniformly-charged sphere the r_o extracted from the b and c coefficients should be equal. Figure 4-13 shows the Coulomb radii r_o determined from the b and c coefficients of the quadratic IMME plotted versus mass number (A) of the quintet. There is quite good agreement between the value of r_o as calculated from the two different coefficients, much better in fact than for quartets, where the r_o derived from the c coefficient shows more fluctuations (Be79).

For a given multiplet there are two Coulomb energy effects that occur when moving from the neutron-rich to the proton-rich member (Be79). There is the increase in energy from the Coulomb interaction between the valence proton and the core. Then there also is the increased energy from the Coulomb interaction between the valence protons themselves.

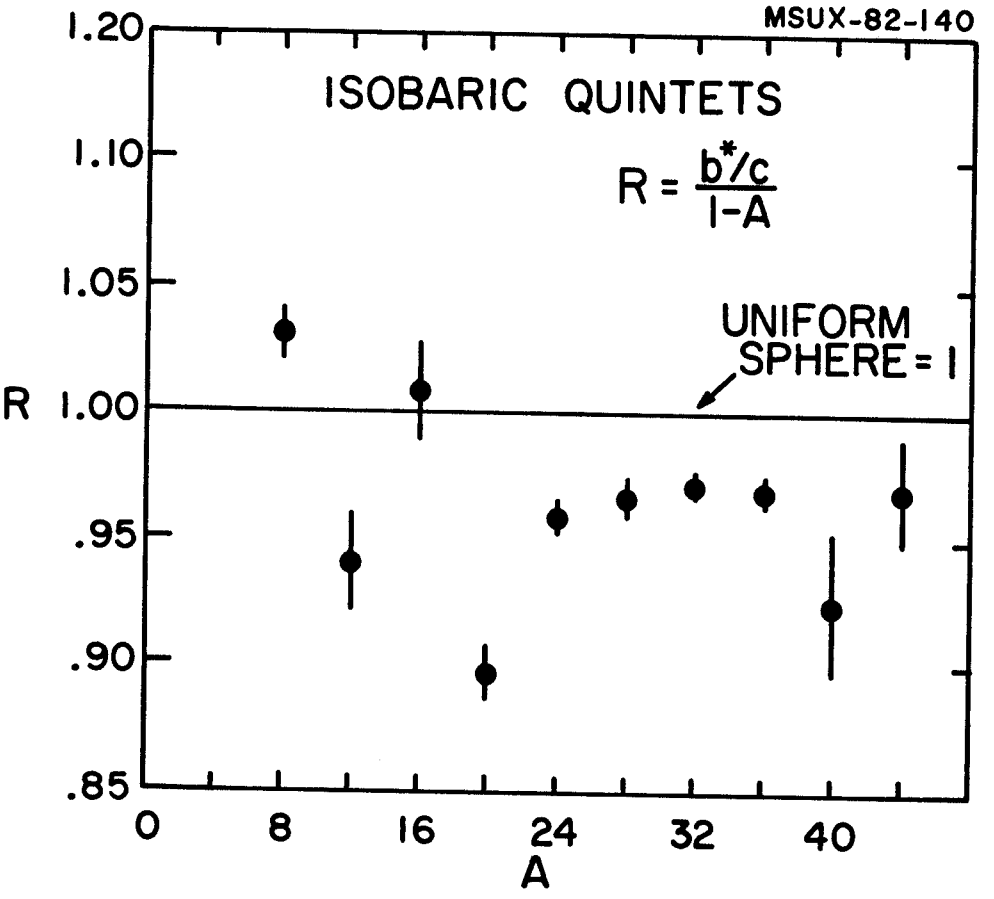

Figure 4-12. The quantity R plotted versus mass number of the quintet. For a uniform sphere, R=1.

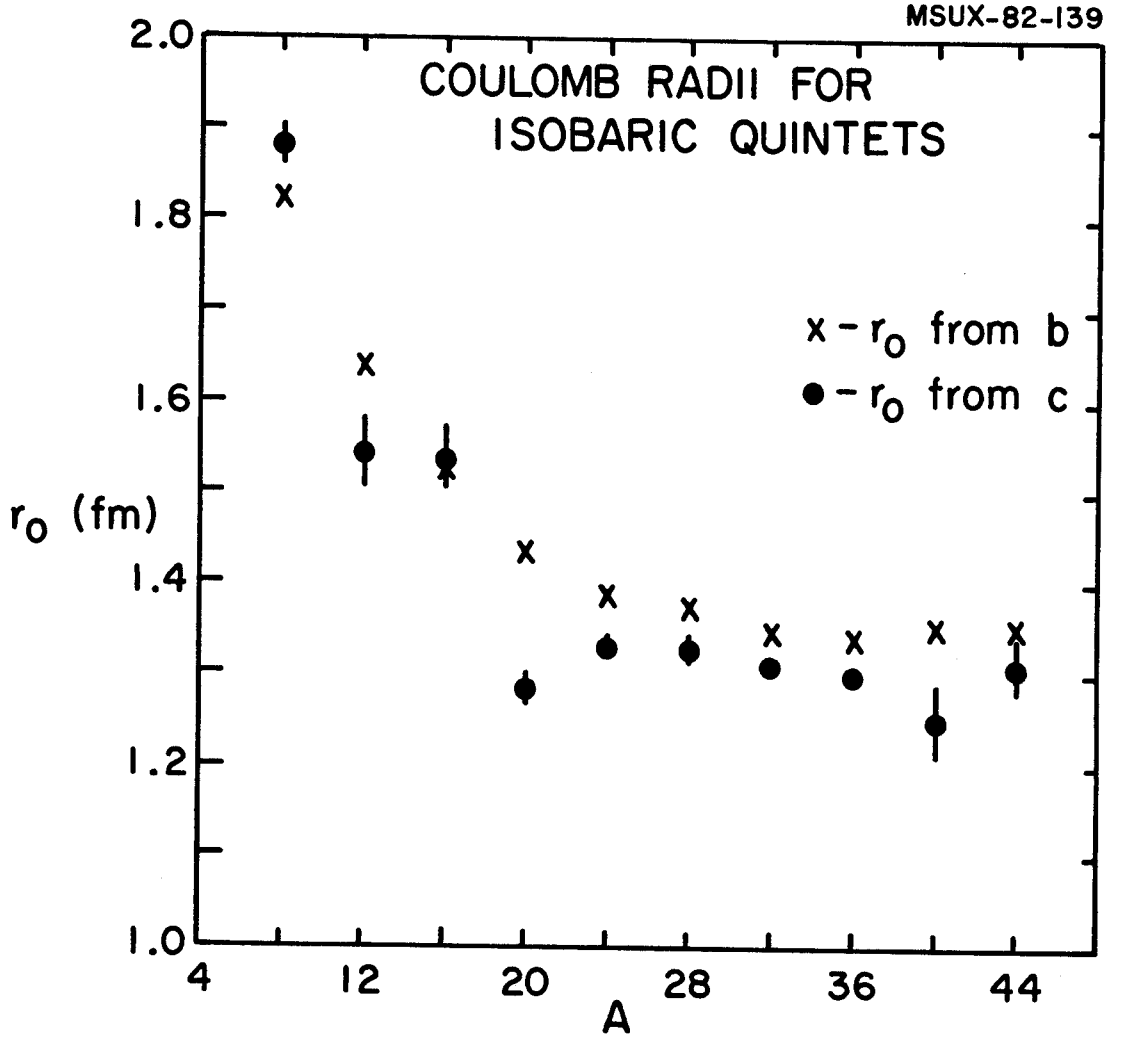

Figure 4-13. Coulomb radii determined from the b and c coefficients of the quadratic IMME plotted versus mass number of the quintet.

The first effect is constant for each proton added so it is expressed in the linear b coefficient. The second effect increases as each proton is added so this dependence is found in the nonlinear c coefficient. Hence, the b coefficient is an average over the core whereas the c coefficient is more sensitive to the wave functions of the valence particles.

In the case of quartets where A=4n±1, the number of protons alternates from even to odd for a given T_z member in one multiplet to the same T_z member in the next multiplet. Because of the strong pairing correlation between nucleons, there is more of an energy difference when a paired proton is converted to a neutron than when an unpaired one is. This additional pairing effect would more likely manifest itself in the b coefficient which displays more of the average properties of the nucleus. In quintets where A is always even, the proton number does not alternate from one T_z member in one multiplet to the same T_z member of the next multiplet. So this pairing effect is greatly reduced.

It is interesting to note the rather large Coulomb radius parameter for the A=8 quintet (see Figure 4-13). The neighboring nuclei ^{7}Li and ^{9}Be have ground state root-mean-square (rms) Coulomb radii inferred from electron scattering of 2.39(3) fm and 2.5Ø(9) fm respectively (Ja74). Taking the radius parameter derived from b (r =1.82 fm), the rms Coulomb radius obtained for the T=2 states is 2.81 fm. This is comparable to the rms Coulomb radius of ^{18}O and ^{19}F.

It is apparent that the T=2 states are significantly larger than the ground states of the neighboring nuclei in this region.

4.5 Conclusions

In the case of the A=24 quintet application of a novel experimental method was successfully applied to yield a precise value for the mass of ^{24}Al as well as the first direct measurement of the half-life of ^{24}Si. For the A=8 quintet the remeasurement of the mass excesses of ^{8}Be and ^{8}Li removed the deviation from the quadratic IMME that existed previous to these measurements.

From an examination of all these A=4n quintets, it is found that agreement with the quadratic form of the isobaric multiplet mass equation is quite good. There seems to be no evidence for substantial higher-order charge-dependent effects in the nuclear interaction, though these effects may be mostly manifested in the c coefficient as is the case for isospin-mixing, Coulomb repulsion and second-order perturbation effects.

It may be conjectured that cases of disagreement from the quadratic form of the isobaric multiplet mass equation may be attributed to experimental error. This leaves only the case of the A=9 ground state quartet where a known deviation is present and where sources of significant experimental error have probably been eliminated.

The significance of the b and c coefficients has been

examined and it is found that they can provide detailed structure information of the analog states.

Further experimental study of both isobaric quartets and quintets is recommended. Mass measurements that complete the remaining quintets as well as improve the accuracy in the known members can, in conjuction with theoretical calculations, provide useful nuclear structure information.

APPENDIX A

A.1 Proton and alpha recoil masses.

The formula for the recoil mass (M_{rec}) can be derived simply from the conservation of momentum in a two-body decay. Following the β-decay of the (A,Z) parent activities to particle unbound levels in the (A,Z-1) nuclei, particle emission populates states in the residual recoil nuclei (A-1,Z-2 for proton emission and A-4,Z-3 for alpha emission). For now we neglect the β-induced recoil, since this just mostly broadens the distribution, ultimately limiting the mass resolution, and does not cause a significant change in the centroid (this effect will examined in Section A.3).

For a two-body decay at rest we have

$$m_p v_p = M_{rec} V_{rec} \qquad \text{(A-1)}$$

where the subscript p denotes the emitted particles (proton or alphas), m, mass and v, velocity. The rec subscript is for the recoiling nucleus. In our case, we have ^{23}Mg recoiling from the delayed proton emission from the T=2 state in ^{24}Al.

Non-relativistically, the energy of the proton is

$$E_p = \frac{1}{2} m_p v_p^2 \qquad \text{(A-2)}$$

solving for the momentum of the proton

$$m_p v_p = \sqrt{2E_p m_p} \qquad \text{(A-3)}$$

Substituting this into the conservation of momentum equation we find

$$M_{rec} = \frac{\sqrt{2E_p m_p}}{V_{rec}} \qquad \text{(A-4)}$$

The velocity of the recoil from the flight path d and the time of flight t is simply

$$V_{rec} = \frac{d}{t} \qquad \text{(A-5)}$$

Replacing this in the recoil mass equation leads to the desired result:

$$M_{rec} = \frac{\sqrt{2E_p m_p}\ t}{d} \qquad \text{(A-6)}$$

For β-delayed alpha emitters expression for the recoil mass is

$$M^{\alpha}_{rec} = \frac{\sqrt{2E_\alpha m_\alpha}\ t}{d} \qquad \text{(A-7)}$$

If, however, the proton mass is used in this equation we obtain

$$M_{rec} = \frac{\sqrt{2E_\alpha m_p}\ t}{d} = \frac{\sqrt{2E_\alpha m_\alpha}\ t}{2d} = \frac{M^{\alpha}_{rec}}{2} \qquad \text{(A-8)}$$

Because we will be using m_p in our calculations rather than m_α, the alpha emitters will appear at one half of their actual mass.

A.2 Beta-decay broadening of the recoil mass distribution.

Neglecting β-recoil, we have been able to obtain a simple relation for the recoil mass M_{rec} (following particle decay) in terms of the experimentally-observable quantities E_p and t.

Assuming M_{rec} is known, we can instead find the recoil's velocity and hence its time of flight. For ^{25}Si decaying to the T=3/2 state in ^{25}Al followed by ground-state proton emission we have a ^{24}Mg recoil with a velocity of V_{rec} = .12 cm/ns and a time of flight of 68 ns for our 8 cm flight path. This is in contrast to the proton velocity of v_p = 2.8 cm/ns.

We now consider the approximate effect of β-recoil on our mass resolution. For the β-decay of ^{25}Si we have both β^+ and ν emission. Since we are not detecting either of these particles, it is tempting to believe that the recoil effects may just average out. However, as mentioned in the text, the rejection of β^+ - p coincidences in the Si detector and β^+ - p angular correlations complicate the problem. Also, in any beta decay we have the sharing of energy between the β^+ and the ν as well as the angular correlation between their decay. Figure A-1 shows recoil energy distributions between a Fermi type and Gamow-Teller type decay (Di8Ø,Jo63). For the Fermi decay, the β-ν correlation is peaked at small relative angles. We can estimate an upper limit to the size of the effect by assuming that the β^+ and ν are collinear, and then,

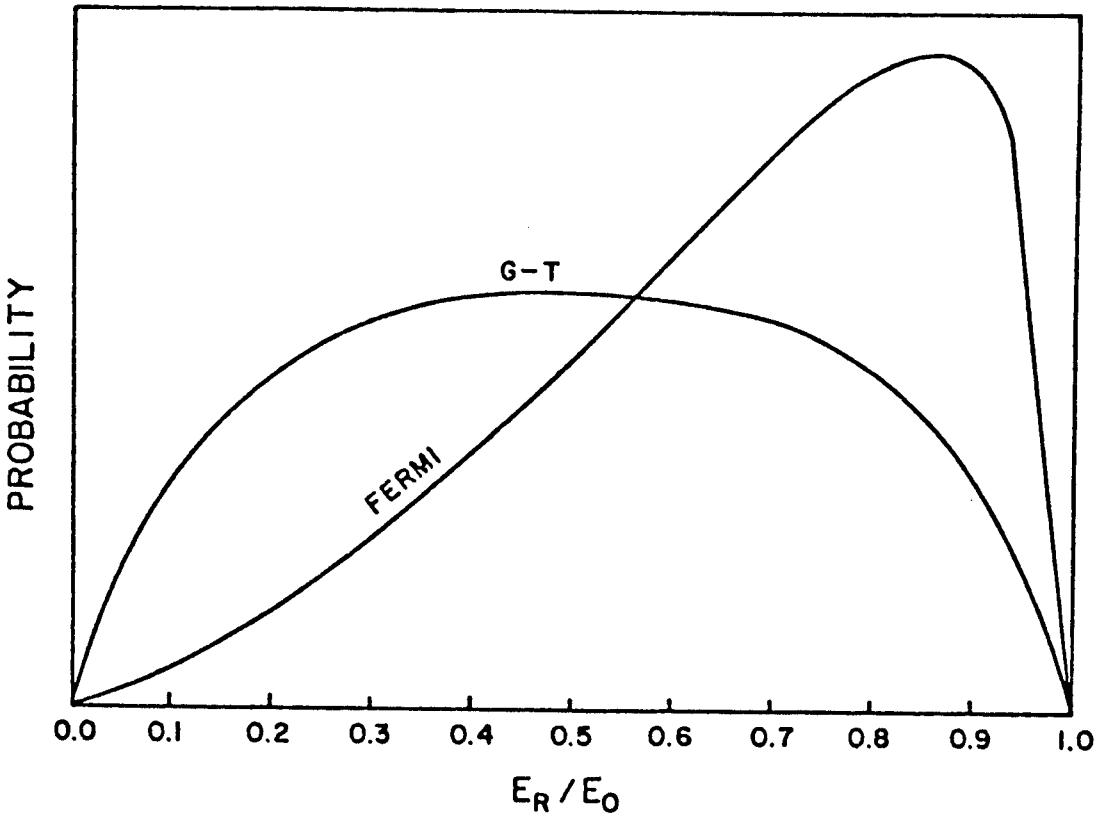

Figure A-1. Fermi and Gamow-Teller recoil energy distributions.

furthermore, giving all the energy to the β^+. As before, we again have a two-body decay, and using momentum conservation can obtain an expression for the initial recoil velocity V_i which occurs before proton emission:

$$p_e = M_i V_i \qquad \text{(A-9)}$$

M_i is the mass of nucleus before proton emission, and is related to the final recoil mass M_{rec} (after proton emission) by

$$M_i \cong M_{rec} + 1 \qquad \text{(A-10)}$$

From the known Q-value of this decay, (to the first T=3/2 level in ^{25}Al) the β^+ kinetic energy is T=4325 keV. This positron is relativistic so we use

$$E_\beta^2 = p_e^2 c^2 + m_e^2 c^4 \qquad \text{(A-11)}$$

and from conservation of momentum we have for the initial recoil velocity

$$V_i = \frac{\sqrt{E_\beta^2 - m_e^2 c^4}}{M_i c^2} c = 6 \times 10^{-3} \text{ cm/ns} \qquad \text{(A-12)}$$

Because this velocity is so much less than the proton velocity (v_p = 2.8 cm/ns), we will neglect any β^+ - p correlation effects in this discussion of the mass resolution. We will consider these effects in relation to changes in the proton centroid in Section A.3.

In comparison to the final recoil velocity (V_{rec} = .12 cm/ns) the initial recoil is more significant for this discussion. Defining the direction toward the center of the Si detector as Ø°, we write the new velocity of the recoil M_{rec} as

$$V'_{rec} = V_{rec} + V_i \cos\theta \qquad \text{(A-13)}$$

where θ is the angle that the beta-decay makes with the axis.

We make a simple velocity addition because the recoils are nonrelativistic. From this expression we see that, for β-decays toward the Si detector, the M_i recoils in the direction of the channel plates with a velocity V_i. Upon the subsequent proton decay, the recoil will have this additional velocity. If, however, the beta is emitted toward the channel plates, then following proton emission, the M_{rec} will have less velocity. Figure 2-18 illustrates this effect.

Still neglecting any proton velocity shift, we can express momentum conservation in terms of an angle dependent recoil mass

$$m_p v_p = M_r(\theta)(V_{rec} + V_i \cos\theta) \qquad \text{(A-14)}$$

We use the Equation A-3 to obtain

$$M_r(\theta) = \frac{\sqrt{2E_p m_p}}{V_{rec}\left(1 + \frac{V_i \cos(\theta)}{V_{rec}}\right)} \qquad \text{(A-15)}$$

and making use of the expression for M_{rec} from Equation A-4.

$$M_r(\theta) = \frac{M_{rec}}{\left(1 + \frac{V_i \cos(\theta)}{V_{rec}}\right)} \qquad \text{(A-16)}$$

This is an expression for the angle-dependent mass $M_r(\theta)$ in terms of the mass M_{rec} and velocity V_{rec} and the initial β-recoil velocity V_i.

The range of allowed angles is only from 19° to 18Ø°. This is because we reject positrons that enter the Si detector as they will be coincident with the protons and hence have too large an energy signal.

If we put into Equation A-16 the above limits on the angle θ, we have a percentage change in the derived mass of 8.8%. A better estimate of our mass resolution is to calculate the variance or root-mean square of the deviations via the expression

$$\sigma_M^2 = \left\langle M_r^2(\theta) \right\rangle - \left\langle M_r(\theta) \right\rangle^2 \qquad \text{(A-17)}$$

where the < > denote an integration over angles. We need to evaluate expressions of the form

$$\left\langle M_r(\theta) \right\rangle = \frac{\int_{\theta_1}^{\theta_2} M_r(\theta)\, 2\pi \sin\theta d\theta}{\int_{\theta_1}^{\theta_2} 2\pi \sin\theta d\theta} \qquad \text{(A-18)}$$

$$\left\langle M_r^2(\theta) \right\rangle = \frac{\int_{\theta_1}^{\theta_2} M_r^2(\theta)\, 2\pi \sin\theta d\theta}{\int_{\theta^2}^{\theta_2} 2\pi \sin\theta d\theta} \qquad \text{(A-19)}$$

Substituting Equation A-16 into the above integrals (θ_1 = 19° and θ_2 = 18Ø°) yields the result for the fractional standard deviation in the recoil mass of

$$\frac{\sigma_M}{M_{rec}} \cong 0.03 \qquad \text{(A-2Ø)}$$

If we treat the distribution as if it were Gaussian, we can obtain an estimate for the full-width at half-maximum (FWHM) for the percentage mass resolution as

$$\text{FWHM} \cong 2.354 \frac{\sigma_M}{M_{rec}} \times 100\% \cong 7\% \qquad \text{(A-21)}$$

This is the "intrinsic" mass resolution limit and has no dependence on the length of the flight path used. A long flight path, however, will reduce the effect of a finite source size which can degrade the mass resolution. Monte Carlo calculations were used in the design of the Princeton apparatus to ensure that this effect was kept smaller than the β-recoil limit (Ro77). We therefore used the same length flight path and source size in our apparatus.

A.3 The effect of beta-recoil on the proton energy.

The recoil mass was a crudely-determined quantity and was used only to filter out nearby masses. In contrast, the proton energy is a precisely-determined quantity and, therefore, scrutiny of any possible systematic effects is essential. In the previous section, the β^+ - p correlation was neglected; we now consider this, along with initial β-recoil effects on the proton energy.

As with the recoil mass, Equation A-13, we can write the new velocity of the proton as

$$v'_p = v_p - V_i \cos\theta \qquad \text{(A-22)}$$

where θ is the relative angle between the proton and the positron. Zero degrees is again in the direction of the Si detector. v_p is the velocity without β-recoil and v'_p is the observed velocity. We can write Equation A-22 in terms of the kinetic energy by squaring it,

$$v'^2_p = v^2_p - 2v_p V_i \cos\theta + V_i^2 \cos^2\theta \qquad \text{(A-23)}$$

this becomes

$$E_p(\theta) = E_p \left[1 - \varepsilon\cos\theta + \frac{\varepsilon^2}{4}\cos^2\theta\right] \qquad \text{(A-24)}$$

where $\varepsilon = \frac{2V_i}{v_p}$, $E_p = \frac{1}{2} m_p v_p^2$ and $E_p(\theta) = \frac{1}{2} m_p v'^2_p$. As was shown in Section A.2, $V_i << v_p$, and therefore ε is quite small.

The angular correlation function between β^+ and the p can be expressed as (Ho74,Fr77)

$$W(\theta) = 1 + a(E)\cos\theta + p(E)\cos^2\theta \qquad \text{(A-25)}$$

It is now only necessary to calculate the average proton energy to determine if there are any shifts from the E_p value.

$$\langle E_p(\theta)\rangle = \frac{\int_{\theta_1}^{\theta_2} E(\theta) W(\theta) 2\pi \sin\theta d\theta}{\int_{\theta_1}^{\theta_2} W(\theta) 2\pi \sin\theta d\theta} \qquad \text{(A-26)}$$

We again have $\theta_1 = 19°$ and $\theta_2 = 180°$.

Though it is possible to carry out this integration exactly, it is more instructive, and just about as accurate, to take the following approach.

Inserting Equation A-24 into the integral, our expression becomes

$$\frac{\langle E_p(\theta)\rangle}{E_p} = 1 + \frac{\int_{\theta_1}^{\theta_2} (-\varepsilon\cos\theta + \frac{\varepsilon^2}{4}\cos^2\theta) W(\theta) \sin\theta d\theta}{\int_{\theta_1}^{\theta_2} W(\theta) \sin\theta d\theta} \qquad \text{(A-27)}$$

We make use of the fact that the coefficients a(E) and p(E) are small (Fr77) and about the same order of magnitude as ε. With ε as the leading factor in our integral, we see that only the first term in the correlation function $W(\theta)$ will contribute (i.e., $W(\theta) \cong 1$). All the other terms are second order in the ε, a(E) and p(E) coefficients, and are therefore much smaller than the first term. So this becomes

$$\frac{\langle E_p(\theta) \rangle}{E_p} \cong 1 - \frac{\varepsilon \int_{\theta_1}^{\theta_2} \cos\theta \sin\theta d\theta}{\int_{\theta_1}^{\theta_2} \sin\theta d\theta} \qquad \text{(A-28)}$$

This reduces to

$$\frac{\langle E_p(\theta) \rangle}{E_p} = 1 + \frac{2V_i}{v_p} \left[\frac{1 - \cos^2 19°}{2(1 + \cos 19°)} \right] \qquad \text{(A-29)}$$

Now recalling Equation A-12, we note that for $E_\beta^2 >> m_e^2 c^4$ we have

$$V_i \cong \frac{E_\beta c}{M_i c^2} \qquad \text{(A-3Ø)}$$

Substituting this expression into Equation A-29 and rewriting, we obtain for the proton energy shift

$$\Delta E_p = \langle E_p(\theta) \rangle - E_p = \frac{\gamma E_\beta \sqrt{m_p c^2 E_p}}{M_i c^2} \qquad \text{(A-31)}$$

where

$$\gamma = \frac{1}{\sqrt{2}} \left[\frac{1 - \cos^2 19°}{1 + \cos 19°} \right]$$

In the decay of ^{25}Si, we find a value of $\Delta E_p = .443$ keV for this shift. For ^{24}Si this shift is $\Delta E_p = .467$ keV. We see that the maximum possible relative shift between these

two lines is only 24 electron volts. This effect is insignificant and can therefore be neglected.

APPENDIX B

The design of the electrostatic lens was numerical in nature since the complexity of the problem would exclude an analytical approach. The relaxation method is a finite difference approach to the solution of Laplace's equation

$$\nabla^2\Phi = 0. \tag{B-1}$$

It is based on the property that the value of the solution (to Laplace's equation) at any point in space is equal to the average of the solutions over an arbitrary surface surrounding the point.

Through the use of a Taylor series expansion of a function, one can obtain an approximation to the derivatives of this function in terms of nearby values.

$$\frac{d^2f(x)}{dx^2} \cong \frac{f(x+\Delta x) - 2f(x) + f(x-\Delta x)}{(\Delta x)^2} \tag{B-2}$$

By substituting these approximations to the derivatives into Laplace's equation, one obtains the value of the potential as an average of nearby potentials. For a two-dimensional Cartesian system with equally-spaced x and y mesh points, $\Delta x = \Delta y = h$, we have the expression

$$\Phi(x,y) = \frac{1}{4}\left[\Phi(x+h,y) + \Phi(x-h,y) + \Phi(x,y+h) + \Phi(x,y-h)\right] \tag{B-3}$$

Here we see quite clearly that the value of the potential

can be expressed as an average of the potentials around a given point.

Since our apparatus has axial symmetry (except for the square face of the channel plates), a lens with this symmetry was designed. With axial symmetry our problem reduces to a two-dimensional one. Laplace's equation in cylindrical coordinates for an axisymmetric system, $\Phi = \Phi(\rho,z)$, is

$$\frac{\partial^2\Phi}{\partial\rho^2} + \frac{1}{\rho}\frac{\partial\Phi}{\partial\rho} + \frac{\partial^2\Phi}{\partial z^2} = 0 \qquad \text{(B-4)}$$

The potential with equally-spaced ρ and z mesh points, $\Delta\rho = \Delta z = h$, for $\rho > \emptyset$ is

$$\Phi(\rho,z) = \frac{1}{4}\left[(1+\frac{h}{2\rho})\Phi(\rho+h,z) + (1-\frac{h}{2\rho})\Phi(\rho-h,z) + \Phi(\rho,z+h) + \Phi(\rho,z-h)\right] \qquad \text{(B-5)}$$

and for $\rho = \emptyset$ we have

$$\Phi(0,z) = \frac{1}{6}\left[4\Phi(h,z) + \Phi(0,z+h) + \Phi(0,z-h)\right] \qquad \text{(B-6)}$$

The alternate form of the equation at $\rho = \emptyset$ is due to the behavior of the first derivative term in Laplace's equation. In this coordinate system as $\rho \to \emptyset$, we find that the first derivative term becomes a second derivative term:

$$\lim_{\rho\to 0}\frac{1}{\rho}\frac{\partial\Phi}{\partial\rho} \longrightarrow \lim_{\rho\to 0}\frac{1}{\Delta\rho}\frac{\partial\Phi}{\partial\rho} \longrightarrow \frac{\partial^2\Phi}{\partial\rho^2} \qquad \text{(B-7)}$$

Therefore, for $\rho = \emptyset$, Laplace's equation becomes

$$2\frac{\partial^2\Phi}{\partial\rho^2} + \frac{\partial^2\Phi}{\partial z^2} = 0 \qquad \text{(B-8)}$$

which results in the second form for the potential (Equation B-6).

This relaxation approach to the solution of boundary value problems is a powerful yet simple method to apply in practice. One first chooses a set of grid (or mesh) points. These are the points at which the potential will be calculated. The boundaries, as well as fixed potential regions of this array, are held constant. The potentials for the remaining points of the potential array are obtained by systematically applying (in our case) Equations B-5 or B-6. The value of the potential from these equations is then put into the array. After this has been done for all the "free" points (those not held fixed), the process is repeated. These iterations are continued until the potential values have sufficiently converged.

A faster convergence can be obtained through the application of successive over-relaxation. This method is similar to a weighted average and uses the previous iteration's value of the potentials. After a potential at some point has been calculated, a correction to this potential is made using the expression

$$\Phi_{ij} = w\Phi_{ij}^{\text{current}} + (1 - w)\Phi_{ij}^{\text{previous}} \qquad \text{(B-9)}$$

where $1 < w < 2$. This corrected value is then placed in the array. Choosing $w = 1$ reduces over-relaxation to relaxation. Over-relaxation acts to more rapidly diffuse the correct values of the potentials from the fixed

boundaries and regions to the rest of the array.

To test a given lens design an existing Runge-Kutta-based code was modified to calculate electron trajectories through the lens (Di8Ø). This program used the potential array in order to calculate the electric fields acting on the electrons. The program was previoulsy tested with analytically-solvable cases and found to be in good agreement (Di8Ø).

In our design studies, a number of possible configurations were tested until a design with acceptable focusing characteristics was obtained.

Figure 2-9 shows the model lens upon which the actual lens was based. Eleven equipotentials and nine particle trajectories are shown. The particles started from rest near the surface of the converter foil. The inner and outer trajectories are at Ø.5 cm and 2.54 cm respectively. A time difference of 3.1 ns was calculated for these two paths. The mass resolution is still limited by β-recoil before the particle emission.

In this calculation an array of 81 x 126 points (ρ,z) with $\Delta z = \Delta\rho = .41625$ mm was used. The largest change in the potential was monitored for each iteration. After 25Ø iterations the largest change was that of 2.2 mV for a 5Ø mV potential. The total potential drop across the lens was 3ØØØ V, this change was thus insignificant and shows the good convergence of the calculation.

APPENDIX C

The principle of maximum likelihood is based on the assumption that the sequence of observations that actually occur in an experiment are those with the maximum probability of occurring. The likelihood function

$$\mathcal{L}(c) = \prod_{i=1}^{n} f(x_i;c) \qquad \text{(C-1)}$$

is the joint probability density of getting a particular experimental result, x_1, x_2, . . . x_n, assuming $f(x_i,c)$ is the "true" normalized one parameter distribution function, where

$$\int f(x;c)dx = 1 \qquad \text{(C-2)}$$

The best value of c will maximize the value of the likelihood function. Another useful quantity is the log-likelihood function, which is just the natural log of the likelihood function.

$$\ell(c) = \ln\mathcal{L}(c) = \ln\left(\prod_{i=1}^{n} f(x_i;c)\right) = \sum_{i=1}^{n} \ln\left(f(x_i;c)\right) \qquad \text{(C-3)}$$

To find the maximum of the likelihood function we require the first derivative of $\mathcal{L}(c)$ with respect to the parameter c to be zero:

$$\frac{d\,\mathcal{L}(c)}{dc} = 0 \qquad \text{(C-4)}$$

In addition, the second derivative must be negative:

$$\frac{d^2 \mathcal{L}(c)}{dc^2} < 0 \qquad \text{(C-5)}$$

Since taking the log of a function does not change the position of the maximum of the function, we can instead work with the log-likelihood function $\ell(c)$.

As a point of reference, we can show that for a set of measurements which are Gaussian-distributed this approach reduces to one of minimizing Chi-squared for the set of measurements (Be69).

For example, consider a linear relationship between two quantities (x,y):

$$y(x) = a + bx. \qquad \text{(C-6)}$$

We wish to obtain the best values for the coefficients a and b from a series of n measurements of (x_i,y_i). The probability for a given measurements will be

$$f(x_i;a,b) = \frac{1}{\sigma_i\sqrt{2\pi}} \exp\left[-\frac{1}{2}\left(\frac{y_i - y(x_i)}{\sigma_i}\right)^2\right] \qquad \text{(C-7)}$$

where $y(x_i)$ contains the a and b explicitly.

The log-likelihood function becomes

$$\ell(a,b) = \sum_{i=1}^{n} \ln\left(f(x_i;a,b)\right) = \frac{1}{\sqrt{2\pi}} \sum_{i=1}^{n} \frac{1}{\sigma_i} - \frac{1}{2} \sum_{i=1}^{n}\left(\frac{y_i - y(x_i)}{\sigma_i}\right)^2 \qquad \text{(C-8)}$$

The first term has no a or b dependence and, hence, is constant for a given set of measurements. We recall that the Chi-squared is defined as

$$\chi^2 \equiv \sum_{i=1}^{n}\left(\frac{y_i - y(x_i)}{\sigma_i}\right)^2 \qquad \text{(C-9)}$$

(a,b) thus becomes

$$\ell(a,b) = \text{constant} - \frac{\chi^2}{2} \qquad \text{(C-1Ø)}$$

From this expression we see that to maximize the log-likelihood function is equivalent to minimizing the χ^2.

Underlying all of the least-squares approaches to data analysis and curvefitting is the minimization of the χ^2. We see that this approach is consistent with the method of maximum likelihood but is valid only for Gaussian-distributed data. However, in many applications, it is the Gaussian distribution which is most useful and is a good approximation to the binomial and Poisson distributions for good statistics.

From the protons (or alpha) energies and the recoil time-of-flight we obtain a two-dimensional plot of energy vs. recoil mass (see Figure 2-12). Because of the β-recoil, there is a correlation between the proton energy and the recoil time-of-flight. On the plot of energy vs. recoil mass, we observe a tilting of the particle groups. Therefore, if we simply project these groups onto the energy axis, their energy resolution will be degraded.

As a result of this correlation, we choose to fit the data with bivariate Gaussian distributions (BGD). (C-11)

$$u(x,y) = \frac{1}{2\pi\sigma_x\sigma_y\sqrt{1-\rho^2}} \exp\left[-\frac{1}{2(1-\rho^2)}\left\{\left(\frac{x-\mu_x}{\sigma_x}\right)^2 - \frac{2\rho(x-\mu_x)(y-\mu_y)}{\sigma_x\sigma_y} + \left(\frac{y-\mu_y}{\sigma_y}\right)^2\right\}\right]$$

The μ_x and μ_y are respectively the x and y values for the centroid. The σ_x and σ_y are respectively the x and y standard deviations for the Gaussians, and ρ is the correlation coefficient between x and y. If $\rho = \emptyset$, and if we require that the joint distribution function be bivariate normal (Gaussian), then we have that x and y are uncorrelated. A three-dimensional plot of this can be seen in Figure 2-17. Many points in the two-dimensional data contain zero counts, and most have somewhat low statistics. We therefore need to use the Poisson distribution rather than the Gaussian distribution to fit our BGD (Equation C-11) to the data. The Poisson distribution function is given as

$$f(n_i;u) = \frac{u^{n_i} e^{-u}}{n_i!} \qquad \text{(C-12)}$$

We recall that the experimental points must be integers, since they are either observed or not observed (i.e., one cannot have half a count). Since we had a two-dimensional array of integer data, our actual distribution function was expressed as

$$f(n_{ij};u_{ij}) = \frac{u_{ij}^{n_{ij}} e^{-u_{ij}}}{n_{ij}!} \qquad \text{(C-13)}$$

The likelihood function becomes

$$\mathcal{L}(a_1,a_2,\ldots,a_6) = \prod_{i=1}^{N} \prod_{j=1}^{M} f(n_{ij};u_{ij}) \qquad \text{(C-14)}$$

where we have for u_{ij} the expression

$$u_{ij} = a_1 \exp\left[-\frac{1}{(1-a_2^2)}\left\{\left(\frac{i-a_3}{a_4}\right)^2 - \frac{2a_2(i-a_3)(j-a_5)}{a_4 a_6} + \left(\frac{j-a_5}{a_6}\right)^2\right\}\right] + a_7 + a_8 j \qquad \text{(C-15)}$$

The energy is along the i-axis and the recoil mass is along the j-axis. The last terms a_7 and a_8 are for the background. These terms were first fit by looking at projections (along the recoil axis) of regions around the peaks of interest. The improved statistics from these projections reduced the fluctuations of the background and made for a better fit to it. These parameters were also fit using the method of maximum likelihood and, once obtained, were not changed during the BGD fit.

As one can see from Equation C-15, this background was constant along the energy axis and linearly-varying along the recoil axis. In the fit of the bivariate Gaussian distribution several alternative forms for the background were tested (e.g., constant along the recoil axis and different a_7 and a_8 values), none of which had much effect on the centroids.

The coefficients a_2, a_4 and a_6 (the correlation parameter, the energy width and the recoil width) were obtained from the 4089 keV ^{25}Si peak. These were then not allowed to vary when fitting the 5402 keV ^{25}Si group and the ^{24}Si group. In addition, for the ^{24}Si peak, the recoil

centroid a_5 was determined from the mass scale, previously defined by the ^{21}Mg and the ^{25}Si lines. Fixing a_5 for the ^{24}Si peak reduced any errors because of statistical fluctuations and background effects.

These two-dimensional fits were superior to simple projections of the data, both in an improvement of the energy resolution and in the reduction of the bias which may occur when choosing the width of the mass band to be projected.

The fitting program used was a modification of a grid-search non-linear least-squares program from Bevington (Be69). This program originally was designed to find the minimum of the χ^2 in a multiparameter space. By taking the negative of the log-likelihood function, the maximum became a minimum and the same algorithm applied.

To obtain the errors using the maximum likelihood formalism, there are three accepted approaches. Two of these involve a weighted integration of the likelihood function; these are discussed in references (Me75) and (Or58). A more straightforward approach, also discussed in the above references, is to obtain the confidence interval for the fitting parameters. This is given as

$$P_r(c_1 \leq c \leq c_2) + \frac{\int_{c_1}^{c_2} \mathcal{L}(c)\,dc}{\int_{c_{min}}^{c_{max}} \mathcal{L}(c)\,dc} \qquad \text{(C-16)}$$

which is the probability that the interval between the estimates c_1 and c_2 includes the "true" value of the parameter c. The limits c_{max} and c_{min} are where the value of $\mathcal{L}(c)$ is effectively zero ($\mathcal{L}(c < c_{min}) = \mathcal{L}(c > c_{max}) = \emptyset$). If $c_2 = c_{max}$ and $c_1 = c_{min}$ unit probability is 1, hence, dividing by the integral over the entire range of possible values of c just normalizes the probability to 1.

We recall that for a normalized Gaussian distribution the area enclosed by one standard deviation is Ø.68269 of the total area of 1.Ø. By choosing the limits of the integration such that we enclosed 68.269% of the total area, we can obtain an estimate of the error in the value of our parameter.

$$.68269 = \frac{\int_{c_0+\Delta_1}^{c_0+\Delta_2} \mathcal{L}(c)\,dc}{\int_{c_{min}}^{c_{max}} \mathcal{L}(c)\,dc} \qquad \text{(C-17)}$$

In practice we integrate from $c_0 + \Delta_2$ or $c_0 - \Delta_1$ separately (i.e.,

$$\int_{c_0}^{c_0+\Delta_2} \quad \text{or} \quad \int_{c_0-\Delta_1}^{c_0}).$$

When the likelihood function is symmetric we have $\Delta_1 = \Delta_2 = \Delta$ and the usual result of $c_0 \pm \Delta$.

When integrating multiparameter likelihood functions $\mathcal{L}(c_1, c_2, \ldots, c_n)$, it is necessary to keep $\mathcal{L}(c_1, \ldots, c_n)$ at a local maximum. As the likelihood function is

numerically integrated, that is, for each step made in the integration variable (e.g., c_1), the other parameters ($c_i; i \neq 1$) are changed until we are at a maximum. This ensures that the error in the parameter is not underestimated.

REFERENCES

Ad68 E.G. Adelberger, A.V. Nero and F.S. Dietrich, Bull. Am. Phys. Soc. 13, 833 (1968).

Ad69 E.G. Adelberger, A.B. McDonald, and C.A. Barnes, Nucl. Phys. A124, 49 (1969).

Ad70 E.G. Adelberger, A.V. Nero, and A.B. McDonald, Nucl. Phys. A143, 97 (1970).

Ad72 E.G. Adelberger, P.T. Debevec, G.T. Garvey, and R. Ohanian, Phys. Rev. Lett. 29, 883 (1972).

Aj75 F. Ajzenberg-Selove, R. Middleton, and J.D. Garrett, Phys. Rev. C 12, 1868 (1975).

Aj78 F. Ajzenberg-Selove, Nucl. Phys. A300, 1 (1978).

Aj79 F. Ajzenberg-Selove, Nucl. Phys. A320, 1 (1979).

Aj80 F. Ajzenberg-Selove and C.L. Busch, Nucl. Phys. A336, 1 (1980).

Aj81 F. Ajzenberg-Selove, Nucl. Phys. A360, 1 (1981).

Aj82 F. Ajzenberg-Selove, Nucl. Phys. A375, 1 (1982).

Aj82a F. Ajzenberg-Selove, to be published in Nucl. Phys. (1982).

Al78 D.E. Alburger, S. Mordechai, H.T. Fortune, and R. Middleton, Phys. Rev. C 18, 2727 (1978).

Al78a D.E. Alburger, D.P. Balamuth, J.M. Lind, L. Mulligan, K.C. Young Jr., R.W. Zurmuhle, and R. Middleton, Phys. Rev. C 17, 1525 (1978).

Am77 Amperex, XP 2230-H.

An80 M.S. Antony, A. Huck, G. Klotz, A. Knipper, C. Miehe, and G. Walter, Berkeley Conference 1980.

As76 D. Ashery, M.S. Zisman, G.W. Goth, G.J. Wozniak, R.B. Weisenmiller, and J. Cerny, Phys. Rev. C 13, 1345 (1976).

Ay73 J. Äystö and K. Valli, Nucl. Instr. and Meth. 111, 531 (1973).

Ay74 J. Äystö, S. Hillebrand, K.H. Hellmuth and K. Valli, Nucl. Instr. and Meth. 120, 163 (1974).

Ay76 J. Äystö, V. Rantala, K. Valli, S. Hillebrand, M. Kortelahti, K. Eskola and T. Raunemaa, Nucl. Instr. and Meth. 139, 325 (1976).

Ay79 J. Äystö, D.M. Moltz, M.D. Cable, R.D. von Dincklage, R.F. Parry, J.M. Wouters, and J. Cerny, Phys. Lett. 82B, 43 (1979).

Ay81 J. Äystö, M.D. Cable, R.F. Parry, J.M. Wouters, D.M. Moltz, and J. Cerny, Phys. Rev. C 23, 879 (1981).

Ay81a J. Äystö, M.D. Cable, R.F. Parry, J.M. Wouters, D.M. Moltz, and J. Cerny, Phys. Rev. C 23, 879 (1981).

Ba70 A. Barbaro-Galtieri, S.E. Derenzo, L.R. Price, A. Rittenberg, A.H. Rosenfeld, N. Barash-Schmidt, C. Bricman, M. Roos, P. Soding, and C.G. Wohl, Rev. Mod. Phys. 42, 87 (1970).

Ba73 G. Baym, Lectures on Quantum Mechanics (W.A. Benjamin, Inc., 1973).

Ba82 P.H. Barker and J.A. Nolen (private communication, 1982).

Ba82a P.H. Barker and J.A. Nolen (private communication, (1982).

Be69 P.R. Bevington, Data Reduction and Error Analysis for the Physical Sciences (McGraw-Hill, 1969).

Be70 G. Bertsch and S. Kahana, Phys. Lett. 33B, 193 (1970).

Be77 W. Benenson, D. Mueller, E. Kashy, H. Nann, and L.W. Robinson, Phys. Rev. C 15, 1187 (1977).

Be79 W. Benenson and E. Kashy, Rev. Mod. Phys. 51, 527 (1979).

Bi81 W. Biesiot and Ph.B. Smith, Phys. Rev. C 24, 2443 (1981).

B167 R. Bloch, R.E. Pixley. and P. Truol, Phys. Lett. 25B, 215 (1967).

B169 J.L. Black, W.J. Caelli, D.L. Livesey, and R.B. Watson, Phys. Lett. 30B, 100 (1969).

B171 H.G. Blosser, G.M. Crawley, R. Deforest, E. Kashy and B.H. Wildenthal, Nucl. Instr. and Meth. 91, 61 (1971).

B176 M. Blann and F. Plasil, unpublished, 1976.

Bo77 W. Bohne, K.D. Buchs, H. Fuchs, K. Grabisch, D. Hilscher, U. Janetzki, U. Jahnke, H. Kluge, T.G. Masterson, and H. Morgenstern, Nucl. Phys. A284, 14 (1977).

Br36 G. Breit and E. Feenberg, Phys. Rev. 50, 850 (1936).

Bu77 R. Burgei, M. Grand, R. Maillard, and A. Papineau, Saclay Report No. CEA-N-2026, 256 (1977).

Bu80 G.R. Burleson, G.S. Blanpied, G.H. Daw, A.J. Viescas, C.L. Morris, H.A. Thiessen, S.J. Greene, W.J. Braithwaite, W.B. Cottingame, D.B. Holtkamp, I.B. Moore, and C.F. Moore, Phys. Rev. C 22, 1180 (1980).

Ca36 B. Cassen and E.U. Condon, Phys. Rev. 50, 846 (1936).

Ce64 J. Cerny, R.H. Pehl, and G.T. Garvey, Phys. Lett. 12, 234 (1964).

Ce66 J. Cerny, S.W. Cosper, G.W. Butler, R.H. Pehl, F.S. Goulding, D.A. Landis and C. Detraz, Phys. Rev. Lett. 16, 469 (1966).

Ce68 J. Cerny, Ann. Rev. of Nucl. Sci. 18, 27 (1968).

Co59 B.L. Cohen, Rev. Sci. Instr. 30, 415 (1959).

De78 Design Corporation, DA-47, 10K ohms (20%), 1% linearity.

Di78 W.R. Dixon, R.S. Storey, and J.J. Simpson, Phys. Rev. C 18, 2731 (1978).

Di79 M. DiStasio and W.C. McHarris, Am. J. Phys. 47, 440 (1979).

Di80 M.M. DiStasio, Ph.D. thesis, unpublished.

En78 P.M. Endt and C. van der Leun, Nucl. Phys. A310, 1 (1978).

Er79 J.R. Erskine, Nucl. Instr. and Meth. 162, 371 (1979).

Fa77 J.C. Faivre, H. Fanet, A. Garin, J.P. Robert, M. Rouger, and J. Saudinos, Trans. IEEE NS24, 299 (1977).

Fe77 Ferrofluidics Corp., SB-500-A-N-069, .5 in. dia. rotary feedthrough.

Fo72 S. Fortier, H. Laurent, J.M. Maison, J.P. Schapira, J. Vernotte, and W. Weisz, Phys. Rev. C 6, 378 (1972).

Fo77 H.T. Fortune, R. Middleton, M.E. Cobern, G.E. Moore, S. Mordechai, R.V. Kollarits, H. Nann, W. Chung, and B.H. Wildenthal, Phys. Lett. 70B, 408 (1977).

Fo77a G. Foit, Ion Beam Handbook for Material Analysis, edited by J.W. Mayer and E. Rimini (Academic Press, New York, 1977).

Fr77 S.J. Freedman, R.D. Cousins Jr., C.A. Gagliardi, G. T. Garvey, and J.F. Greenhalgh, Phys. Lett. 67B, 165 (1977).

Ga64 G.T. Garvey, J. Cerny, and R. Pehl, Phys. Rev. Lett. 13, 548 (1964).

Ga69 G.T. Garvey, Nuclear Isospin, edited by J.D. Anderson, S.D. Bloom, J. Cerny, and W.W. True (Academic Press, New York, 1969), p. 703.

Ga76 Galileo Electro-Optics Corp. M-2062, pore size 25 micrometers, 15 degree slanted holes, 1.488 in. x 1.488 in. square array.

Go74 D.R. Goosman, Nucl. Instr. and Meth. 116, 445 (1974).

Ha70 J.C. Hardy, H. Brunnader, and J. Cerny, Phys. Rev. C 1, 561 (1970).

Ha74 G.C. Hamilton and L.N. Vance, DOALL, MSU program (1974).

Ha77 E. Hagberg, P.G. Hansen, J.C. Hardy, A. Huck, B. Jonson, S. Mattsson, H.L. Ravn, P. Tidemad-Petersson, and G. Walter, Phys. Rev. Lett. 39, 792 (1977).

He32 W. Heisenberg, Zeits. f. Physik 77, 1 (1932).

He61 Heraeus, Type R15Ø.

He68 D.C. Hensley, P.H. Nettles, and C.A. Barnes, Phys. Lett. 26B, 435 (1968).

He69 E.M. Henley, Isospin in Nuclear Physics, edited by D.H. Wilkinson (North-Holland Publishing Company, Amsterdam, 1969), p. 17.

He77 J.C.P. Heggie and H.H. Bolotin, Aust. J. Phys. 3Ø, 4Ø7 (1977).

He81 E.M. Henley, Proceedings of the Nuclear Theory Summer Workshop, Santa Barbara, August 1981, edited by G.F. Bertsch (World Scientific, Singapore, 1982), p. 1.

Hi62 S. Hinds, H. Marchant, and R. Middleton, Nucl. Phys. 38, 81 (1962).

Hi75 D. Hirdes, E. Georg, H. Wollnik, and R. Brandt, Nucl. Instr. and Meth. 13Ø, 15 (1975).

Ho74 B.R. Holstein, Rev. Mod. Phys. 46, 789 (1974).

Hu76 A. Huck, G.J. Costa, G. Walter, M.M. Aleonard, J. Dalmas, P. Hubert, F. Leccia, P. Mennrath, J. Vernotte, M. Langevin, and J.M. Maison, Phys. Rev. C 13, 1786 (1976).

Il74 Ilford, type L4, 2Ø-inch long, 25-micron emulsion, 1974.

Ja6Ø N. Jarmie and M.G. Silbert, Phys. Rev. 12Ø, 914 (196Ø).

Ja69 J. Janecke, Isospin in Nuclear Physics, edited by D.H. Wilkinson (North-Holland Publishing Company, Amsterdam, 1969), p. 297.

Ja74 C.W. de Jager, H. de Vries, and C. de Vries, Atomic Data and Nucl. Data Tables 14, 479 (1974).

Ja75 J. Janecke, F.D. Becchetti, L.T. Chua, and A.M. VanderMolen, Phys. Rev. C 11, 2114 (1975).

Je72 N.A. Jelley, N. Anyas-Weiss, M.R. Wormald, B.Y. Underwood, and K.W. Allen, Phys. Lett. 4ØB, 2ØØ (1972).

Jo63 C.H. Johnson, F. Pleasonton, and T.A. Carlson, Phys. Rev. 132, 1149 (1963).

Jo74 J. Cerny, N.A. Jelley, D.L. Hendrie, C.F. Maguire, J. Mahoney, D.K. Scott, and R.B. Weisenmiller, Phys. Rev. C 1Ø, 2654 (1974).

Ke78 G.J. KeKelis, M.S. Zisman, D.K. Scott, R. Jahn, D.J. Vieira, J. Cerny, and F. Ajzenberg-Selove, Phys. Rev. C 17, 1929 (1978).

Ki65 Kinney Vacuum Div., KDH-65.

Ko75 R. Kouzes and W.H. Moore, Phys. Rev. C 12, and Phys. Rev. C 13, 89Ø (1976).

Ku67 H.M. Kuan, D.W. Heikkinen, K.A. Snover, F. Riess, and S.S. Hanna, Phys. Lett. 25B, 217 (1967).

Ku72 H.M. Kuan, G.L. Latshaw, W.J. O'Connell, D.W. Heikkinen, E.G. Adelberger, A.V. Nero, and S.S. Hanna, Nucl. Phys. A193, 497 (1972).

Ly67 H. Lycklama and T.J. Kennett, Can. J. Phys. 45, 3Ø39 (1967).

Ma55 W.M. MacDonald, Phys. Rev. 1ØØ, 51 (1955).

Ma75 D.J. Martin, J.A. Szucs, and D.T. Kelly, Can. J. Phys. 53, 1734 (1975).

Ma76 A.K. Mazumdar, H. Wagner, W. Walcher, and T. Lund, Nucl. Instr. and Meth. 139, 319 (1976).

Ma76a D.J. Martin, H.C. Evans, and J.A. Szucs, Phys. Rev. C 14, 132Ø (1976).

Me75 S.L. Meyer, Data Analysis for Scientists and Engineers (Wiley, New York, 1975).

Mi76 G.F. Millington, R.M. Hutcheon, J.R. Leslie, and W. McLatchie, Phys. Rev. C 13, 879 (1976).

Mi77 Micro Switch, 61VM-DC Control Motor (ALNIC-V7).

Mo79 D.M. Moltz, J. Aysto, M.D. Cable, R.D. von Dincklage, R.F. Parry, J.M. Wouters, and J. Cerny, Phys. Rev. Lett. 42, 43 (1979).

Mo79a D.M. Moltz, Ph.D. thesis, University of California at Berkeley, Report No. LBL-9718.

Mo82 C.L. Morris, G.R. Burleson, G.S. Blanpied, G.H. Daw,

A.J. Viescas, H.A. Thiessen, S.J. Greene, W.J. Braithwaite, W.B. Cottingame, D.B. Holtkamp, I.B. Moore, and C.F. Moore, to be published in Phys. Rev. C (private communication, 1982).

Mo82a C.L. Morris (private communication, 1982).

Mv76 MVE Cryogenics, M-1, super insulated stainless steel dewar flasks (open dewar).

Mv76a MVE Cryogenics, T-11A, liquid nitrogen level controller (time cycle filling).

Ne71 P.H. Nettles, C.A. Barnes, D.C. Hensley, and C.D. Goodman, Bull. Am. Phys. Soc. 16, 489 (1971).

No73 J.A. Nolen Jr., At. Mass. and Fund. Const. 5, edited by J.H. Sanders and A.H. Wapstra (Plenum Press, New York, 1976), p. 140.

No74 J.A. Nolen Jr., G. Hamilton, E. Kashy, and I.D. Proctor, Nucl. Instr. and Meth. 115, 189 (1974).

No76 J.W. Noé, D.F. Geesaman, P. Paul, and M. Suffert, Phys. Lett. 65B, 125 (1976).

Nu77 NUPRO, SS-8FE-2, stainless steel filter element, 2 micrometers.

Or58 J. Orear, University of California at Berkeley, Report No. UCRL-8417 (1958).

Or78 ORTEC Inc., TE-015-150-300.

Pi60 D. Piraino, C.H. Paris, and W.W. Buechner, Phys. Rev. 119, 732 (1960).

Ri67 F. Riess, W.J. O'Connell, D.W. Heikkinen, H.M. Kuan, and S.S. Hanna, Phys. Rev. Lett. 19, 367 (1967).

Ri75 J.A. Rice, B.H. Wildenthal, and B.M. Preedom, Nucl. Phys. A239, 189 (1975).

Ro38 Roots Connersville, RGS-SP-AVM, size 38.

Ro69 J.T. Routti and S.G. Prussin, Nucl. Instr. and Meth. 72, 125 (1969).

Ro73 R.G.H. Robertson and B.H. Wildenthal, Phys. Rev. C 8, 241 (1973).

Ro73a R.G.H. Robertson and J.A. Nolen, Bull. Am. Phys. Soc. 18, 1423 (1973).

Ro74 R.G.H. Robertson, S. Martin, W.R. Falk, D. Ingham, and A. Djaloeis, Phys. Rev. Lett. 32, 1207 (1974).

Ro75 R.G.H. Robertson, W.S. Chien, and D. Goosman, Phys. Rev. Lett. 34, 33 (1975).

Ro76 R.G.H. Robertson, W. Benenson, E. Kashy, and D. Mueller, Phys. Rev. C 13, 1018 (1976).

Ro77 R.G.H. Robertson, T.J. Bowles, and S.J. Freedman, Nucl. Instr. and Meth., 147, 361 (1977).

Ro77a D.W.O. Rogers, N. Anyas-Weiss, S.P. Dolan, N.A. Jelley, and T. K. Alexander, Can. J. Phys. 55, 206 (1977).

Ro78 R.G.H. Robertson, T.L. Khoo, G.M. Crawley, A.B. McDonald, E.G. Adelberger, and S.J. Freedman, Phys. Rev. C 17, 1535 (1978).

Ro78a R.G.H. Robertson, E. Kashy, W. Benenson, and A. Ledebuhr, Phys. Rev. C 17, 4 (1978).

Ro81 R.G.H. Robertson, J.A. Nolen Jr., T. Chapuran and R. Vodhanel, Phys. Rev. C 23, 973 (1981).

Sa77 Sargent-Welch, 3133C vertical turbo molecular pump.

Se73 R.G. Sextro, Ph.D. thesis, University of California at Berkeley, Report No. LBL-2360 (1973).

Se78 R.R. Sercely, R.J. Peterson, and E.R. Flynn, Phys. Rev. C 17, 1919 (1978).

Si61 M.G. Silbert and N. Jarmie, Phys. Rev. 123, 221 (1961).

Si72 J.J. Simpson, W.R. Dixon, and R.S. Storey, Phys. Rev. Lett. 29, 1472 (1972).

Sn69 K.A. Snover, D.W. Heikkinen, F. Riess, H.M. Kuan, and S.S. Hanna, Phys. Rev. Lett. 22, 239 (1969).

St73 D.F.H. Start, N.A. Jelley, J. Burde, D.A. Hutcheon, W.L. Randolph, B.Y. Underwood, and R.E. Warner, Nucl. Phys. A206, 207 (1973).

St77 W.A. Sterrenburg, G. Van Middlekoop, and J.A.G. De Raedt, Nucl. Phy. A290, 200 (1977).

Sz73 J. Szucs, B.Y. Underwood, T.K. Alexander, and N. Anyas-Weiss, Nucl. Phys. A212, 293 (1973).

Tr71 G.F. Trentelman, B.M. Preedom, and E. Kashy, Phys. Rev. C 3, 2205 (1971).

Tr76 R.E. Tribble, R.A. Kenefick, and R.L. Spross, Phys. Rev. C 13, 50 (1976).

Tr76a R.E. Tribble, J.D. Cossairt, and R.A. Kenefick, Phys. Lett. 61B, 353 (1976).

Tr76b G.F. Trentelman, R.G.H. Robertson, R. Gleitsmann and L.W. Robinson, SPECTKINE IV, MSU Program, 1976.

Tr77 R.E. Tribble, J.D. Cossairt, and R.A. Kennefick, Phys. Rev. C 15, 2028 (1977).

Tr77a R.E. Tribble, J.D. Cossairt, D.P. May, and R.A. Kenefick, Phys. Rev. C 16, 1835 (1977).

Tr80 R.E. Tribble, D.M. Tanner, A.F. Zeller, Phys. Rev. C 22, 17 (1980).

Va67 G. Van Middelkoop, Nucl. Phys. A97, 209 (1967).

Va78 Vac Torr, D-1000, two-stage vacuum pump, Precision Scientific Co.

Ve73 J. Vernotte, S. Gales, M. Langevin, and J.M. Maison, Phys. Rev. C 8, 178 (1973).

Ve76 J. Vernotte, S. Fortier, M. Langevin, J.M. Maison, M. Vergnes, and B.H. Wildenthal, Phys. Rev. C 13, 461 (1976).

Wa73 E.K. Warburton, P. Gorodetzky, and J.A. Becker, Phys. Rev. C 8, 418 (1973).

Wa77 A.H. Wapstra and K. Bos, At. Data Nucl. Data Tables 19, 175 (1977); 20, 1 (1977).

Wa79 A.H. Wapstra (private communication, 1979).

Wa81 A.H. Wapstra and K. Bos, October 1981 Midstream Atomic Mass Adjustment (private communication).

Wa82 A.H. Wapstra and K. Bos (private communication, 1982).

We77 Sargent Welch, DUO Seal, R1398D.

Wi66 C.F. Williamson, J.P. Boujot and J. Picard, Saclay Report No. CEA-R 3042, 1 (1966).